EXTREME PHYSICAL PHENOMENA ASSOCIATED
WITH CLOSE-IN SOLID EXOPLANETS:
MODELS AND CONSEQUENCES

by

Prabal Saxena
A Dissertation
Submitted to the
Graduate Faculty
of
George Mason University
In Partial fulfillment of
The Requirements for the Degree
of
Doctor of Philosophy
Computational Sciences and Informatics

Committee:

| | |
|---|---|
| _____ | Dr. Michael Summers, Dissertation Director |
| _____ | Dr. Jie Zhang, Committee Member |
| _____ | Dr. Robert Weigel, Committee Member |
| _____ | Dr. Paul Cooper, Committee Member |
| _____ | Dr. Kevin Curtin, Department Chair, Department of Computational and Data Sciences |
| _____ | Dr. Donna M. Fox, Associate Dean, Office of Student Affairs Special Programs, College of Science |
| _____ | Peggy Agouris, Dean, College of Science |

Date: _____ Summer Semester 2015
George Mason University
Fairfax, VA

# Extreme Physical Phenomena Associated with Close-In Solid Exoplanets: Models and Consequences

A dissertation submitted in partial fulfillment of the requirements for the degree of Doctor of Philosophy at George Mason University

By

Prabal Saxena
Bachelor of Science
Columbia University, 2007

Director: Dr. Michael Summers, Professor
(School of Physics, Astronomy and Computational Sciences)

Summer Semester 2015
George Mason University
Fairfax, VA

# Dedication

I dedicate this dissertation to anyone who is willing to read it!

Also to a mischievous pug named Buddy and to a rambunctious cat named Scully.

# Acknowledgments

None of the research produced as part of this dissertation could have been done without the support of my family, friends, and instructors. I am especially indebted to my wonderful parents, Praveen and Punam, my wife, Angela, and my brother, Pulkit.

Additionally, the work produced by this thesis is underpinned by a large body of scientific and computational literature as well as software - I am grateful to the many hard working individuals who produced these products.

# Table of Contents

# List of Tables

# List of Figures

# Abstract

EXTREME PHYSICAL PHENOMENA ASSOCIATED WITH CLOSE-IN SOLID EXOPLANETS: MODELS AND CONSEQUENCES

Prabal Saxena, PhD

George Mason University, 2015

Dissertation Director: Dr. Michael Summers

Solid exoplanets orbiting at very close distances away from their host star are astrophysical laboratories for unique and exotic processes that define everything from their orbit and shape to their atmospheres and interiors. We create models to examine the unique physical environments that these planets inhabit and explore the effects on planetary shape and on atmosphere and resurfacing processes. In particular we examine three related topics. The first topic involves the creation of a model of the atmospheres of synchronously orbiting close in solid planets which examines the potential of mass advection by the atmosphere to deform the planets shape and produce observable surface signatures. This model reproduces and builds upon earlier low dimension atmospheric models produced for Io and Heated Super-Earths by incorporating stellar disk insolation and latent heat considerations and then examines bulk atmospheric mass transport processes on a variety of different close in solid exoplanets. Spatial deposition profiles are then compared to putative sub-stellar magma oceans in order to examine deformation to a planets' shape and potential production of observable surface features.

The second is the potential for tidally and rotationally distorted planets in synchronous orbit to produce observational effects and transit signatures which can both confound system

characterization and also act as a probe to constrain system and planet properties. In this model we examine a number of different planet-star systems and quantify their potential biases and asphericity signatures in hypothetical transit data. The results indicate that such signatures and biases exceed observational thresholds of a number of current and future surveys and instruments and consequently may be an invaluable probe for exoplanet characterization - in particular they may help to discriminate between rocky super-earths and mini neptunes - a fundamental unresolved question regarding exoplanets.

Finally, the last project describes current work that looks at the consequences of exoplanet asphericity on those planets' atmospheres. The project will look to produce estimates of atmospheric effects on these planets that are akin to gravity darkening in aspherical stars. Such effects will be calculated in order to understand how they may influence dynamics and also observational atmospheric retrieval.

# Chapter 1: Introduction to Exoplanets

Since the first discoveries in the early 1990's, one of the most humbling statistics in astronomy has been the ever increasing number of planets discovered outside our solar system. With each additional exoplanet detection, countless theses and review paper introductions are rendered obsolete while simultaneously an additional mystery is added to the current census of humanity's knowledge of the universe. This introduction of an unfamiliar planet is often fraught with observational considerations which confound the type of characterization that has been done for planets in our solar system. However, in spite of that, current instruments and methods have still been able to glean an astounding wealth of information on these newly discovered worlds and have identified at least one simple rule regarding them - that they are full of surprises.

## 1.1 Exoplanet Detection

While there are many methods that have used or are being developed to detect exoplanets, to date, the majority of detected exoplanets have been found using only a few dominant methods. Transit photometry and radial velocity have accounted for the bulk of discoveries. However, methods such as gravitational microlensing, direct imaging, astrometry and a variety of different timing and brightness variations based methods have also been used or are being developed to find exoplanets. Figure 1.1 shows a scatter plot of exoplanets detected by the different methods as a function of their mass and distance from host star.

Exoplanets discovered by the transit method or by the radial velocity method constitute the largest portion of planets currently detected and are also the two methods that are most rapidly adding to the exoplanet count. Variations in the data collected by those two methods have also been used to identify a significant number of exoplanets. As new

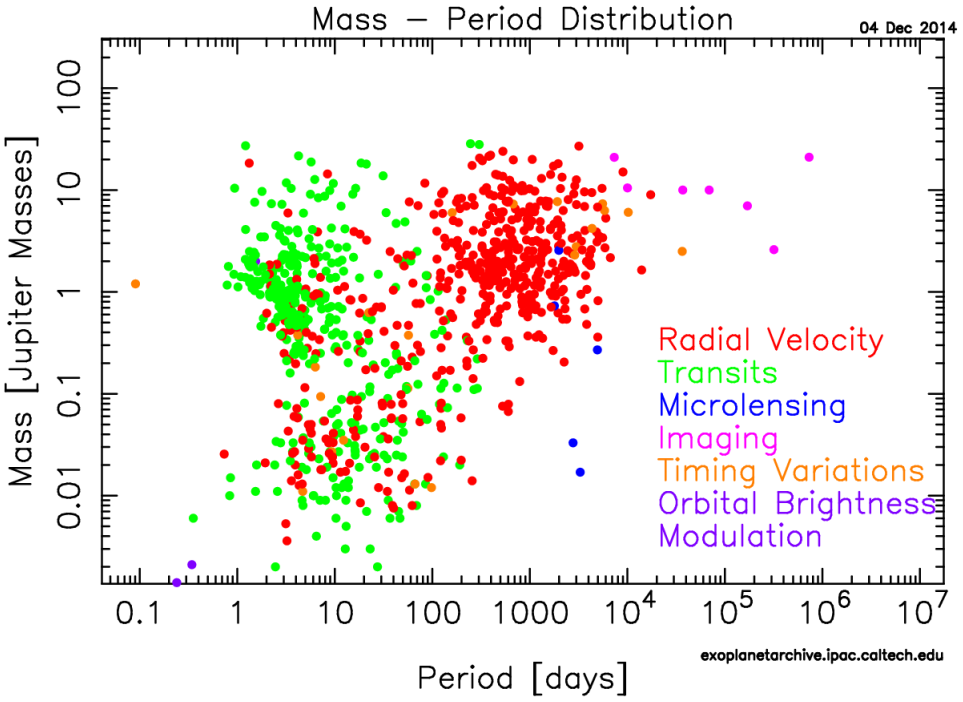


Figure 1.1: The current census of detected exoplanets labeled by detected method and plotted as a function of mass and orbital period from the NASA Exoplanet Archive. [Akeson et al., 2013]

instruments and surveys begin to return data and improved techniques are refined, other detection methods such as astrometry and microlensing have also started to produce a larger yield of newly detected exoplanets. This section will briefly describe the techniques used to detect exoplanets with a detailed focus on the Transit Photometry given the relevance of that detection method to the studies that constitute this thesis.

### 1.1.1 Transit Photometry

Transit Photometry has been the most prolific exoplanet detection method to date given that the number of confirmed exoplanet detections it is responsible for is more than double the next most successful technique. What makes this efficacy more surprising is that transit photometry may also be the most physically intuitive exoplanet detection technique.

Transit Photometry primarily detects exoplanets when a planet orbiting a star passes

between the star and observer's line of sight, temporarily blocking out a portion of the light typically observed from the star. During this process, the temporary drop in flux from the star can be captured as time series data which is denoted as the system's *lightcurve* (see Figure 1.2). Such a phenomenon requires that from the observer's perspective, the orbit of the planet must be oriented in such a way that the projected area of the planet falls upon the apparent projected area of it's host star. As a result, for a planet $R_p \ll R_s$ on a nearly circular orbit a distance $a$ from it's host star, the probability of a transit is $\sim {}^{R_s}/_{a}$. A consequence of this is that close-in and large planets are more easily detected while the probability of detecting a transiting planet falls as semi-major axis gets larger and planetary radius gets smaller. Additionally, there is a bias towards detecting planets around smaller stars using this method while planets around larger stars are harder to confirm above noise thresholds.

While the transit of the planet between the host star and an observer is the most common means of detection and parameter estimation of an exoplanet system, the remaining portions of the light curve often hold additional invaluable information regarding the system. Figure 1.2 displays the change in light from the system due to the changing amount of light reflected off the planet during periods when neither body is being eclipsed. This reflected light phase curve can act as a probe of atmospheric or surface features. There also exist a number of other system effects which can result in variations in the light curve that may also enable additional characterization. These additional effects can be so powerful that a number of exoplanets have actually been detected from light curves where there is no primary transit! The different components are described in the following section and identified using techniques similar to those used to identify the primary transit and to fit radial velocity measurements.

The light curve data of a system with a planet transiting a star can be written in a convenient analytic manner when certain contrived system parameters are assumed. The utility of such expressions is important to understand the planetary and system parameters which may be generally gleaned from transit photometry and often times the assumptions made

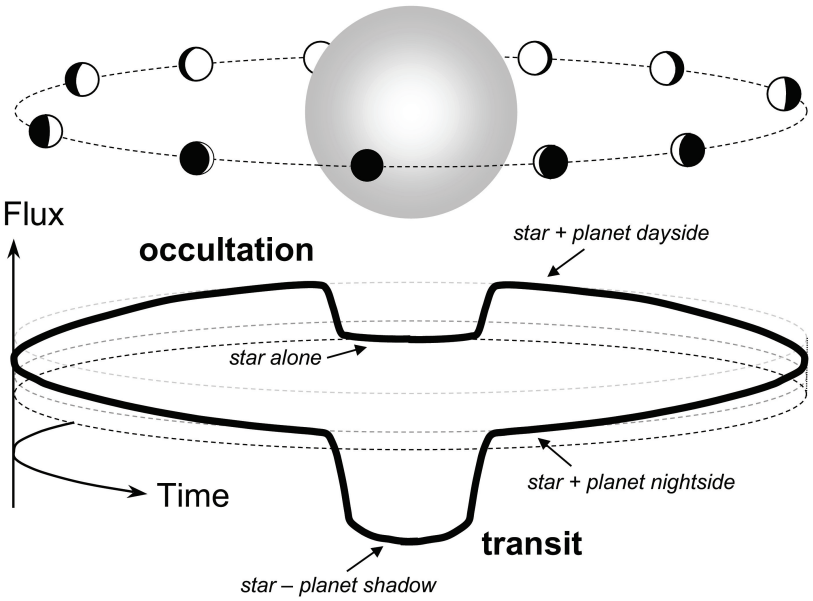


Figure 1.2: Image of a transit and occultation in a planet star system from Winn [2010]. When the planet passes in front of the star, part of the star's light is blocked out resulting in a dip in the total flux observed. As the planet orbits around the star before and after transit the total flux from the system changes as the amount of light reflected off the planet varies during different phases and as other additional secondary effects also contribute to light curve variations. When the planet passes behind the star during the occultation there is a secondary dip in the total flux as light reflected off the planet is blocked.

for such expressions to hold are accurate to a fair degree. In particular, unique solutions for the stellar mass, stellar radius, companion radius, companion orbital separation and orbital inclination can be obtained used a set of simplifying assumptions. The assumptions include the following [Seager and Mallén-Ornelas, 2003]:

- The planet has a circular orbit.
- $M_p \ll M_s$
- The stellar mass-radius relation in known
- The light comes from a single star as opposed to two or more blended stars

- The planet is fully superimposed on the star, resulting in a flat eclipse bottom in the light curve
- The period can be deduced from the light curve through the observation of two consecutive transits

The first three assumptions hold or are a good approximation in many cases. While observational surveys looking for potential exoplanets are careful to identify potential sources in a field that may result in a blend, the fourth assumption is certainly a complicating factor in the detection of exoplanets by transit. Most transiting exoplanets detected so far are fully superimposed on their host star at some point during their transit, though exoplanets have been identified from light curves when they only partially graze their host star or in some cases when they do not transit their host star at all. Finally, observing consecutive transits of an exoplanet is a typical procedure in order to derive the planet's orbital period. In the case where the stellar mass and radius are known from a measured spectral type and the impact parameter is known one can actually estimate the planetary orbital period from only one transit. The impact parameter, b, is the projected distance between the planet and star centers - a parameter which is a product of the orbital inclination of the planet (shown in figure 1.4). Given the determination of these system and planetary parameters from a transiting system, one can this knowledge with data obtained from other corroborating detection and characterization techniques such as the Radial Velocity method in order to obtain further derived parameters such as bulk planetary density.

While this analytical treatment of transits yields a very useful description of how to extract important information about an exoplanet system, in reality the assumptions required for this treatment to be a complete description often do not hold. In fact, in some cases current transit detection techniques are biased towards finding exoplanet systems where certain assumptions do not hold. One of the most simple examples of this is that for planets with the same orbital distance from their host star, those planets on eccentric orbits are more likely to transit than their circularly orbiting counterparts by a factor of $(1-e^2)^{-1}$ [Barnes,

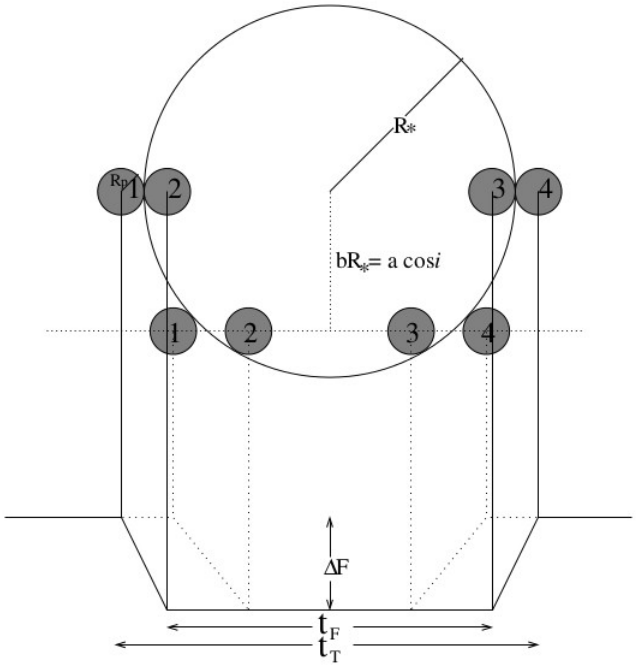


Figure 1.3: Image of two transits with their schematic light curves taken from Seager and Mallén-Ornelas [2003]. The two separate transits show how different geometric alignments of the planetary system can produce different shaped light curves. The impact parameter is given by b and is related to the orbital inclination of the planet. $t_f$ is the total transit duration where the planet is fully imposed upon the star while $T_f$ is the transit duration between ingress (the beginning of transit) and egress (the end of transit).

2007]. This is a simple derivation based on the description of the variation of the orbital distance of a planet from it's host star as a function of the true anomaly $f$, semi-major axis $a$ and the eccentricity $e$:

$$r = \frac{a(1-e^2)}{(1+e\cos f)} \tag{1.1}$$

[Murray, C. D. and Dermott, S. F., 2000]

Using this equation for r with a non-zero value for $e$ in the integral for the probability of a transit given in equation 4 of Barnes [2007] yields the additional $(1-e^2)^{-1}$ factor that a planet on an eccentric orbit is likely to transit by. This departure from the assumption of

a circular exoplanet orbit is emblematic of the fact that exoplanet systems do not typically adhere to the idealized descriptions prescribed by different detection and characterization techniques that most easily extract their orbital and planetary parameters [Kipping, 2008]. Indeed, departures from the idealized requirements necessary for this analytic depiction of transits will produce different transit shapes that can confound characterization of the system and also help constrain parameters like impact parameter and eccentricity. As a consequence of this, the ability to find numerical fits which can accurately approximate data to constrain these properties are a critical component of observational exoplanet science including transit photometry.

The need for more versatile parameter extraction techniques has led to an exploration of different statistical and numerical methods that have been used for analogous problems in other sciences and quantitative disciplines. In the case of transit photometry, this search has focused on the ability to obtain exoplanet transit signals from their light curve time series data. Morphologically, this amounts to being able to detect periodic reductions in the amount of light received from the system that occur with a predictable shape in the time series data. Specific techniques have become especially widespread due to their utility in fitting and interpreting such features.

One of the most powerful is a box least squares fitting algorithm which analyzes stellar photometric time series for exoplanets [Kovács et al., 2002]. This box fitting method is effective at relatively low signal to noise ratios and looks for periodic changes in the flux between two discrete levels, the lower of which signifies a potential planet detection. This particular algorithm has been implemented in some of the most robust exoplanet searches [Mandel and Agol, 2002] and has yielded planets and systems of extraordinary diversity due to its versatility. Periodic or regular deviations from a mean value of these extracted transit times, transit periods or dimming due to an exoplanet are also powerful tools that can indicate the presence of additional planets that may be producing such effects or may be indicative of unique system characteristics. Indeed a substantial number of exoplanets in multi-planet systems have been discovered due to transit timing variations [Steffen et al.,

2013].

Transit fitting and parameter estimation within bayesian statistical frameworks are also becoming an important feature of transit photometry. Such tools typically use Markov Chain Monte Carlo techniques to fit light curves and incorporate likelihood functions from a variety of sources [Gazak et al., 2012, Placek et al., 2014]. These fitting schemes have been used to extract parameter estimates from the full light curve, which includes the primary transit, phase curve and secondary transit portions.

### 1.1.2 Photometry: Beyond the Primary Transit

The light curve of a star that hosts a planet may contain additional information regarding the nature of the system outside of the portions of the time series where the planet transits the star. For planets that transit their host star (and in the latter case some non-transiting planets) the secondary eclipse and phase curve can also provide additional information that can enable system and planet characterization.

The secondary eclipse portion of a light curve reflects the occultation of the planet by the star. The additional starlight reflected off the planet as well as the planet's intrinsic thermal emission is blocked and there is a consequent drop in the total flux from the system. Quantifying the magnitude and timing of the drop in flux as the planet is occulted can place bounds on orbital eccentricity [Knutson et al., 2007], planetary albedo [Cowan and Agol, 2011], atmospheric pressure-temperature profiles [Baskin et al., 2013, Deming et al., 2014] and can even be used to generate spatial brightness maps [Majeau et al., 2012].

The phase dependent light curve portion of the light curve (phase curve) occurs between the transit and secondary eclipse and represents the part of the planet's orbit around the star where neither the star or planet is obscured by the other body. This portion of the light curve can contain invaluable information regarding the system and planet but is complicated by the fact that there are numerous overlapping signals due to different processes which produce the critical variations in flux. A simple expression which reflects the total observed flux due to the different contributions to this portion of the light curve (normalized by the

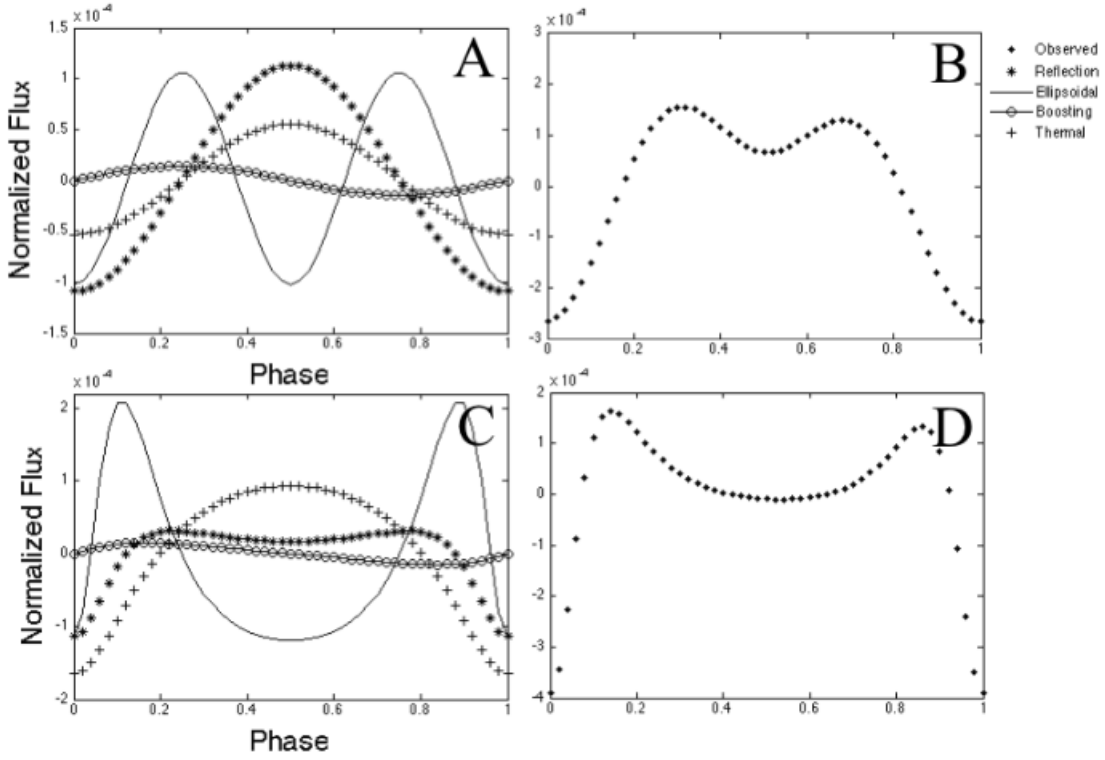


Figure 1.4: Images A and C demonstrate the contributions of different effects on the phase curve portion of a light curve while images B and D demonstrate the summed up contributions. The top row corresponds to a Hot Jupiter in a circular orbit while the bottom images correspond to a Hot Jupiter in an eccentric orbit (e=0.3). Images taken from Placek et al. [2014].

stellar flux) is given by:

$$F_{total} = \frac{F_* + F_{ell} + F_{dop} + F_{ref} + F_{the}}{F_*} \tag{1.2}$$

where $F_*$ is the stellar flux, $F_{ell}$ is the flux due to ellipsoidal variations due to both the star and planet, $F_{dop}$ is the flux due to Doppler beaming, $F_{ref}$ is the flux due to light reflected off of the planet and $F_{the}$ is the flux due to the thermal emission from the planet.

In general, $F_*$ is expected to be relatively constant throughout the phase curve portion of the light curve. In reality, there can sometimes be significant stellar variability such as

starspots that may complicate interpretation of other signals throughout the light curve - a fact that has spawned a number of different methods and tools to correct for such effects [Ballerini et al., 2012, Dumusque et al., 2014a, Béky et al., 2014].

Ellipsoidal variations $F_{ell}$ are variations in flux due to the change in the apparent shape of the star or the planet. These changes result from tidal distortion of the star by a closely orbiting massive planet or by the tidal distortion of a closely orbiting planet by a star. The sky projected area of the distorted body varies as function of phase resulting in a variation of total flux from the changing apparent surface of the star [Mislis et al., 2012]. For the planet, the change in apparent shape results in a varying flux from both the reflected light and thermal emission phase components that diverges from the perfectly spherical planet case.

Doppler boosting $F_{dop}$ is a result of the reflex orbital motion of the star due to its planet's gravity. The varying radial velocity of the star as it moves in orbit results in stellar Doppler shifts that cause variability in flux [Loeb and Gaudi, 2003].

A planet that transits its star will exhibit periodic variations in the stellar light reflected off its surface. These phase related variations $F_{ref}$ are analogous to the way the Moon goes through phases as viewed from Earth. The reflected light varies as a function of the phase angle - the angle between the star and observer as seen from planet. In addition to the phase, the flux contribution from this component is also dependent on planetary albedo, making it a potential proxy for surface or atmosphere characterization.

Finally, $F_{the}$ is the flux due to thermal emission intrinsic to the planet. Most planets are too cool for this effect to be significant relative to the other phase curve variations. However, for planets close in to their host star, surface or atmospheric temperatures may be high enough to allow favorable contrast ratios in certain bands.

### 1.1.3 Radial Velocity

The Radial Velocity method has been other technique that has found a prolific number of exoplanets to date. The technique is based upon interpreting the orbital motion experienced

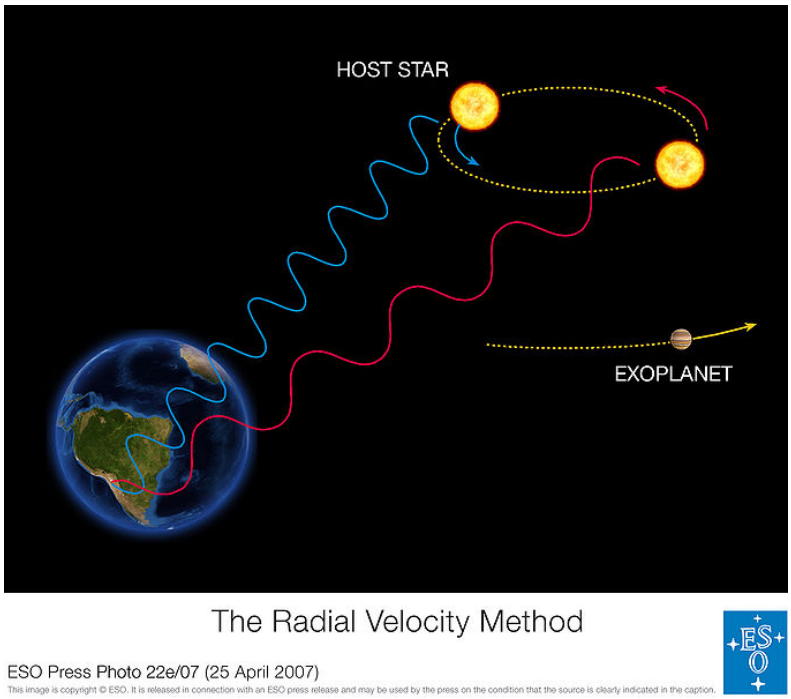


Figure 1.5: An image depicting the physical principles underlying the radial velocity method. As the star moves in an orbit around the planet-star system's common center of mass, it's spectrum is blue shifted when it approaches the Earth and is red shifted when it moves away. The extent of this Doppler shift bounds the radial velocity of the star and subsequently the product of the mass of the planetary companion and the system's orbital inclination. Image reproduced from the European Space Organization.

by the individual members of a binary or greater system of bodies (in fact the application to exoplanets is really an extension to the lowest companion mass limits in binary and multiple star systems). Radial velocity refers to the spectroscopic radial velocity of a star determined from Doppler spectroscopy of the star.

In the case of a planet orbiting a star the gravitational force of the star pulls the planet around in an orbit around a common center of mass of the system. However, the planet also exerts a gravitational force on the star and causes the star to move in an orbit around the same center of mass. If the planet-star system is not inclined in such a way that it appears

face on from Earth, there will be a radial component of the star's orbital velocity that will result in a periodic Doppler shift in its spectroscopy. As shown in figure 1.5, the spectrum of a star will blue shifted when it approaches the Earth and will be red shifted when it moves away. Using knowledge of the stellar parameters one can then produce a time series of the radial velocity of the star - a typical example of such a time series is given in the data of the star 51 Pegasi in figure 1.6. 51 Pegasi b was one of the first candidate exoplanets detected by this method [Mayor and Queloz, 1995]. Since detection of planets using this method is dependent upon gravitational perturbations from planetary companions and the distance from the related center of mass of the system, there is a bias towards finding planets are more massive and that have a larger orbital separation from the host star versus the transit method.

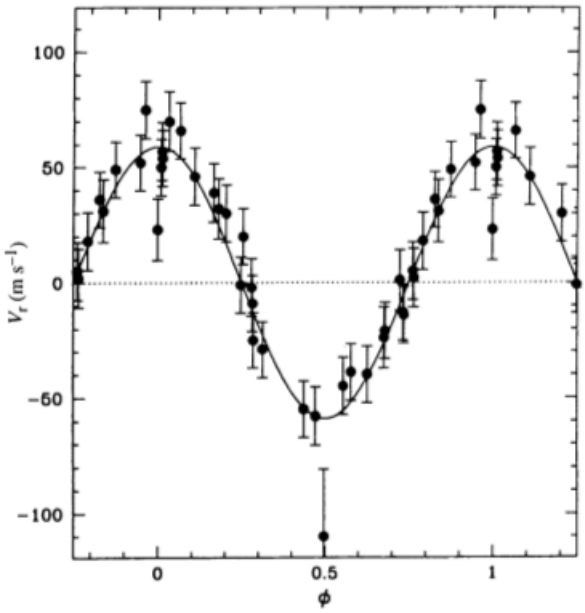


Figure 1.6: Time series data depicting the radial velocity of 51 Pegasi b over one purported orbital period. Data over several different orbits was overlaid and fitted with a line representing a short period circular orbit.
[Mayor and Queloz, 1995]

The most important unique derived planetary parameter obtained using the radial velocity method versus the transit method is the mass of the planet. While the transit method can constrain the volume of a planet, the radial velocity method can give an estimate of the minimum mass of the planet (and can constrain the product of the mass of the planet with its orbital inclination). In the case of a planet that can be identified and characterized by both the transit method and radial velocity method this means that not only can the inclination of the planet be constrained, but that using the measured mass and volume of the planet a bulk planetary density can also be estimated. Radial velocity confirmation of exoplanet candidates identified by the transit method is commonplace as the orientation of the star-planet system is likely to produce a measurable radial velocity amplitude if it is inclined in such a way as to produce a transit.

Another fundamental system parameter that the radial velocity method can constrain is the orbital period of the planet - this is extracted from the length of the periodic variation in stellar radial velocity time series. Finally, the direction of a planet's orbit can also be identified through a novel phenomenon called the Rossiter-McLaughlin Effect [Ohta et al., 2005] when both radial velocity and transit data of a system can be obtained. Radial velocity measurements taken during the beginning of a transit will deviate from expected value in different ways depending on whether the planet is moving in a prograde or retrograde orbit. If the planet is orbiting in a prograde direction it will first transit the portion of the star that is producing spectral lines that are blue shifted because that side of the star is turning towards the observer and then transit the portion that is red shifted as the star surface appears to recede. The opposite is true when the planet is in a retrograde orbit around the star.

One of the most important computational tools for radial velocity is an adapted and generalized Lomb-Scargle periodogram, a commonly used frequency analysis tool that can disentangle overlying signals in a time series even if the time series data is unevenly sampled [Zechmeister and Kürster, 2009]. Such extraction techniques can yield signals for multiple planets orbiting a star above a specific false alarm probability threshold. Due to the often

sparse and poorly spaced nature of radial velocity data, attempts to confirm planets in multiple planet systems can often result in disputed claims that are often only resolved with more data [Robertson et al., 2014]. Bayesian frameworks that use Monte Carlo Markov Chain fitting techniques have proven to be a critical recent advance in model selection for identification and characterization of planetary systems in radial velocity data [Tuomi and Jones, 2012, Nelson et al., 2014].

### 1.1.4 Other Detection Methods

While the transit method and radial velocity method account for the majority of exoplanets detected to date, there are a host of other detection methods which have been successful and which promise to yield more discoveries in the future. However, given the limited relevance of some of these detection methods to the work carried out as part of this thesis, this section will only offer brief descriptions of some of the most prominent ones. Some of the most exciting exoplanet detection methods which are likely to increase their share of discoveries in the next decade are direct imaging, astrometry and gravitational microlensing. The detection methods described in this section have been selected based upon their potential to yield new exoplanet detections due to coming missions and surveys that will utilize them - many of these methods have been detailed more extensively in Wright and Gaudi [2013]. For a more exhaustive description of exoplanet detection techniques there are a number of resources [Seager and Lissauer, 2011, Scharf, 2009, Mason, 2008] which go over different detection methods.

Direct imaging is the most intuitive of exoplanet detection methods but suffers from a number of observational problems that have limited its usefulness in the past. Exoplanets are very faint compared to their host stars and contrast ratios often exceed $10^6$-$10^7$ in visible light and are still $10^3$-$10^4$ in the infrared. In addition to these massive contrast ratios, the tiny separation between the host star and a planet versus the distance of the system from Earth means spatially resolving a planet from a star is also very difficult. However, what has made this technique more promising is the continued development of

coronagraphy techniques which block the light from the star and allow orbiting exoplanets to be observed. While this development has currently only been effective for large planets with large semi-major axes and for planets around young and very massive stars, even those bounds are being pushed and will continue to be stretched in the future.

Astrometry is another relatively intuitive exoplanet detection technique and physically is the inclined analogue of the radial velocity method. While the radial velocity method is most effective when the star and orbiting planet are aligned so that they are edge on when viewed from Earth, astrometry is most effective when the entire system is rotated 90 degrees and appears face on to an observer. Astrometry looks for periodic movement of a star in the sky that indicates it is orbiting a common system center of mass due to the presence of perturbing exoplanets. The spatial movement of the host star can be recorded as time series data and then analyzed and fitted for periodicities that are indicative of planets [Wright and Howard, 2009]. A significant issue for the technique is that ground based observatories do not have the precision to detect stellar position changes due to exoplanets. However, the space based observatory *Gaia* will be free of some of the atmospheric and systematic constraints limiting ground based telescopes and is expected to find somewhere between 20,000 to 70,000 exoplanets using astrometry [Perryman et al., 2014].

Finally, gravitational microlensing is an exoplanet detection method based upon the discovery that the amount of light deflected by gravity under general relativity was significantly greater than that predicted under Newtonian gravity. This method typically requires a configuration where an object such as an unbound planet or a planet hosting star passes in front of another star and amplifies its light. For an unbound star as the lens object, the amplification of the light from the star indicates that an object with a particular constrained mass has been detected. For a lens object that is a star hosting an exoplanet the typical lensing event will change shape and result in an atypical light curve where the brightening of the background star is not a simple monotonic increase and decrease. An example of the photometric signature of a lensing event where the lens is a star hosting a planet is given in figure 1.7. Gravitational microlensing events need densely crowded fields because

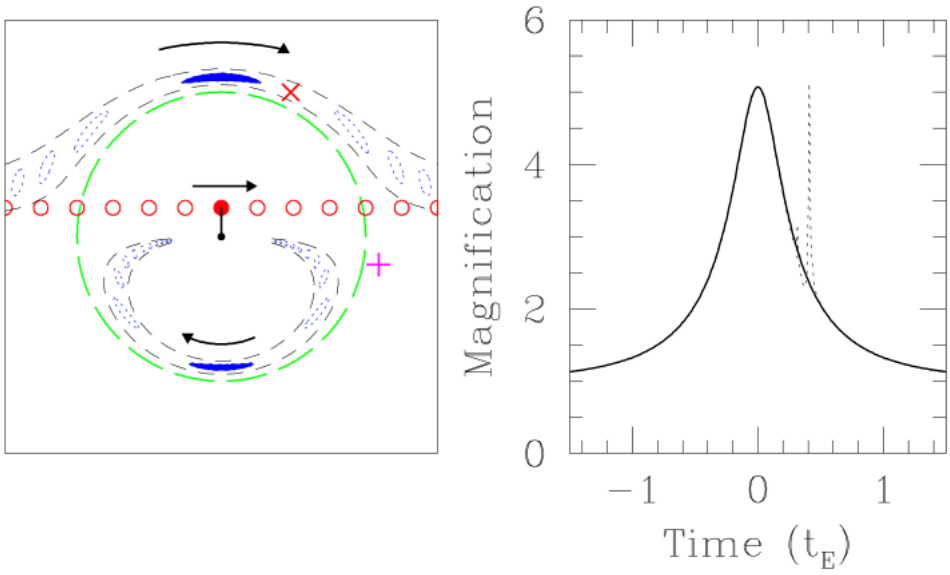


Figure 1.7: A diagram of a lensing event on the left. The moving source star is represented by the red circles and images produced are the blue dashed ellipsoids and solid ellipsoids. The image on the right shows the light curve from the star if there was only a lens star at the red x (solid line) and the additional spike if there was also a planet orbiting a star at the x (dashed line). Figure taken from Gaudi [2011]

the frequency of such events is rare - most searches are focused on the galactic bulge as a result. While this method has been able to detect a new class of free floating exoplanets and can probe a relatively under explored parameter space of bound exoplanets (lens planets need to be far enough away from their host star to produce an additional lensing signal), the extraction of planetary or even system parameters of detected exoplanets is difficult due to system and bulk planetary degeneracies. However, the *Wide Field Infrared Survey Telescope* is expected to find several thousand free floating and bound planets in the near future [Penny and Gaudi, 2014].

## 1.2 Exoplanet Statistics

A taxonomy of the exoplanets that have been currently detected reinforces the notion of diversity amongst these new worlds. Bound exoplanets have been found from right at the edge of their host stars [Charpinet et al., 2011] to distances so far out [Bailey et al., 2014] that they are only just barely bound to their star and capable of remaining so despite perturbations from other stars. The sizes of discovered exoplanets have ranged from the size of the Earth's moon [Barclay et al., 2013] all the way up to the tenuous line separating planets from brown dwarfs. Peculiar planets have been observed to be puffed up more than physical models can explain and yet on the other hand there have been planets detected that appear to be more compressible than can be explained by current models of planetary interiors. Orbital parameters vary incredibly and have yielded such oddities as planets on extremely inclined orbits, planets on extremely eccentric orbits, and planets orbiting in retrograde. Classes of planets have also started to emerge though even these are sprinkled with outliers such as the so called 'Godzilla' Earth rocky planet nearly twice the radius of the Earth [Fressin et al., 2011] and a gas dwarf whose mass is only that of the Earth's [Kipping et al., 2014]. Modeling of different types of planets has studied water worlds, carbon planets and a wide range of other environments. Exploring all the system configurations, different classes of planets, their dynamics, their physics, their interiors, surfaces and atmospheres would be an exhausting endeavor more fit for several conferences. Instead of attempting this herculean task, this section will instead look at some basic facts about exoplanets such as occurrence rates and general principles drawn about populations of planets while the next section will discuss some of the means used to characterize different planets.

The following discussion of occurrence rates will leave out the most frequent type of planet believed to inhabit our universe - free floating exoplanets not bound to any star. Microlensing surveys suggest that these types of planets are at least as frequent as planets bound to a star and actually may be an order of magnitude more prevalent [Sumi et al., 2011]. While these planets clearly are interesting in their own right, current detection methods limit any characterization of these planets beyond simple detection and the constraining

of a degenerate set of bulk parameters. The more interesting populations to evaluate for the purpose of this project are those planets which are gravitationally bound to a host star. The top line frequency of planets around main sequence dwarf stars is believed to be of order unity [Cassan et al., 2012]. This astounding number has been produced by taking into account selection effects of different detection methods and looking at the current census of discovered exoplanets. Many of these planets exist in multiple planet systems - indeed most methods that have detected an exoplanet have also found a multi-planet system. However, confirmation and validation of multiple planet systems can be fairly difficult statistically and as a result the occurrence rates for different multiplicities remains incomplete. While individual planets can inhabit very lonely parts of the parameter space of system and planetary characteristics, there have been several prominent types of planets which have been discovered.

Some of the most common planets in our solar system are planets, particularly gas giant planets, located beyond our snow line. However, the plot shown in figure 1.8 of the orbital period radius distribution of planets found by the *Kepler Space Telescope* appears to show that there is paucity of such planets. In reality this is due to selection effects. The ability to detect planets with larger orbital separations from their host star is hurt by the biases of the transit method to find close in planets and by the requirement for a long baseline of data using radial velocity methods to confirm long period planets that have masses significantly below the the brown dwarf/planet boundary. As a result, while preliminary efforts indicate that the probability density of gas giant planets is fairly flat as one goes out to about 2000 days, there is a still a lack of information regarding this class of planets due to observational incompleteness. Thankfully, missions such as *Gaia* and *WFIRST* are expected to be complementary to transit and radial velocity methods in terms of parameter space of exoplanets they will observe and are expected to discover thousands of farther out exoplanets.

While longer period planets are under observed, current detection methods and efforts have resulted in a nearly complete census of planets closer in - specifically for those planets

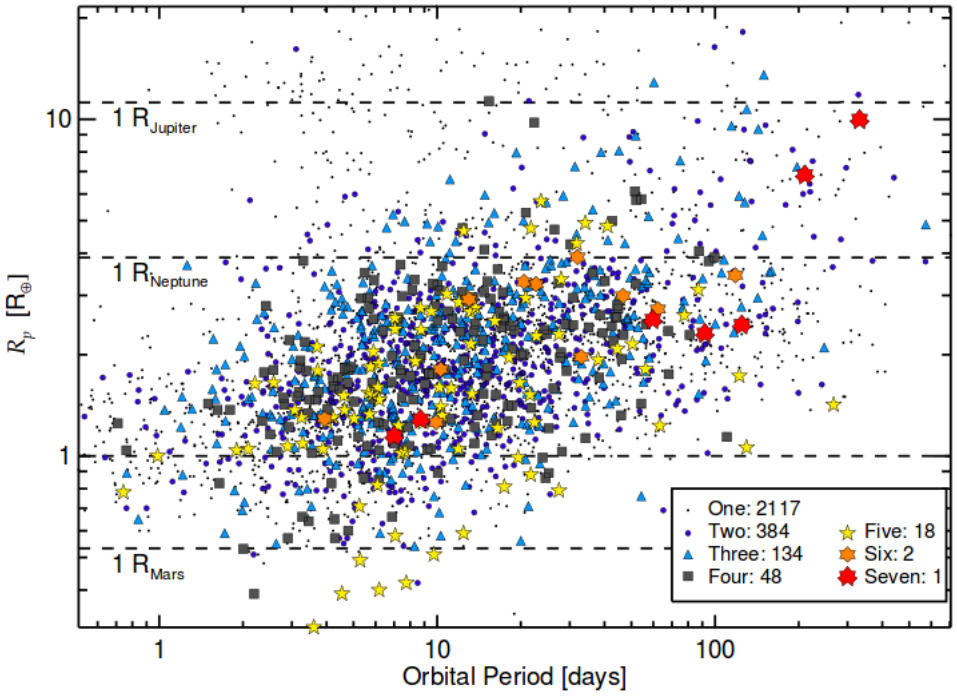


Figure 1.8: An image from Lissauer et al. [2014] which shows the distribution of planets found in the first three years of Kepler data as a function of orbital period and planetary radius. The apparent upward slope as a function of distance is believed to be a selection effect due to the difficulty of detecting small planets farther away using the transit method. The different shapes correspond to the multiplicity of the system - how many planets there are orbiting one system.

with orbital period less than 1 year around FGK stars. One of the striking features to come out of these surveys is the division of bound exoplanets into three main groups with respect to planetary radius [Buchhave et al., 2014]. The first is terrestrial or solid exoplanets that tend to have radii less than 1.7 $R_e$. The next are gas dwarf planets ($1.7<R_e>3.9$) with rocky interiors surrounded by a gaseous envelope of hydrogen and helium. Finally, the last set of planets are ice or gas giants with radii greater than 3.9 $R_e$.

These planets have different stellar class dependent occurrence rates for the distances where the data is complete or nearly complete. Specifically there is about 1 gas giant planet

with an orbit of less than several years around sun-like stars while that number jumps to about 1 out of every 2 stars for a system of smaller rocky planets. Occurrence rates for the highly sought after rocky planets in the habitable zone of a dwarf star are poorly constrained - estimates for range from a couple percent to over 30 percent with respect to the number of FGK class stars that host a solid planet or small gas dwarf in the habitable zone. One area of agreement though is that the smallest and most prevalent stars in our galaxy, M Dwarfs, are more likely to host a solid planet in their habitable zone [Winn and Fabrycky, 2014]. Part of this is because of the general rule that these smaller stars tend to also host smaller planets, but these systems also tend to be more compact and likely to host more compact systems of multiple planets. Either way, given the statistics of the number of stars in our galaxy, the number of planets orbiting those stars and the subset of those that may potentially be located in a habitable zone is staggering.

### 1.2.1 Close-In Solid Exoplanets: Occurrence and Significance

Finally, of particular interest to our work is the occurrence of planets very close in around dwarf stars. These planets are of special significance because the increased signal to noise of transit observations of such planets enables more thorough characterization of them versus more distant planets. Such planets are known to be rare [Howard et al., 2012] but tend to be preferentially detected because of their short periods and large signals in transit observations. In fact, one would get the impression that Hot Jupiters (gas giants very close to their host star) are surprisingly common given the distribution observed in figure 1.8. However, this is entirely due to selection effects and actual occurrence rates of Hot Jupiters between 0.1 and 1 percent around FGK dwarf stars. A hypothetical sample of the number of expected planets around the closest 1000 FGK dwarf stars that does take into account selection effects is given in figure 1.9. From here it is clear that planets very close in to stars are rare. However, given the observational bias towards finding such planets they are an important laboratory to explore their bulk and planetary properties - properties which can then allow for extrapolations for their more distant cousins.

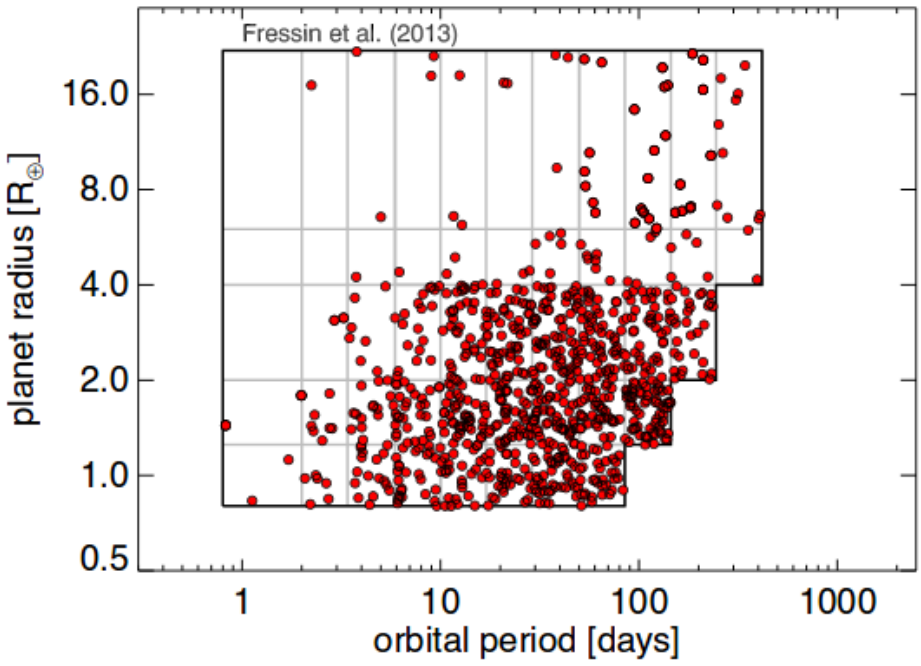


Figure 1.9: A hypothetical sample of planets around the closest 1000 FGK dwarf stars that takes into account selection effects. [Winn and Fabrycky, 2014]

This study is primarily concerned with very close in solid exoplanets - their additional observational potential due to their orbital separation and their rocky nature makes them unique probes into worlds that most resemble ours. These smaller planets produce larger transit signals due to their proximity and as a consequence provide less ambiguous characterization signals. General trends [Mulders et al., 2015] and estimates of close in solid planets in very short orbits around FGK dwarf stars appear to indicate they are slightly more common (∼1 percent) than Hot Jupiters [Sanchis-Ojeda et al., 2014, Dressing and Charbonneau, 2013, Howard et al., 2012]. There are fewer occurrence rates estimates for these planets around those stars most likely to host them (M dwarfs) due to a focus on FGK dwarf stars, however Dressing and Charbonneau [2015] find an occurrence rate between 0.30 and 0.75 percent for potential small solid planets on sub 1 day orbits as part of their larger calculation of occurrence rates around M dwarf (see figure 1.10). Given the raw statistics of

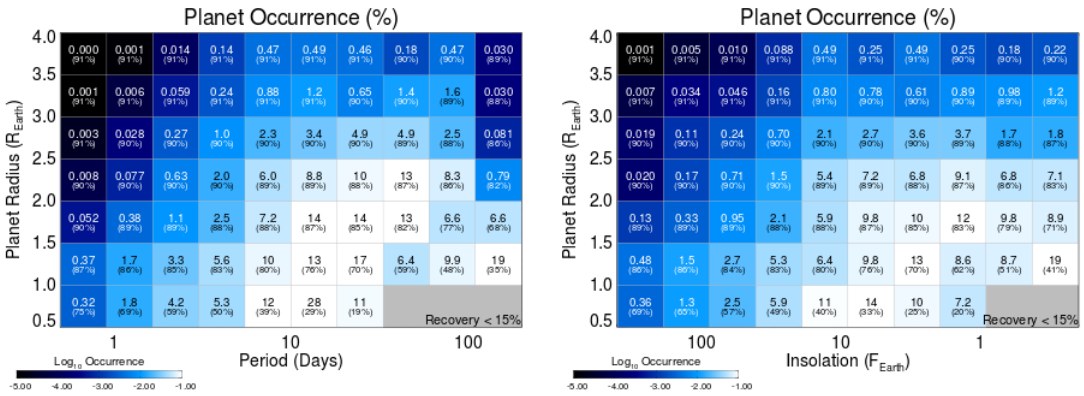


Figure 1.10: Planet Occurrence rates around M Dwarfs as a function of Planetary Radius and either Orbital Period or Insolation [Dressing and Charbonneau, 2015]. The top number is the percentage occurrence rate while the bottom is the pipeline recovery rate of simulated injected planets. Of note are the planets with radii less than 2.25 $R_e$ and orbital periods of less than one day.

stars that will be observed and planets expected to be detected using the transit method, it appears there will be a number of candidates that have already been found and that are likely to be found that will be relevant to the topics that were studied as part of this dissertation.

## 1.3 Characterization of Exoplanets

Characterization of exoplanets beyond basic detection is often done by using different detection and characterization techniques in tandem. As mentioned before, basic orbital and bulk properties such as inclination, mass, radius and density can be obtained by combining transit observations with radial velocity observations of an exoplanet. Particularly interesting for the work studied here is that transit photometry of an exoplanet often can yield far more information about an exoplanet beyond just an estimated radius and period.

Multi-band transit observations can not only ascertain the planetary nature of a transit but can also help characterize the atmospheres, surfaces and interiors of such planets. In

some cases, the varying reflectivity of a planet at different points in its orbit can be captured as ellipsoidal variations in the planet's light curve and in the secondary eclipse of the system when the additional light from the planet is obscured when it is blocked by the host star. These variations can then be fitted and interpreted (though not limited to) as a number of different phenomena: 1) Different reflectivity of haze layers, clouds, or variations in temperatures of an atmosphere 2) Varying surface albedo of an exoplanet due to different composition or topography 3) Asphericity of a planet due to oblateness of the planet or tidal distortion from external forces.

In addition to that, transmission and emission spectroscopy using either multi band photometry or spectroscopy can serve as an additional probe of a planet. As a planet passes in front of its host star it will block some of the light from the star but its atmospheric annulus will also act as a filter for light passing through it. Depending on the composition, structure and dynamics of the atmosphere the resulting spectrum can show absorption bands or general trends that can help to characterize the atmosphere. Additionally, right before the planet appears to disappear behind it's host star during secondary eclipse some of the light emitted from the portion of the planet's atmosphere illuminated by the star can appear as additional signals in the emission spectroscopy of the planet. This can also then be used to characterize the atmosphere of the planet. A diagram showing the orientation of the planet in these positions is given in figure 1.11. Interpretation of these spectra has reached astounding lengths - breakthroughs have included constraining of atmospheric constituents [Lecavelier Des Etangs et al., 2008, Mandell et al., 2013], determining whether an atmosphere is dominated by clouds or a haze layer [Bean et al., 2010], and evidence of winds in an exoplanet atmosphere [Miller-Ricci Kempton and Rauscher, 2012]. A final additional probe of a planet's atmosphere is the potential to view starlight that has been polarized as it passes through the atmosphere - polarimetry has been used to identify likely Rayleigh scattering in the atmosphere of an exoplanet [Berdyugina et al., 2011].

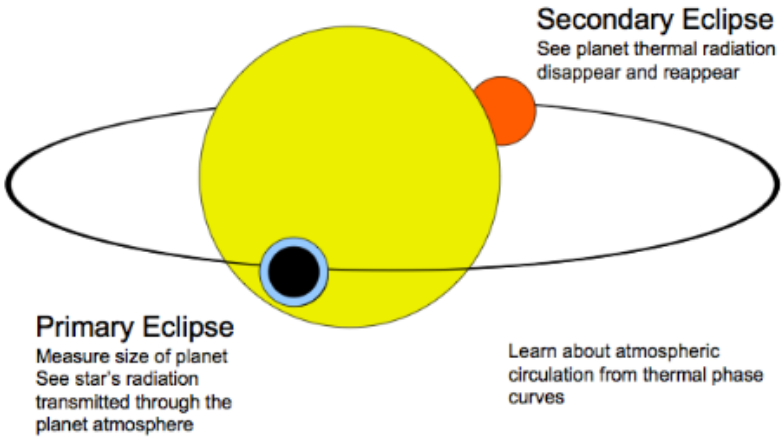


Figure 1.11: A diagram illustrating the primary eclipse and secondary eclipse during transit observations. During the primary eclipse some of the star light passing through the atmosphere of the planet can be absorbed. Right before secondary eclipse the illuminated portion of the planetary atmosphere can produce an additional emission. Both these features can act as a probe of the atmosphere through the transmission and emission spectra respectively. Finally, the changing thermal phase curve of the planet can also act as a probe of the circulation of the atmosphere or albedo of the surface. [Seager and Deming, 2010]

### 1.3.1 The Study of Exoplanet Bulk and Interior Characteristics

Due to the relatively nascent state of observational characterization of exoplanets, most interior and and some surface characterization has mostly involved theoretical modeling work. Basic bulk density can be explored in cases where planets can be observed using methods that independently constrain mass and volume. However, any composition or interior models suffer the difficulty of significant degeneracy since the interiors of planets may be composed of an unknown number of layers with varying densities [Valencia et al., 2006, Fortney et al., 2007]. While there has been some suggestion that knowledge of planetary mass, radius and stellar elemental abundances may be able to constrain core size [Dorn et al., 2015] and in some cases measured oblateness has been used to constrain core size for certain gas giants [Zhu et al., 2014] (this technique has yielded success in our solar system),

this degeneracy remains mostly unsolved and a significant issue in interior characterization. As a consequence, development of models of planetary interiors and surfaces that are merely plausible given relevant physics has dominated with respect to the different types of planets that may exist - these models include but are not limited to waterworlds [Kuchner, 2003, Léger et al., 2004], carbon planets [Madhusudhan et al., 2012] and lava worlds [Henning et al., 2009].

A major component of the study of exoplanet interiors has also been a focus on modeling of the interior layers of exoplanets using appropriate equations of state for suitable materials [Wagner et al., 2012, Gong and Zhou, 2012]. Given the high pressure and undetermined compositional nature of these interior environments, there is interest in experimental parameterization of equations of state for solid materials expected to make up planetary interiors at ranges of pressures and densities that would conform to those expected to exist in planetary interiors. Much of this work is based on or ancillary to exploration of equations of state and interior modeling for planets in our own solar system [Baraffe et al., 2014].

One other central question in the area has been the nature of convection in the interior of exoplanets. The Earth is continuously resurfaced by a 'mobile lid' convection regime that results in the plate tectonics that has been responsible for continental drift and much of the volcanism seen on the planet. In general, the convection regime for a planetary interior is critical for cooling, resurfacing, climate mediation and potentially habitability of a planet. As a consequence, the ability to determine which planets possess Earth-like mobile lid convection processes versus 'stagnant lid' regimes devoid of plate tectonics (seen on the smaller terrestrial planets in our solar system) is a critical question with respect to understanding present planetary conditions and well as evolutionary history. Interestingly, while there is agreement on many of the controlling factors (planetary radius, insolation, internal temperature upon initial formation, etc.) in determining the nature of interior convection, there is still significant disagreement on whether plate tectonics is inevitable for a number of different solid bodies [O'Neill and Lenardic, 2007, Valencia et al., 2007a].

### 1.3.2 The Study of Exoplanet Surface and Atmospheric Properties

Exoplanet surface and atmospheric properties can often be difficult to disentangle using current observational methods. Part of this is due to uncertainty regarding the structure of atmospheres and their subsequent influence on atmospheric and surface information retrieval. As a result, exoplanet surfaces largely remain a poorly characterized domain in observational studies. Pathways may exist for characterization of surfaces in specific cases or using multiple observational techniques. For rocky planets tidally locked to their host star, night side reflected light or surface emissions my yield surface information in a region where atmospheric collapse has occurred. It may also be possible to extract surface information using a combination of reflected light and thermal emission from a planet in conjunction with transmission spectroscopy [Hu et al., 2012]. In this case, transmission spectroscopy would provide observations of an atmosphere that may enable surface characterization.

As a result of the current limits on observationally constraining exoplanet surfaces, a portion of exoplanet literature tries to explore exoplanet surfaces through the use of modeling that applies physical principles related to the environments those planets likely inhabit. Some of this work explores the interaction of the the stellar environment a planet is exposed to with the interior modeling of the planet based upon bulk and orbital properties. These analyses can provide insights with regard to exoplanet surfaces and suggest some surprising outcomes. Indeed such work has suggested that planets with significant tidal heating and a high level of stellar insolation may possess significant lava oceans and resurfacing processes [Henning et al., 2009, Léger et al., 2011] and even significant volcanism [Barnes et al., 2010]. However, even in such cases the detectability of these extreme surface features or their consequent atmospheric signatures is right at the edge of current observational limits [Kaltenegger et al., 2010].

The complication of retrieving information about exoplanet surfaces is often a result of confounding signals from a planet's atmosphere - the upshot of this is that the observational study of exoplanet atmospheres is a burgeoning area with respect to exoplanet

characterization. While this study of atmospheres is still limited by observational considerations [Hansen et al., 2014, Hoeijmakers et al., 2015] as well as gaps in the understanding of physical and chemical processes [Lewis et al., 2014], there are a number of observational techniques which have been used to probe the structure, dynamics, composition and chemistry of exoplanet atmospheres in combination with modeling. In fact at this point, the field of exoplanet atmospheres possesses a substantial body of literature consisting of a range of analytical techniques, observational techniques and modeling that have yielded a number of interesting findings. As a consequence the following description of the field will only focus on a brief overview and some highlights - for a more exhaustive view of the field there are several reviews available which describe the current state of field more comprehensively [Madhusudhan et al., 2014, Burrows, 2014].

The main tools used to explore exoplanet atmospheres have been interpretation of multi-band transit photometry and the use of spectroscopy to obtain transmission and emission spectroscopy of targeted exoplanets. Multi-band and single band photometry studies make use of the full phase curve and secondary eclipse portions of a light curve in addition to the main transit, while both photometry and spectroscopy techniques combine observational results with atmospheric modeling in order to enable interpretation. There have been some notable findings using other observational techniques such as the identification of the rotation rate of a directly imaged exoplanet beta Pictoris b using spectroscopy [Snellen et al., 2014]. However, the vast majority of atmospheric characterization of exoplanets to date has come from those few, main methods.

Successes in atmospheric characterization have primarily came in the ability to identify a number of different but related atmospheric features in individual planets (typically for close-in gaseous planets). These can broadly be categorized as features regarding atmosphere structure and dynamics, atmospheric composition including opacity and chemistry and finally the characterization of clouds and hazes. All of these features are obviously related and interpretation of the individual attributes of an atmosphere along with more holistic examinations of planetary atmospheres has been furthered by a substantial body of

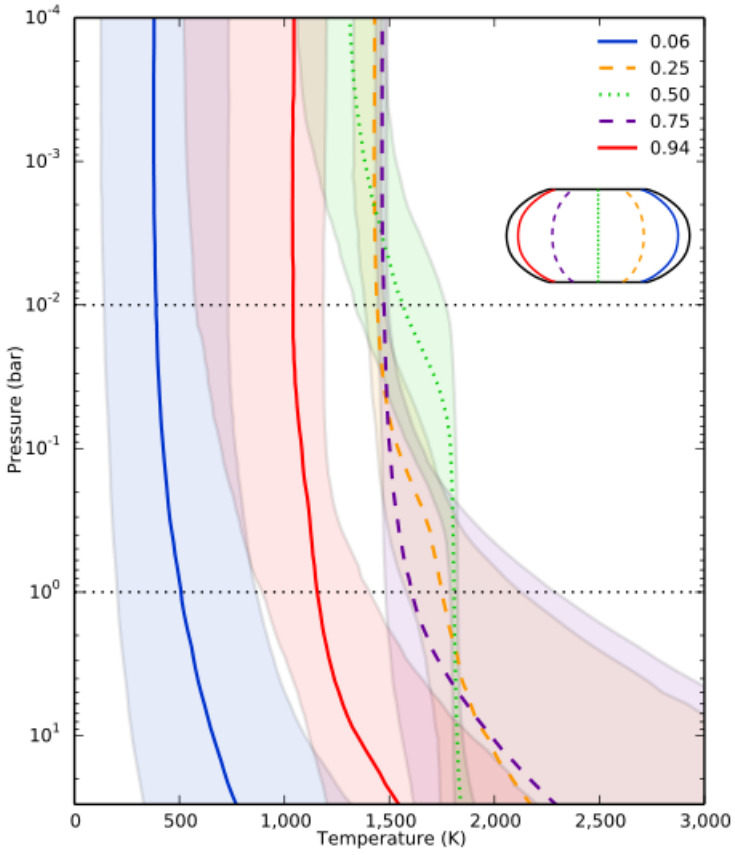


Figure 1.12: Image of inferred thermal and pressure structure of the atmosphere of WASP-43b taken from Stevenson et al. [2014b]. Pressure-profiles are parameterized from a combination of phase resolved emission spectroscopy measurements along with climate modeling for the planet and are plotted with $1\sigma$ uncertainty regions around median values.

climate modeling for exoplanet atmospheres.

Characterization of atmospheric structure and dynamics has focused on the pressure-temperature structure of an atmosphere and some of the dynamics that may be observable for such atmospheres. Studies have been able to explore both the vertical and horizontal pressure-temperature space for exoplanets from phase curve and secondary eclipse observations using multi-band photometry and using spectroscopy. An especially exciting example of this is the mapping of Hot Jupiter WASP-43's thermal structure using spectroscopic thermal emission measurements taken as a function of phase [Stevenson et al., 2014b]. Figure

1.12 shows the inferred thermal structure of the atmosphere as a function of longitude. In addition, coarser broadband measurements have also been able to provide evidence both for [Machalek et al., 2008, Knutson et al., 2009] and against [Diamond-Lowe et al., 2014] thermal inversions in individual exoplanets, suggest circulation/heat distribution bounds [Cowan et al., 2007, Wong et al., 2014] and identify superrotation in an atmosphere (including anomalously high values as in Crossfield et al. [2010]. Fascinatingly, photometry of Brown Dwarfs has even been used to track evolving atmospheric cloud features on those bodies [Radigan et al., 2012], suggesting that 7 day forecasts of the weather on certain exoplanets may not be too far off.

Detection and characterization of the composition of exoplanet atmospheres has obvious appeal. For planets that are habitable, molecular and atomic detections may be one of the best ways of identifying life. Spectroscopic observations of Earth's atmosphere using light reflected off of the moon suggests that detection of biogenic $O_2$, ozone and water vapor may be achievable using next generation ground based telescopes [Arnold et al., 2014]. Even more generally, detection of specific molecules can lead to insight into atmospheric structure, dynamics, radiative transfer processes that control formation of clouds and hazes and chemistry.

The ability to constrain general composition of an atmosphere [Swain et al., 2014, Fraine et al., 2014] is an obvious motive for such research - yet it has not necessarily been the most important finding of such work. Detection or non-detection of certain constituents or their enhanced opacities have placed constraints on the potential for temperature inversions [Sing et al., 2013, Bento et al., 2014], detection of certain atomic species have enabled estimates of atmospheric escape [Bourrier et al., 2015] and shifted absorption lines of other molecules have even been suspected to be signals of winds in the upper atmosphere of an exoplanet [Wyttenbach et al., 2015]. Radiative processes in atmospheres can also be probed by detection and abundance constraints of key atmospheric constituents [Nikolov et al., 2014]. In some cases, detection or non-detection of certain absorption features can suggest the existence of certain scattering models [Stevenson et al., 2014a] and/or of clouds

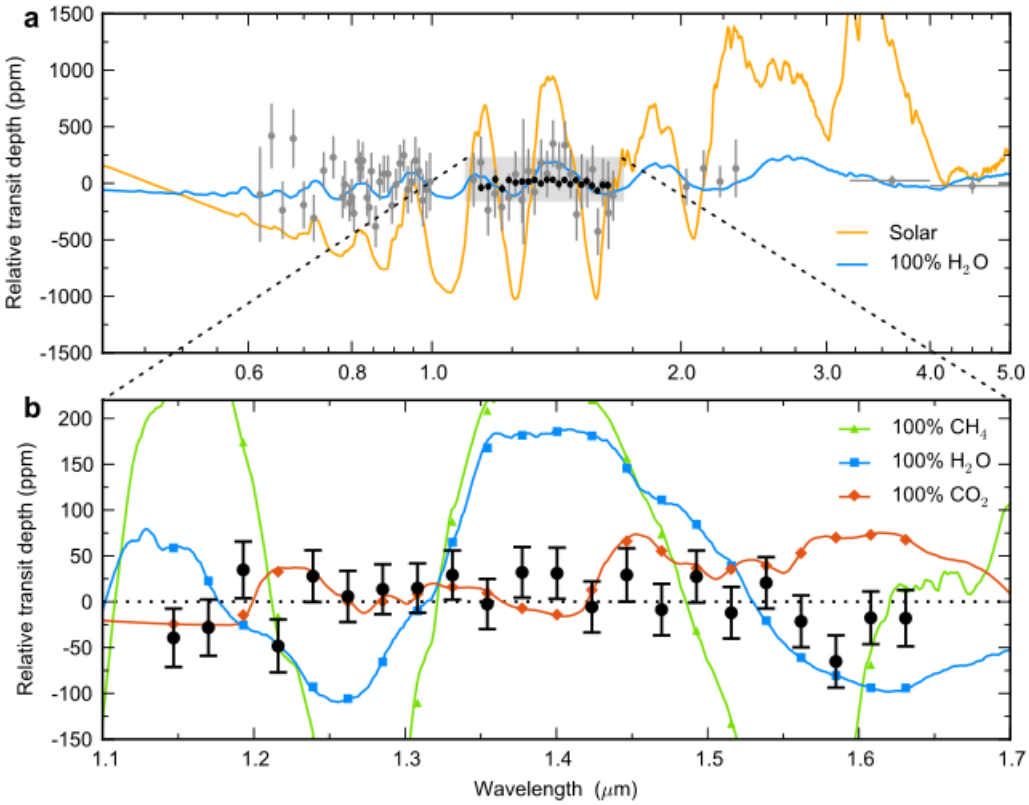


Figure 1.13: Near-infrared transmission spectra of GJ 1214b from Kreidberg et al. [2014]. The data points are overlaid with models for atmospheres with high mean molecular masses. The poor agreement between the data and models suggest the likelihood of clouds in the atmosphere of the planet.

and hazes [Deming et al., 2013]. A notable example of the latter is the non-detection of the features of a high mean molecular atmosphere in the near-infrared transmission spectrum of Super Earth GJ 1214b [Kreidberg et al., 2014]. This non-detection, shown in figure 1.13, indicates the presence of clouds in GJ 1214b's atmosphere.

Finally, in addition to the use of modeling to interpret observational signals there also exists a large body of literature that uses pure modeling efforts to elucidate some of the physical and chemical properties of exoplanet atmospheres. Three dimensional idealized general circulation models have been used to explore structure and dynamics over a large

phase space of bulk parameters [Showman et al., 2015, Kaspi and Showman, 2014] and have been used to identify novel potentially observable features of certain atmospheres [Miller-Ricci Kempton and Rauscher, 2012]. A large of array of simpler models also explore different physical features and mechanisms that may exist for exoplanet atmospheres and even examine processes related to atmospheric chemistry [Agúndez et al., 2014] or interaction with a biosphere [O'Malley-James et al., 2014]. Some of these models even come full circle by simulating atmospheres and then producing potential observational signatures for their results [Fortney et al., 2006].

## 1.4 The Observational Advantage and Relevance of Close-In Solid Exoplanets

The projects that constitute this thesis focus on the processes that occur on and the observables that can be extracted from close-in solid exoplanets. Occurrence rate estimates from section 1.2.1 indicate that these are not very common planets - at least based upon yields from past and current exoplanet detection efforts. However, these previous and current searches have mostly looked for exoplanets around stars less likely to possess close-in exoplanets. More importantly, the characterization value of each close-in solid exoplanet found is arguably much greater than that of their farther out analogues. Part of this is due to the higher precision of the planetary signal that is extractable from their observational data - this is a product of the fact that a transiting close-in solid planet will have a shorter orbital period than a further out counterpart. The ability to analyze the subsequent larger sample of transits in similar periods of time allows for more rigorous detection of system and planetary features.

Additionally, these closer in planets will also exhibit different physical phenomena due to the extreme stellar insolation and gravitational environment they are in. These features - such as much higher atmospheric temperatures or even asphericity effects are preferentially

observable to analogous features farther out. The exploration of Hot Jupiter planets is a testament to the utility of closer in planets which possess extreme physical environments. The lessons learned from studies of these close-in giant planets have been invaluable for learning general lessons about exoplanets and their more distant cousins. Thus the real promise of these close-in worlds is that they provide the most realistic pathway to characterizing solid planets such as our own.

It is important to note however that the observationally advantageous nature of these extreme features do also lead to some lessons which are only really applicable to a limited class of exoplanets. However, understanding what the extent is of the types of exotic process that exist on exoplanets is an important part of learning about the diversity and evolution of our and other solar systems. Additionally, often processes that appear be restricted to exotic environments end up having applications to more familiar environments. The catalytic destruction of Ozone in the Venusian atmosphere and it's importance in understanding the past destruction of the Ozone layer on Earth is an important reminder of that. Thus the projects carried out as part of thesis that are described in the following sections examine these close-in solid planets with respect to some of the exotic processes that may be occurring on these worlds - processes that will influence our understanding of this class of planets, solid planets in general and the diversity and evolution of all exoplanets.

# Chapter 2: Atmospheric Mass Transport on Close-In Solid Exoplanets - Atmospheres that Move and Mold Planets

This project describes the atmospheres of close-in solid exoplanets using a low dimensional model which is then used to explore atmospheric mass advection. The resulting atmospheric mass transport results are compared to different critical timescales and other processes which effect the distribution of mass on these planets. Those comparisons are used to inform potential observational signatures on the planets and the potential for resurfacing on these planets to alter their gravitational potential.

## 2.1 Introduction

The modeling of the atmospheres of solid exoplanets has become an important facet of exoplanet research. These models explore the nature of such atmospheres across a wide range of parameters and in varying degrees of complexity [Leconte et al., 2014, Showman et al., 2013]. A substantial portion of this research has specifically been devoted to examining the atmospheres of potentially habitable exoplanets in addition to general studies which examine the structure and dynamics of atmospheres of solid exoplanets across a large phase space of orbital and bulk parameters. A critical question with respect to habitability and the persistence of an atmosphere is stability of an atmosphere against collapse [Heng and Kopparla, 2012, Wordsworth, 2014]. This is especially important considering that many solid planets are expected to be found around M dwarfs - and studies have found that the habitable zone around those stars may coincide with an orbital distance where planets may become tidally locked. As a consequence, these planets may experience long term or permanent dayside/nightside contrasts that can affect habitability. While recent research suggests that solid planets in the habitable zones of M dwarf stars may be able to break

free of synchronous rotation that creates a permanent dayside and nightside [Leconte et al., 2015], there is still uncertainty regarding the rotation of planets closer in. In fact, recent research suggests that simply using a more realistic tidal response, a significant fraction of solid planets that are close-in fall into higher order resonance orbits versus synchronous rotation [Makarov and Efroimsky, 2013]. This is an important question because at minimum, these planets must possess synchronous rotation for their farther out counterparts to be likely to do so. Additionally, these very close-in solid planets are also likely to be the most observationally accessible and characterizable of solid planets using their phase curves and transit spectroscopy. As a result it is critical to explore the atmospheres of these extreme worlds and determine what atmospheric processes may exist that may produce extreme phenomena and observable features. Such modeling should inform observations of these planets - this in turn will help in characterization of the larger group of solid exoplanets.

There is already a small body of literature which has examined the atmospheres of these close-in and very hot solid exoplanets. One important open question regarding these planets is the initial state of their gaseous envelope - whether they have always been volatile-poor rocky planets or whether they are the evaporated remnants of volatile-rich gaseous planets [Jackson et al., 2010]. The present state of the atmospheres on these planets is dependent upon the evolution of volatiles from their initial state - an important fact when combined with the compositional degeneracies that currently exist for such planets when looking at bulk density [Valencia et al., 2010]. However, there are good reasons to believe most of these very hot planets are free of volatiles such as H, He, C, N, S, F, Cl, etc. If these planets originally formed close-in, disk temperatures were likely too high so far in from respective snow lines to allow for significant volatile accretion. Even if these planets were formed farther out, accreted significant volatile envelopes and migrated to their current position, volatile loss processes suggest that most of these close-in solid planets possess volatile poor atmospheres. Mass loss rates for such planets are extremely high [Perez-Becker and Chiang, 2013] - to the extent that a purely gaseous planet the size of Corot-7b would evaporate within 5 Gyr for a heating efficiency that only requires 15 percent of incoming stellar radiation to

drive escape [Ehrenreich and Désert, 2011]. Planets in these stellar radiation environments are highly unlikely to possess H/He envelopes just from thermal escape arguments [Elkins-Tanton and Seager, 2008] and Extreme UV and X-Ray radiation driven escape is expected to be significant for the remaining heavier volatiles [Lammer et al., 2013, Owen and Wu, 2013]. As a result, these planets are expected to possess thin volatile-poor atmospheres dominated by heavier constituents such as alkali and metal elements and compounds along with molecular oxygen and oxygen compounds from vaporized crustal lava [Schaefer et al., 2012].

Simulations of just such atmospheres have included studies of composition and vapor pressure by borrowing from models that looked at high temperature lava vaporization for solar system bodies. An adaptation of the MAGMA model [Fegley and Cameron, 1987] that was used to simulate lava vaporization on Io [Schaefer and Fegley, 2004] has been extended to apply to hot close-in solid planets - specifically hot Super-Earths. The MAGMA model uses the equilibrium between gas and vapor in a magma exposed to high temperatures in order to calculate the outgassed atmospheres produced by such vaporization. An examination of the atmospheres of these close-in Super Earth's using that model indicated that those planets' atmospheres were likely to be dominated by metals and metalloids that would result in thin silicate atmospheres [Schaefer and Fegley, 2009]. It also suggested the compositions the model produced may also give rise to metallic clouds, though later work has claimed that such atmospheres are too thin to support such clouds [Léger et al., 2011]. A later study [Miguel et al., 2011] that looked at the census of Kepler candidates at that time further organized those hot Super-Earth atmospheres into 5 different categories that were divided by the effect of surface temperature on composition. Those categories are given in table 2.1 - they indicate that the dominant constituents for these very hot planets are typically Na, $O_2$, O and SiO with relative abundances that are sensitive to temperature.

Table 2.1: Hot Super-Earth Atmosphere Classification

| Hot Super-Earth Atmospheres[1] | | | |
|---|---|---|---|
| Atmosphere Type | Temperature Range (K) | Dominant Constituents[2] | Examples[3] |
| 1 | T < 2033 | Na, $O_2$, O, Fe | Kepler-11b, Kepler-23b, Kepler-101c |
| 2 | 2033 < T < 2588 | Na, $O_2$, O, SiO, Fe, Mg | CoRot-7b, Kepler-9d, Kepler-33b |
| 3 | 2588 < T < 2890 | Na, $O_2$, O, SiO, Mg, Fe | Kepler-21b, Kepler-65b, Kepler-323b |
| 4 | 2890 < T < 3168 | Na, SiO, $O_2$, O, Mg, Fe | K03242.01, Kepler-10b |
| 5 | T > 3168 | SiO, $O_2$, O, Na | K03204.01, 55 Cnc e [4] |

[1] Category types taken from Miguel et al. [2011]

[2] Listed in order of abundance

[3] Example planets based on temperature calculated for sub stellar point with albedo equal to zero

[4] Observational estimates suggest a bulk density for this planet which may not be compatible with the composition assumptions made for this classification scheme

A study of CoRot-7b, the first Super-Earth to have both it's mass and radius constrained in order to produce density estimates, included sections on the atmosphere and surface

environment of the heated Super-Earth [Léger et al., 2011]. That study echoed the results from those general studies by predicting an extreme environment on the planet that included a strong dayside-nightside temperature contrast due to synchronous rotation, a large sub stellar lava ocean and a thin, cloudless metal-dominated atmosphere that was also restricted to the dayside. As will become apparent in the following sections, some of the assumptions used in and extant physical phenomena suggested by that work are generalized and included in this project. Finally, the study of atmospheres of close-in solid planets has also been heavily informed and explored by two other critical papers. The first study carried out as part of this thesis extends the low dimensional atmospheric model developed and used in those papers in order to explore the atmospheres and the nature of atmospheric mass transport on these planets. As a result, some of their main results are described in the following sections in order to relate the motivation behind this project before a description of the methodology used in the research.

### 2.1.1 Supersonic Meteorology of Io

The most thorough model to date of the atmosphere of a hot close-in solid planet is unsurprisingly based upon a study [Ingersoll et al., 1985] that originally focused on a solar system object - Jupiter's moon, Io. In that work, Ingersoll, Summers and Schlipf examined the horizontal flow of $SO_2$ from Io's dayside to nightside by solving conservation equations of mass, momentum and energy for temperature, pressure and horizontal velocity as a function of solar zenith angle. The hydrodynamic vertically integrated one dimensional model examined an atmosphere that had a horizontal pressure gradient that was due to varying sublimation vapor pressures produced by spatially varying surface temperatures. The model incorporated boundary layer interactions between the surface and atmosphere and calculated the flow pattern and resurfacing processes of the atmosphere.

Several basic assumptions underpinned the model:

- The temperature of the $SO_2$ frost can be calculated from radiative balance arguments. The atmosphere has minimal effect on the surface temperature as latent heat

contributions are small compared to insolation.

- The molecules of the atmosphere behave as a continuous fluid that is hydrostatically bound to the body. For this to be true the mean free path of the particles must be less than the atmospheric scale height, the atmospheric scale height must be less than the planetary radius and the kinetic energy of the flow must be less than the binding energy of the body. All of these are met in Io's case.

- The horizontal velocity and entropy per unit mass can be treated as constants with respect to the vertical axis - a simplification that requires turbulent flow to be true. This is also well held as the Reynolds number is large over most of the flow (with the exception of a thin layer near the top of the atmosphere and in the thin boundary layer area). Additionally, the turbulent diffusion time is short compared to the distance the flow travels - enabling it to be considered as well mixed to first order.

- There is substellar and antistellar axis symmetry and rotation can be neglected. This requires the rotation rate to be smaller than V/r. This is true for a first approximation.

These critical assumptions underpin the model for Io and were also used in the application of the model to hot Super-Earths. The thesis project described in this section that builds upon this model also uses the same assumptions and will justify their use in the methodology section.

While the model was the essential part of this paper with respect to its application to exoplanets - something that will be apparent from the following section - there were some fascinating results that are also relevant to the project that was conducted for this thesis. The two most prominent ones were the existence of supersonic flow of $SO_2$ from the dayside to the nightside and the indication of significant atmospheric mass transport at low and mid-latitudes.

### 2.1.2 Atmospheres of Hot Super-Earths

The atmospheric model developed in Ingersoll et al. [1985] was extended to study the atmospheres of Hot Super-Earths in Castan and Menou [2011]. This work marked one of the first studies that looked at the structure and dynamics of the atmospheres of these very hot and solid worlds - an important effort considering that these planets would be at the forefront of solid planet characterization.

The study focused on the hydrodynamics of the atmospheres of CoRot-7b, Kepler-10b and 55 Cnc e. The methodology used to solve for the atmosphere was very similar to Ingersoll et al. [1985] with the main difference being a different numerical technique to solve the system of equations, the addition of the magnetic effects in the form of magnetic drag and ohmic dissipation parameterized as an additional term in the momentum and energy flux from the ground to the atmosphere, and a surface temperature and dominant constituent profile appropriate for hot close-in solid planets taken from literature.

The results also mirrored those obtained when modeling Io's atmosphere - Castan and Menou [2011] found hot, tenuous atmospheres that exhibited a transition to supersonic flow in each planet's atmosphere near  40 degrees and also saw the potential for significant atmospheric mass transport given that there was significant condensation  20 degrees past the transition to supersonic speeds. Their discussion of the potential for such atmospheric mass transport to influence the gravitational potential of these planets served as the impetus for the research carried out here which examines the magnitude of such resurfacing. The initial work carried out as part of this project included replicating some of the results of Castan and Menou [2011] - particularly the ability to reproduce pressure and velocity values for the atmospheres of interest given in figure 2.1 and 2.2.

## 2.2 Methodology

The overall structure of the model for this project entailed building the atmospheric model from Ingersoll et al. [1985] and applying it to close-in solid planets in order to measure

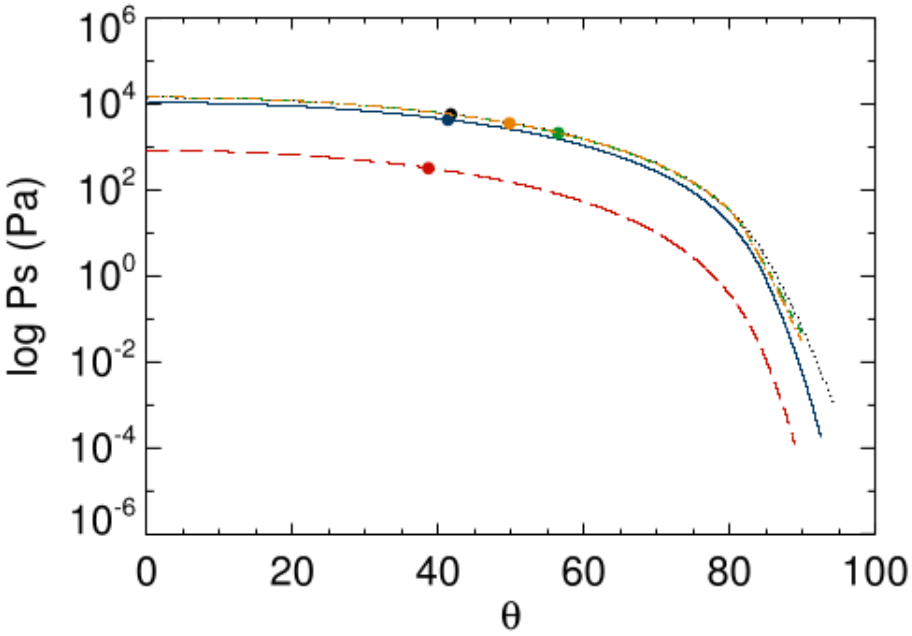


Figure 2.1: The atmospheric pressure as a function of angle away from the substellar point for CoRot-7b (red), Kepler-10b (black) and 55 Cnc e (blue). The yellow and green dashed lines are for Kepler-10b with magnetic effects included. Dots represent the location of the sonic point where the flow transitioned from subsonic to supersonic. Image taken from [Castan and Menou, 2011].

resurfacing processes and their subsequent consequences. This 1-D model is used to first replicate the results from Castan and Menou [2011] and is then extended in order to measure deposition rates past the sonic point of atmospheric flow on these planets. These deposition rates are then compared to the extent of putative magma oceans [Léger et al., 2011] in order to estimate the extent of resurfacing to parts of a planet where cycling mechanisms are too slow to effectively bring back preferentially transported materials. This resurfacing is then examined with respect to potential ramifications for planetary shape and spin as well as in order to probe potential observational signatures.

Current limitations on observational characterization of the planets relevant to this study as well as limited understanding of atmospheric properties in such extreme irradiation environments support the use of a low dimensional model based on simple and dominant

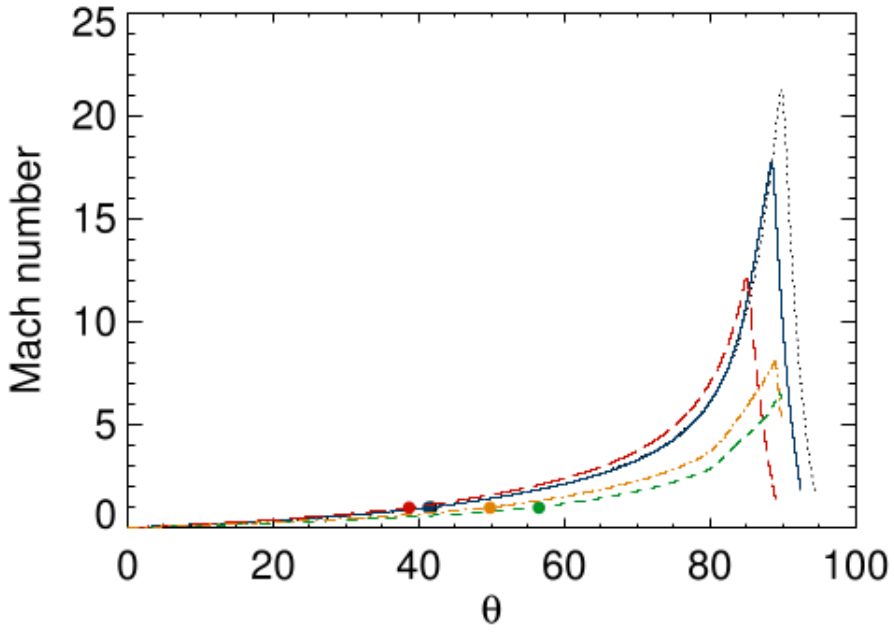


Figure 2.2: The atmospheric horizontal velocity as a function of angle away from the sub-stellar point for CoRot-7b (red), Kepler-10b (black) and 55 Cnc e (blue). The yellow and green dashed lines are for Kepler-10b with magnetic effects included. Dots represent the location of the sonic point where the flow transitioned from subsonic to supersonic. Image taken from [Castan and Menou, 2011].

physical principles for this project. There are a number of second order factors which can be considered and may have an effect on the structure and dynamics of these atmospheres. Many of these second order effects were examined and not included if their magnitude was not significant enough to affect the atmosphere or if their parameter space was too poorly constrained to apply. There were a few effects considered due to their relevance to the resurfacing question - namely a model of stellar insolation which attempted to incorporate the angular size of the host star and the inclusion of sub stellar magma oceans.

### 2.2.1 Assumptions

A number of important assumptions underpin and enable the atmospheric and resurfacing model that is the main driver of this project. These assumptions allow for the study of the

dynamics and structure of these atmospheres in a relatively simple mathematical form and also help distinguish the relevance of certain secondary effects. There are five assumptions that are essential to the current formulation of the model - they are tested and hold in each case the model is applied to (CoRot-7b is used as an illustrative example for these tests).

The first is the necessity of conservation for critical parameters such as mass, momentum and energy. As will be described in the next section, these are the basis of the atmosphere model. In addition to the conservation of those variables however, there is also an additional requirement of the conservation of particle flux during resurfacing processes. As stated in the literature [Miguel et al., 2011, Castan and Menou, 2011], escape mechanisms for the likely dominant atmospheric constituents on these heated planets (Na, $O_2$, O, SiO, Fe, and Mg] are too slow to significantly alter resurfacing particle flux conservation. This additional conservation requirement is critical for the deposition estimates past the sonic point in these atmospheres and will be described in section 2.2.6.

The second assumption is that the surface temperature of these planets - the temperature which controls melting and vaporization processes - can be obtained using simple radiative balance estimates. Radiative fluxes dominate for these thin atmospheres, and latent heat fluxes are small compared to them. We compare latent heat fluxes to these radiative fluxes for all our different cases and find that this principle holds. For example, for CoRot-7b, the maximum latent heat contribution that occurs at the sub stellar point is almost three orders of magnitude smaller than the radiative contribution.

The third assumption is that atmosphere behaves as a continuous fluid and is hydrostatically bound to the planet. There are three main tests to ensure that this condition holds. The first is that the mean free path of the particles must be smaller than the local pressure scale height - a necessary condition for the continuous fluid assumption. This holds along the bulk of the flow in these planets' atmospheres and the model is stopped when the condition starts to breakdown (where the mean free path begins to exceed 10% of the local scale height) . In the case of CoRot-7b, this occurs at $\sim$93 degrees from the substellar point in our model. The second condition is that the local scale height must be small compared

to the radius of the planet. This is trivially true for most of the planets we test and in the case of CoRot-7b the ratio is nearly 1/200000 at the sub stellar point where the scale height is largest. Finally, the last condition is that the kinetic energy of the atmospheric flow must be less than the binding energy of the planet. This is again trivially true for all the cases tested and in the case of CoRot-7b is even more well held than the scale height to planetary radius ratio.

The fourth assumption is that the flow can be treated as turbulent and consequently that parameters such as the horizontal velocity and entropy per unit mass can be treated as constant with respect to the vertical axis. The most important exception to this adiabatic and constant horizontal velocity condition is the thin surface boundary layer - which is where the surface and atmosphere exchange fluxes of mass, horizontal momentum and energy. We test this by producing the average Reynolds Number for the flow region - in all of our cases, including CoRot-7b, we find the flow to be turbulent.

Finally, the last assumption we use for our model is that the planets we examine are tidally locked to their host star and that rotation effects are small enough to be ignored to first order. There is some debate over the likelihood that close-in planets with non-negligible eccentricity can fall into pseudosynchronous rotation [Makarov and Efroimsky, 2013] and it is suggested that many close-in solid planets are actually in higher order resonance states. However, given the different pathways to synchronous rotation [Makarov and Efroimsky, 2014] and short classical tidal locking timescales for such planets we continue to assume these planets are in a synchronous rotation state. Additionally, some of the effects of resurfacing are specifically being examined in order to determine potential perturbations to and the stability of synchronous rotation. With respect to the effect of rotation on atmospheric dynamics - that is tested by calculating the average Rossby number over the portion of the atmosphere where the fluidity condition holds. This test has indicated that to first order, rotation effects can be ignored for the class of planets that are being examined. For CoRot-7b, we find the average Rossby number to be close to 1. However, while rotation effects are consequently excluded in the development and implementation of our model, we do discuss

some potential ramifications of the role of rotation on our results in later sections.

### 2.2.2 Atmospheric Model

Our atmospheric model is nearly the same that was developed for Io in Ingersoll et al. [1985] and that was then applied to hot super-earths in Castan and Menou [2011] - it attempts to solve for the atmospheric pressure, temperature and velocity (at the base of the atmosphere) as a function of the angular distance $\theta$ away from the substellar point. This is done by solving the following conservation equations for mass, momentum and energy:

$$\frac{1}{rg\sin\theta}\frac{d}{d\theta}(VP\sin\theta) = mE \tag{2.1}$$

$$\frac{1}{rg\sin\theta}\frac{d}{d\theta}[(V^2+\beta C_pT)P\sin\theta] = \frac{1}{rg\tan\theta}\beta C_pTP + \tau \tag{2.2}$$

$$\frac{1}{rg\sin\theta}\frac{d}{d\theta}[(\frac{V^2}{2}+C_pT)VP\sin\theta] = Q \tag{2.3}$$

Details regarding the formulation of these equations are available in Ingersoll et al. [1985] but a general description of the above formulas is that the left side of these equations are the vertically integrated divergence of horizontal fluxes of mass, momentum and energy while the right side represents the mass, energy and momentum transport between the atmosphere and ground. The radius of the planet in meters is given by r and g is the surface gravity, which is simply $g = GM/r^2$ with M being the mass of the planet and G being the gravitational constant.

$\beta$ is a thermodynamic parameter given by $\beta = (R/(R+C_p))$ where $C_p$ is the specific heat at constant pressure and $R = k_b/m$. The values for the mass per atom, m, as well as $C_p$ are taken for the expected dominant constituent in the atmosphere (in most cases, including CoRot-7b, this is Sodium). The choice for this single constituent atmospheric model is based

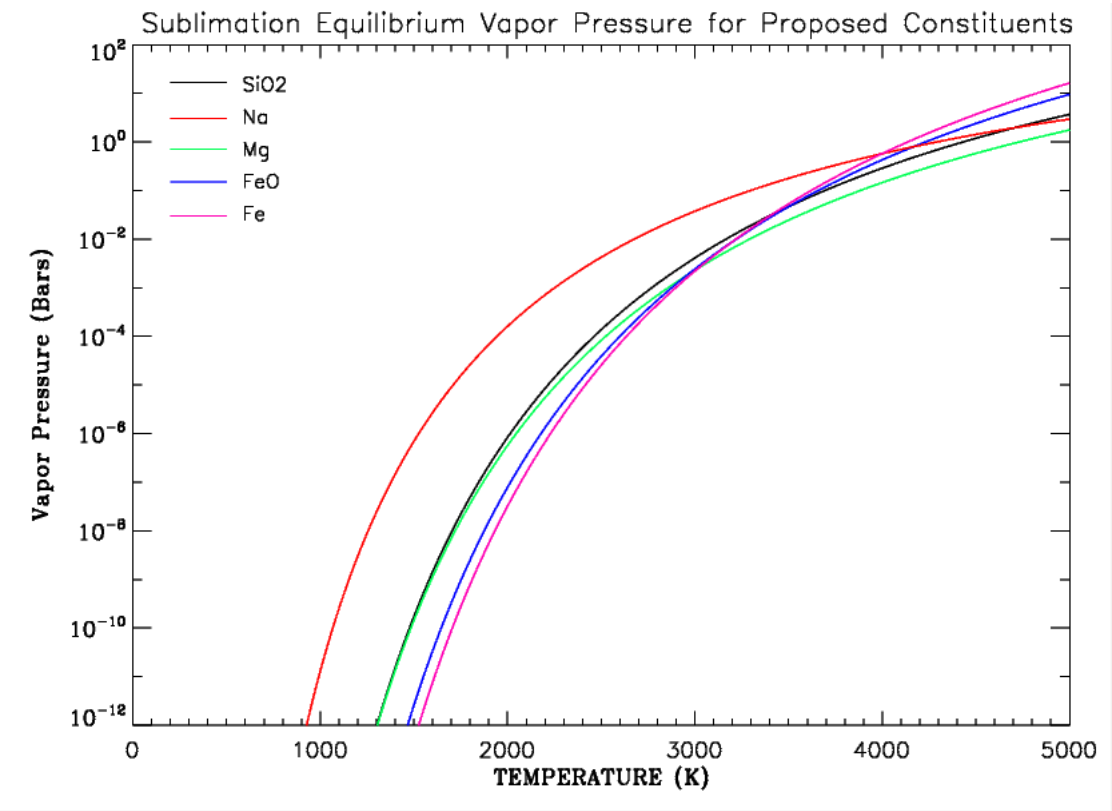


Figure 2.3: Fitted vaporization pressure curves as a function of temperature for a komatiite magma. Pressure curves were produced using Clausius-Clayperson equations for the individual constituents that were fitted from figure 2 of Miguel et al. [2011].

upon expected vaporization pressures for a komatiite magma given in figure 2 of Miguel et al. [2011]. Vaporization pressures as a function of temperature were fitted in order to produce Clausius Clapyeron relations given by $P_s(T_s) = Ae^{-B/T_s}$ for each of the dominant constituents and are plotted in figure 2.3. For equilibrium temperatures up to nearly 3500K, the vapor pressure of the dominant constituent is nearly an order of magnitude greater than the next most significant constituent. This justifies to first order our assumption of a single species atmosphere and these vapor pressure curves can be used to extract the constants used in our vapor pressure equations. Since Sodium was the dominant constituent for most models, we explicitly state any models where there was a different atmospheric constituent.

The quantities mE, $\tau$ and Q represent the mass, momentum and energy transport rate

per unit area between the atmosphere and the ground over the vertically small surface boundary layer. Specific prescriptions for the momentum and energy transport are based on the assumption that those transport rates are linearly dependent on the surface flux quantities being transported - which is reflected through the linear dependence of the equations on $\rho_s$. Equations for the particle, momentum and energy transport rate are given by:

$$E = \frac{(P_s - P)}{v_s\sqrt{2\pi}} \tag{2.4}$$

$$\tau = -\rho_s \omega_a V \tag{2.5}$$

$$Q = \rho_s \omega_s C_p T_s - \rho_s \omega_a (\frac{V^2}{2} + C_p T) \tag{2.6}$$

Here, the particle flux E is proportional to the difference between the surface vapor pressure $P_s$ and the atmospheric pressure P. The local speed of sound is $v_s$ which is given by $v_s = (kT_s/m)^{1/2}$. The surface boundary layer density $\rho_s$ is given by $\rho_s = (mP_s)/(k_b T_s)$. Momentum and energy transport rates are mediated by transfer coefficients $\omega_a$ and $\omega_s$. Since momentum and heat transfer in the surface boundary occur by both advection by a mean flow normal to the surface and by eddy driven turbulence, theses coefficients are parameterized in terms of two different velocities representing each process. The mean flow velocity $V_e$ is given by $V_e = mE/\rho_s$ while the eddy velocity $V_d$ is given by $V_d = V_*^2/V_0$ where $V_*^2$ is the frictional velocity. For the turbulent flow observed in our models the frictional velocity is solved for iteratively using the equation $V_{n+1} = 2.5 V_* log[(9.0 z V_* \rho)/\eta]$ (for laminar flow one would find $V_* = [2\eta V_0/\rho H]^{1/2}$). The transfer coefficients are then written in terms of simple functions of $V_e$ and $V_d$ that model the behavior of the transfer coefficients in known limits of $V_e >> V_d$ and $V_d >> V_e$ - the exact description of these formulations are given in Ingersoll et al. [1985]. The dynamic viscosity $\eta$ is given by Sutherland's formula:

$$\eta = \eta_0 (T_s/T_0)^{3/2} [(T_0 + C)/(T_s + C)] \tag{2.7}$$

with $\eta_0$ equal to $1.8X10^{-5}$ kg $m^{-1}s^{-1}$, $T_0 = 291K$ and C = 120K (it is important to note that Sutherland's formula is only valid to about 555K, but our simulations show that our results are not highly sensitive to variations in $\eta$).

Finally, in terms of solving for P, V and T at a new location as one advances from the substellar point, one must first calculate the right hand side of the main conservation equations (2.1 - 2.3) using previous values of P, V and T at $\theta$. Upon moving to the next value of $\theta$, those values should be augmented by the fluxes that are calculated for the terms in parenthesis on the left hand side. This will then yield the following system of equations where the fluxes are represented by the f values:

$$V_0 P = f_1 \tag{2.8}$$

$$(V_0^2 + \beta C_p T_) P_0 = f_2 \tag{2.9}$$

$$(V_0^2/2 + \beta C_p T_0) V_0 P_0 = f_3 \tag{2.10}$$

One can then solve for the velocity at the new value of $\theta$ using the following equation:

$$V_0 = \frac{f_2 \pm (f_2^2 - 2\beta(2-\beta) f_1 f_3)^{1/2}}{f_1 (2-\beta)} \tag{2.11}$$

with the Mach value given by $M = V_0 [(1-\beta)(\beta C_p T_0)]^{1/2}$. As the solution is advanced, these system of equations and the model developed here should yield a profile of P, V, T, E, $\tau$ and Q as function of $\theta$.

### 2.2.3 Surface Temperature and Magma Ocean Model

The surface temperature is critical to the atmospheric and magma ocean model as it determines evaporation, sublimation, deposition and melting processes. A surface temperature profile is determined using simple radiative balance for the dayside portion of a planet and a constant nightside temperature informed by potential geothermal heating contributions. We use a nightside temperature of 50K which is the value assumed for CoRoT-7b from geothermal heating in Léger et al. [2011]. The dayside temperature profile is obtained by taking the lambertian profile used in Castan and Menou [2011] of $T_s = [(T_{sub} - 50)\cos^{1/4}\theta] + 50$ (with a substellar temperature calculated for an albedo of 0) and extending it to the total illuminated portion of the dayside on these planets due to the angular size of the host star. This is done by using this temperature profile for $0 \leq \theta \leq 90$ and mapping that temperature profile to $0 \leq \theta \leq 90 + 0.5\theta_*$ where $\theta_*$ is the angular size of the star as seen from the substellar point of the planet and is given by $\theta_* = 2\arctan(R_*/a)$. Intuitively, this roughly takes into account the penumbra effect of illumination due to the angular size of the host star by treating the star as a continuum of point sources that consequently illuminate slightly shifted portions of the dayside. This is a first order approximation as it ignores the overlap of illumination between those adjacent points but still provides a very similar temperature model to those used in other relevant work [Castan and Menou, 2011, Léger et al., 2011]. We are currently developing and will incorporate a disk integrated model of the stellar surface in order to accurately produce the subtended solid angle as a function of $\theta$ on the planetary surface (similar to the work done in Léger et al. [2011]).

The extent of the substellar magma ocean is the other critical boundary of our study of resurfacing processes on these planets. Estimates of the total amount of mass advected to parts of a planet where cycling processes too slow to return the material are dependent on the angular extent of the magma ocean versus the spatial profile of evaporation and deposition by the atmosphere. We use two different estimates of ocean shore extent based on Léger et al. [2011] that correspond to different physical assumptions regarding the oceans. The first corresponds to the likely maximum angular extent of a substellar magma ocean

under the conditions that there is extremely efficient heat circulation in the ocean that results in a uniform ocean temperature and an ocean temperature choice that is the fusion temperature at zero pressure. This condition, along with a emissivity ratio of ∼1 for the ocean composition given in Léger et al. [2011] yields the following equation for ocean extent $\theta_{max}$:

$$\theta_{max} = \arccos([2(\frac{T_{ocean}}{T_*})^4(\frac{a}{R_*})^2] - 1) \tag{2.12}$$

where a is the orbital separation distance in meters, $R_*$ is the stellar radius in meters and $T_{ocean}$ and $T_*$ are the ocean and star temperature respectively. We use the same ocean composition as assumed in Léger et al. [2011] for this calculation - resulting in an ocean temperature of 2200K. Since this estimate will give us the maximum ocean extent based upon an idealized treatment of ocean temperature and circulation, we also use another method to calculate ocean extent. In this estimate, we use the point where the surface temperature equals the liquidus temperature of the local magma. For the composition assumed in Léger et al. [2011], the liquidus temperature is 2200K - the resulting estimate of the extent of the magma ocean is smaller than that of the previous method. The only case where we choose a different ocean composition is that of KOI1843.03, which has been speculated to be an Iron planet. In that case, we use an Iron composition for an atmosphere and an ocean temperature and liquidus temperature for Iron of 2800K. Calculations of the total evaporation and deposition over and beyond the magma ocean are calculated for both ocean extents in each of our models.

### 2.2.4 Numerical Implementation

The numerical technique we use in our model is the same shooting method described in Ingersoll et al. [1985]. The technique is implemented to solve for the atmosphere up until the sonic point. We rely on the same method of pressure guesses and checks with boundary conditions that is described in Ingersoll et al. [1985]. After guessing a pressure value at our

initial value of $\theta$, we accumulate fluxes obtained using an RK4 scheme and then solving for our system of equations. We continue shooting forward until boundary conditions necessitate a new guess and eventually find the difference between our pressure guesses converge to an arbitrarily small value. We then advance our model to an angular distance right before our solution diverges. Using this technique we iteratively continue shooting until we approach some arbitrarily small distance near the sonic point. Of note is that the implementation of our model does not begin right at the substellar point due to a singularity where our solution is undefined based on our value of $\theta$. Instead, we begin our solution at a very small distance away from the substellar point - significantly smaller than our grid spacing. We found the our solution for atmospheric variables and resurfacing estimates are insensitive to our choice of a starting point using this arbitrarily small substellar point displacement. This small displacement is reflected in all visualizations of our results and produces no significant change.

The use of this shooting method to constrain a transonic solution is critical given the singularity that exists at the sonic point. As a consequence, previous work as well as our study attempt to solve for an atmosphere to as close to the sonic point as possible and then extrapolate across and then past the sonic point. The solution past the sonic point is very sensitive to this extrapolation. In the case of our model, we find that a simple extrapolation through and past the sonic point is problematic in two ways. The first is that the term under the square root in equation 2.11 must remain positive (to have physical significance) as we move from the subcritical to supercritical branch for velocity. The second is that any extrapolation through and then past the sonic point must also ensure that the mass transferred between the surface and atmosphere (that is evaporated or sublimated and then deposited) must be conserved globally over the entire surface area of resurfacing. This conservation is critical especially given that there is no other mechanism for mass loss (such as escape).

As a result, we extrapolate through and past the sonic point using a Forward Difference Richardson Extrapolation that includes a factor which shoots to satisfy both of those two

requirements. In our case, we specifically shoot in order to conserve resurfacing mass by intuitively checking to make sure the total global mass lost over the extent of the fluid atmosphere is a very small percentage of the total global resurfacing mass. This is done by taking the resurfacing mass flux of the ring representing the surface area as a function of $\theta$ (given by $2\pi R_p \sin\theta$) where $\theta$ is again the angular distance from the substellar point and integrating over the extent of the resurfacing. We solve for the fluxes based upon our extrapolated atmospheric variables and check to make sure that our solutions lead to physically meaningful fluxes. We find that this holds true for all our cases with some rare and minimal exceptions. In a few cases, we find a small angular portion of the atmosphere has a very brief period centered on an inflection point around 0 for the term in the square root in equation 2.11 where that discriminant has trivially small negative values. The integrated total of these negative values is trivially small compared to the overall integrated value.

This slightly different approach to the extrapolation through and past the sonic point solves the mass conservation issue and also retains the smoothness requirement that the transonic solution must satisfy. The inclusion of an additional factor (which in all cases is very close to 1) when extrapolating through the supercritical branch is a relatively simple means of satisfying those two additional boundary conditions that does not require any additional assumptions regarding the nature of the atmosphere past the sonic point. However, while it does preserve transonic smoothness it does also change the shape of the supersonic solution slightly relative to a simple extrapolation. While the pressure, temperature, velocity and global resurfacing over one orbital period profiles are very close to each other in both extrapolation cases, there is a small difference between the two cases. This is evident in figure 2.4, which displays the difference in pressures and resurfacing between the two models for the atmosphere of Corot-7b - one with a conservative extrapolation and another with a non-conservative extrapolation. Compared to the overall pressure and resurfacing this is very small (much less than one percent) - however, we retain this check as an important boundary condition for the supercritical solution.

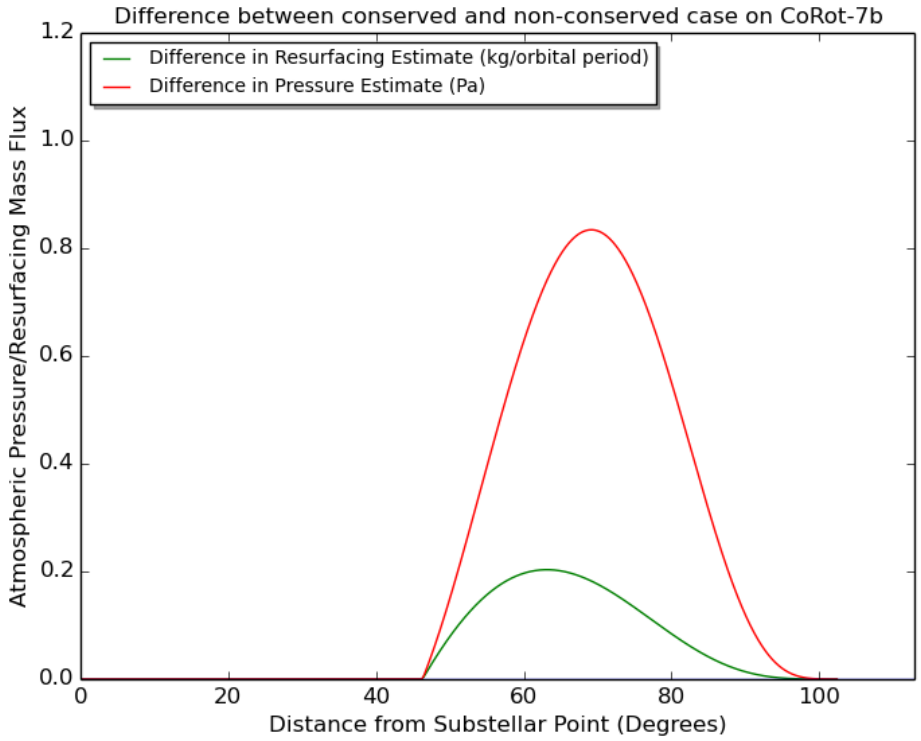


Figure 2.4: Difference in atmospheric pressure between models for the atmosphere of CoRot-7b with and without resurfaced mass conservation.

### 2.2.5 Planet and Parameter Selection

In order to model their potential resurfacing processes and also explore the atmospheric properties of close-in solid exoplanets, this project modeled the atmospheres and resurfacing for both a range of hypothetical planets across different parameter spaces and a selection of individual already discovered planets that cover every category of the Hot Super-Earth Atmosphere classification scheme given in Table 2.1.

In the case of the parameter space exploration, this entails modeling the atmospheres and resurfacing of 1 and 1.5 $R_e$ planets at distances where their substellar point temperature ranges from 2100K to 3300K in 400K increments. We choose masses for the planets based on the relation given by equation 2 in Weiss and Marcy [2014] for putative solid planets

without large gaseous envelopes. If the upper bound for the mass is under this value, we choose the maximum mass allowed. The distances and planets are chosen in order to examine general patterns that may emerge for atmospheric dynamics and resurfacing based upon orbital separation from host star (all of the substellar point temperatures correspond to orbital separations outside of the planet's fluid Roche limit around a G class star) and for different planet sizes. While we do also model individual planets, each of those planets are different enough from each other that extricating the effect of a particular parameter change is difficult. Additionally, the choice of these 4 temperatures ensures that these hypothetical planet span nearly all of the categories with the exception of the 'cold' one in Table 2.1. The dominant constituent for each atmosphere is chosen based upon Table 2.1 and is Sodium for each case except for the hottest planet - which has a SiO dominated atmosphere.

The individual planets we model include the three chosen by Castan and Menou, Corot 7b [Léger et al., 2009, Hatzes et al., 2011], Cnc 55 e [Winn et al., 2011] and Kepler 10b [Dumusque et al., 2014b] (despite the likelihood it is actually in a higher order resonance orbit), as well as Kepler 101c [Bonomo et al., 2014], Kepler 78b [Sanchis-Ojeda et al., 2013] and KOI 1843.03 [Rappaport et al., 2013]. All of these additional planets have constrained masses and radii that appear to preclude the likelihood of a large volatile envelope and as a group they span most of the different hot Super-Earth atmospheres listed in table 2.1. Appropriate planetary and system parameters are taken from the references cited next to each of the listed planets. Appropriate dominant constituents are chosen based upon substellar temperature (in every case except for KOI 1843.03 the dominant constituent is Sodium).

## 2.3 Results and Analysis

### 2.3.1 Replicating the Results of Castan and Menou [2011]

We validate our atmospheric model by first using it to replicate the results of Castan and Menou [2011] - who originally took the model created for Io and applied it to Heated Super-Earths. We use the temperature profile described in their model, their values for fits to the equation for vapor pressure of Sodium and stellar and planetary parameters described in their paper. We replicate their results for atmospheric models of CoRot 7b, Kepler 10b and 55 Cnc e without magnetic drag or ohmic dissipation. We choose to replicate atmospheres without these processes because of the large phase space for the parameterization for such effects. This uncertainty in the effect of these magnetic processes is what prevented us for

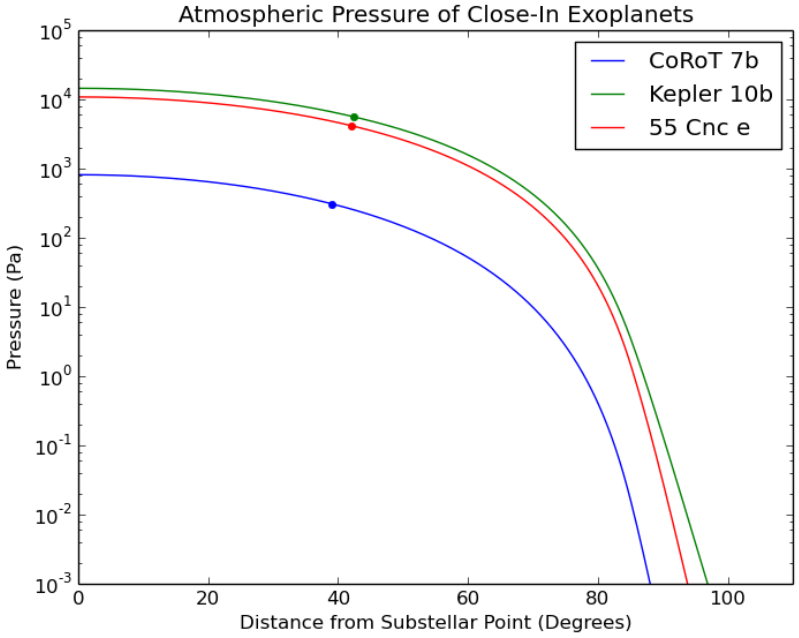


Figure 2.5: Replicated results of Castan and Menou [2011] for the atmospheric pressure profile of CoRot-7b, Kepler-10b and 55Cnc-e. Only results for model atmospheres without ohmic dissipation or magnetic drag are shown as we do not incorporate those processes into future work.

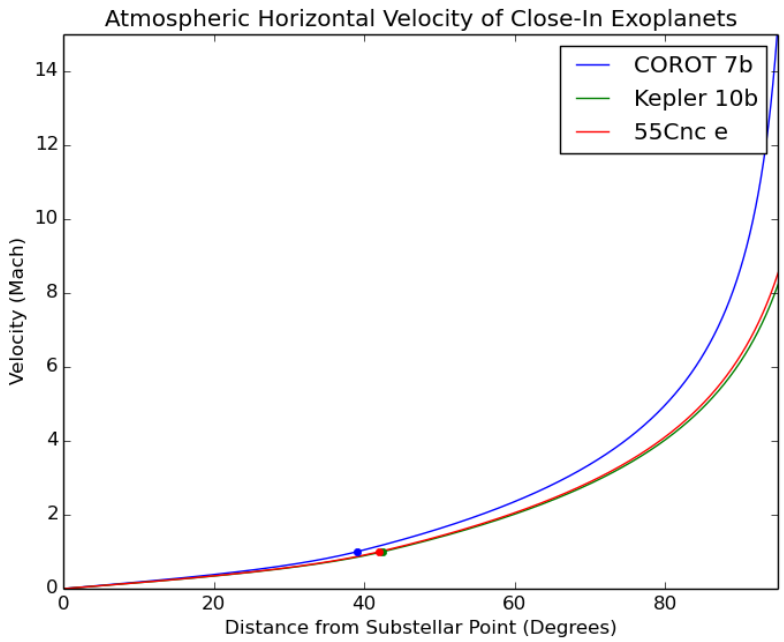


Figure 2.6: Replicated results of Castan and Menou [2011] for the atmospheric horizontal velocity profile of CoRot-7b, Kepler-10b and 55Cnc-e. Only results for model atmospheres without ohmic dissipation or magnetic drag are shown as we do not incorporate those processes into future work.

incorporating them in the rest of our work given that we are attempting to limit the number of additional effects to our model that are not very strongly constrained.

As is evident from a comparison of figure 2.5 with figure 2.1, our replicated pressure profiles and the individual sonic points agree very well with their work. Further, our results for the horizontal velocity profiles on these planets given in figure 2.6 also agree with their velocity profiles (see figure 2.2). Towards the portion of the flow where the fluid limit breaks down we see a slight divergence from their velocity values but this is likely due to sennsivity to the combination of the very thin atmosphere that has deposited most of its mass and the choice of different extrapolation methods. In any event, these portions of the atmosphere carry too little mass to impact any of our future findings.

As will be evident in the other subsections in our results, our models for these planets diverge slightly when we incorporate some of the additions we have described in the methodology section. While these results are somewhat different from the work of Castan and Menou [2011], they are generally still fairly similar with respect to the pressure, temperature and horizontal profiles as well as the location of the sonic points that they produce for planets that are examined in both studies

### 2.3.2 Phase Space Exploration

Since, already discovered close-in planets possess a diverse range of host star, orbital and bulk parameters, the exploration of a number of hypothetical planets with single variable changes should elucidate general tendencies for these planet's atmospheres and resurfacing based on our model. Varying the planetary radii (and consequently the mass and local gravity) and varying the substellar point temperature (equivalent to varying the orbital distance of the planet from it's host star) appear to have the following results:

- Pressure

  Atmospheric pressure varies (figure 2.7) in an intuitive way in response to a variation in the substellar temperature of the different planets (which is equivalent to variation in the orbital distance of the planets from their host star). As the hypothetical planets' substellar temperature gets higher (the planets get closer to their host star), there is more energy to drive vaporization and sublimation and atmospheric pressures go up and generally remain higher throughout the entire extent of the atmospheres. The one exception is the hottest planets - those above the 3168K limit where the dominant constituent is changed from Sodium to SiO. In that case while the atmosphere begins at a higher pressure, it eventually thins out and becomes less thick than the hottest Sodium atmospheres as it approaches the terminator.

  Variation in the size of the planet has minimal effect for the majority of the atmosphere. Until areas of net condensation/deposition, the larger planets do have a very

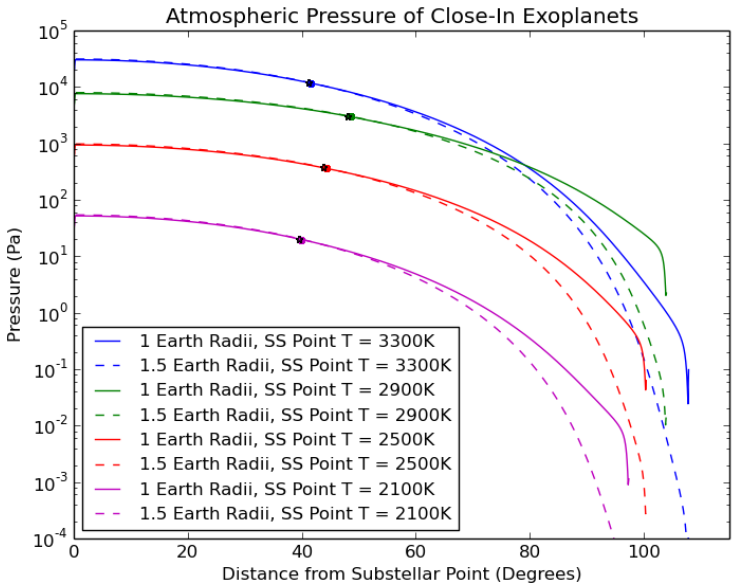


Figure 2.7: Atmospheric Pressure as a function of the angular distance away from the substellar point for a number of different hypothetical close-in solid exoplanets. The location of individual sonic points are marked with dots and stars.

slightly more dense atmosphere. However, the atmospheres for the larger planets condense more quickly when condensation/deposition begins and as a consequence past that point those planets actually possess thinner atmospheres than their smaller counterparts.

- Velocity and Mach Number

  The horizontal velocity of the atmospheres of modeled hypothetical planets are given in terms of kilometers per second in figure 2.8 and in terms of the local mach number in figure 2.9. Again, the hotter planets exhibit higher horizontal velocities in m/sec (the SiO atmosphere is responsible for the lower velocities for the hottest case). Unsurprisingly, horizontal velocities in m/sec are essentially the same for the smaller planets where the gravity constant is also lower than their larger counterparts. The difference is proportional to the ratios of bulk density between the larger and smaller

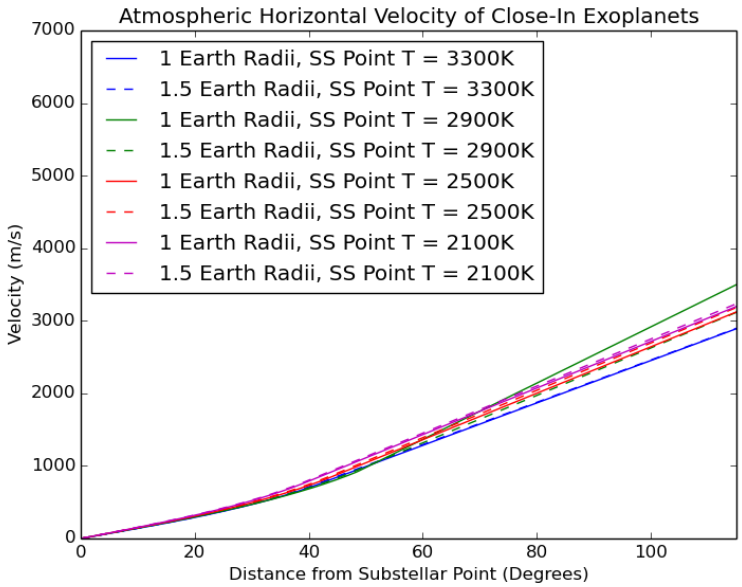


Figure 2.8: Atmospheric horizontal velocity in meters per second as a function of the angular distance away from the substellar point for a number of different hypothetical close-in solid exoplanets.

planets - a number that exceeds one due to the greater compressibility of the larger planets. Given the definition for the local mach number, however, it is then also not surprising to note that the sonic point on the smaller planets is located at a slightly greater distance away from the substellar point versus their larger counterparts. The mach number is very similar for larger and smaller planets in all four cases until the sonic point. However, after the sonic point and closer towards the main area of condensation/deposition, the mach values diverge as the larger planets return more of their mass to the surface. The most prominent example of this is the planet which has the highest substellar temperature while still possessing a Sodium atmosphere - the high thermal inertia of the atmosphere as mass is deposited leads to a larger divergence in mach number between the small and large planet case.

- Atmospheric Temperature

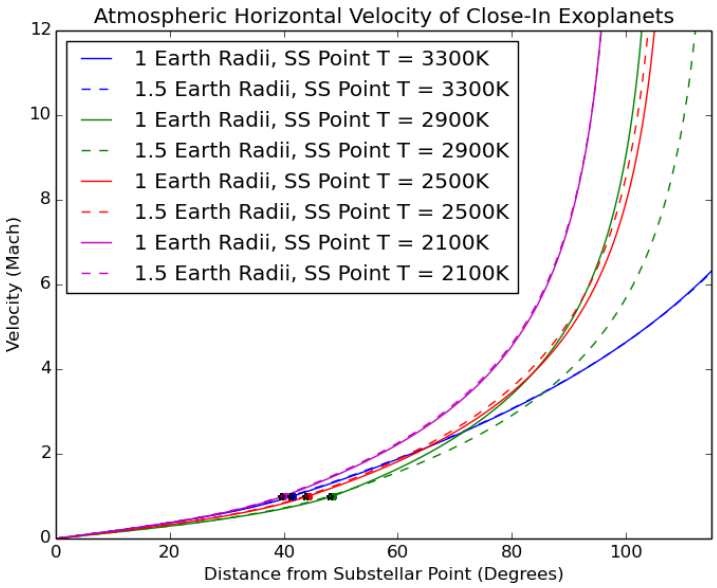


Figure 2.9: Atmospheric Horizontal Velocity in terms of Mach Number as a function of the angular distance away from the substellar point for a number of different hypothetical close-in solid exoplanets. The location of individual sonic points are marked with dots and stars.

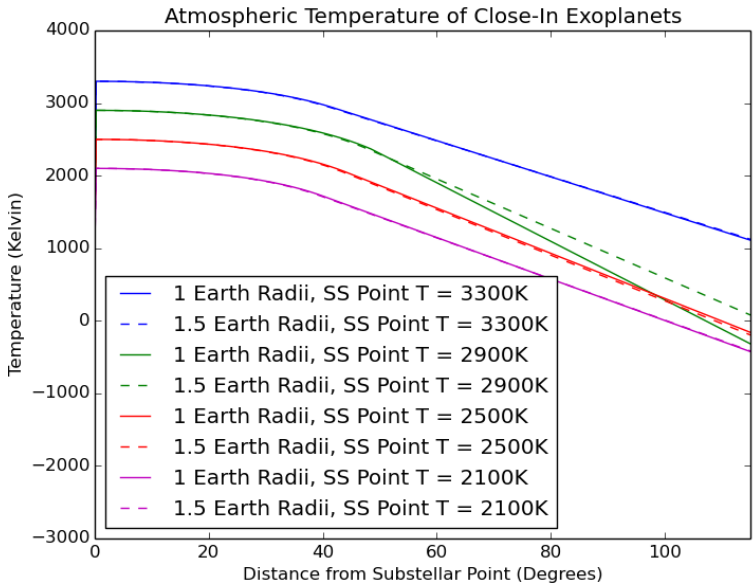


Figure 2.10: Atmospheric Temperature as a function of the angular distance away from the substellar point for a number of different hypothetical close-in solid exoplanets.

Atmospheric temperature exhibits a direct relationship to the distance of the planet from it's host star. As a consequence, all other factors being equal, those planets that are closer in and have high substellar temperatures also exhibited the highest overall atmospheric temperatures. Size of the planet has little discernible effect except for the cases of the hottest Sodium atmosphere. In that case, the retention of relatively more mass from the surface during condensation/deposition for the smaller 1.0 $R_e$ planet leads to a higher pressure but lower atmospheric temperature in the corresponding region. This is true for all pairs of planets to a small extent but is greatly exacerbated for the hottest Sodium atmosphere planet.

- Resurfacing Rates and Timescales

  Resurfacing rates per orbital period integrated over latitude as a function of the angular distance away from the substellar point are given in figure 2.11. Resurfacing rates range from 0 to nearly $4 * 10E10$ kg/orbital period over each individual

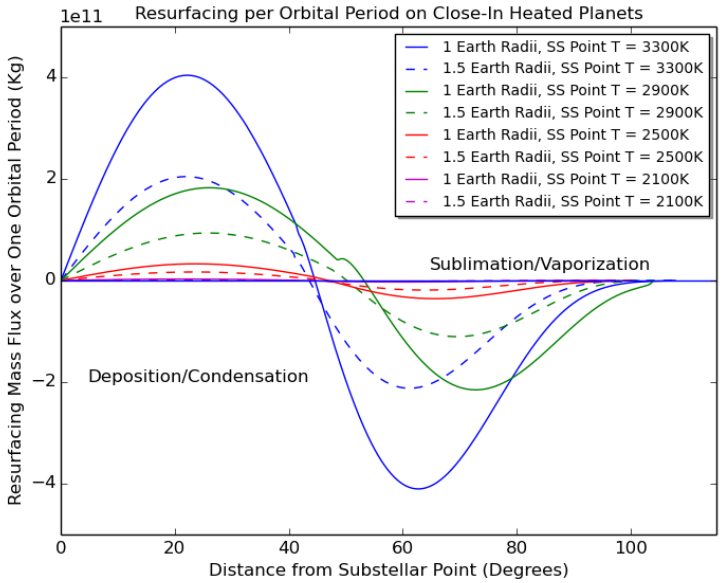


Figure 2.11: Resurfacing rate per orbital period integrated over latitude as a function of the angular distance away from the substellar point for a number of different hypothetical close-in solid exoplanets.

ring corresponding to an angle away from the substellar point. Maximum sublimation/vaporization occurs in a region centered around 25 degrees while maximum deposition/condensation occurs in a region generally around 60 degrees (though this varies slightly based upon temperature and atmospheric composition). The hottest planets tend to have the greatest amount of resurfacing and the smaller planets also exhibit greater resurfacing due to their smaller gravities. The slight numerical instability due to the mass conservation during extrapolation is evident in the resurfacing rate of the hottest sodium atmosphere planet but does not effect overall results.

Finally, the time required to advect a given percentage of total planetary mass beyond a magma ocean shoreline is calculated for an ocean shore extent that corresponds to the liquidus temperature for the magma (figure 2.12) and for the maximum ocean shore extent possible (figure 2.13). The total mass deposited per second past the

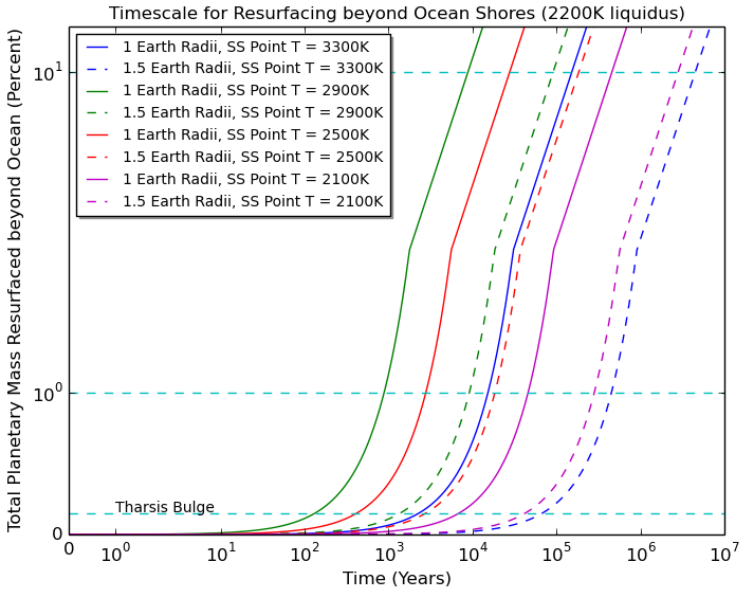


Figure 2.12: The time required to advect a given percentage of total planetary mass beyond a putative liquidus temperature based shoreline of a magma ocean. The mass deposited beyond the ocean shore is treated as having been removed permanently from the magma ocean as cycling processes are assumed to be very slow in that region of the planet.

ocean shore extent was over the region of deposition and then used to determine how long it would take to remove different percentages of the total mass of the planet. The extent of mass advection and deposition past the liquidus temperature shoreline is immense.

In every case, more than 1 percent of the total planetary mass is advected beyond the shoreline in less than 1 million years. In every case, more than 15 percent of the planet's mass would be advected beyond the shoreline within 10 million years. These cases are obviously dependent on the planetary and substellar reservoir for the dominant atmospheric constituent but they certainly indicate that such resurfacing processes can move enough mass on a planet that it's moment of inertia and consequently rotation may change. Illustrative of that point is the short timescales over

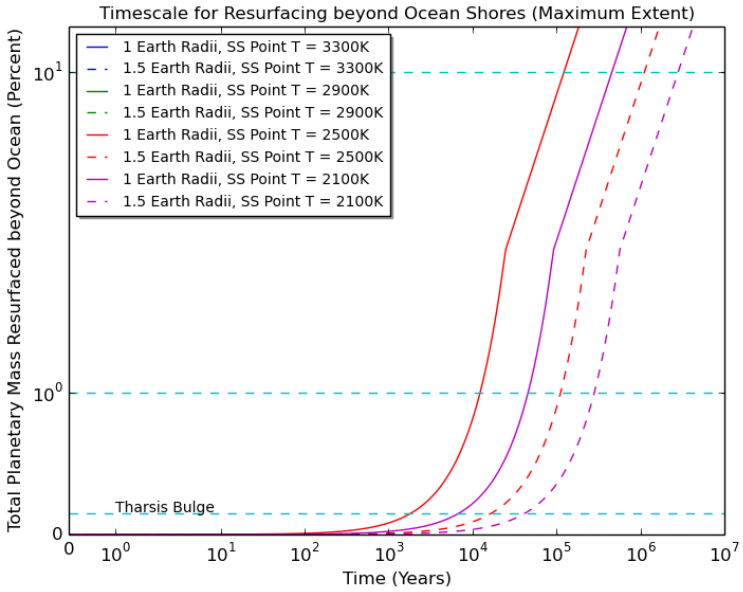


Figure 2.13: The time required to advect a given percentage of total planetary mass beyond a putative maximum angular extent shoreline of a magma ocean. The mass deposited beyond the ocean shore is treated as having been removed permanently from the magma ocean as cycling processes are assumed to be very slow in that region of the planet.

which each of the hypothetical planets would advect an amount of mass equivalent to a proportional Martian Tharsis Bulge on their planet. The Tharsis Bulge is a volcanic plateau on Mars so large and massive that it has affected the planet's moment of inertia and is believed to have caused changes in the planet's rotation [Nimmo and Tanaka, 2005] such as true polar wander.

With respect to general trends, the greater resurfacing on smaller planets leads to shorter times required to advect a particular amount of mass. Similarly, closer-in planets with higher substellar temperatures also advect mass more quickly. The planet with a SiO atmosphere takes longer to advect a given amount of mass that would otherwise be expected for it's temperature given Sodium as the dominant atmospheric constituent. Even in the case where the maximum ocean extent is assumed (in 4 cases

the ocean extent exceed the fluid limit and no mass is advected beyond the shore), the 4 coolest planet cases still exhibit massive advection to the point where it may affect the planet's rotation.

### 2.3.3 Individual Discovered Exoplanets

Table 2.2: Advection Timescale for Deposition Past Magma Ocean Shore

| AdvectionTimescale | | | |
|---|---|---|---|
| Planet Name | Planetary Radius ($R_e$) | Time to Deposit a 'Tharsis Bulge' Past Ocean Shore (yrs) [2] | Time to Deposit 10% of Planetary Mass Past Ocean Shore (yrs)[2] |
| Corot 7b | 1.58 | 6600 | 425000 |
| Kepler 10b | 1.47 | 550 | 35000 |
| 55 Cnc e | 2.00 | 1800 | 116000 |
| Kepler 78b | 1.12 | 250 | 16000 |
| Kepler 101c | 1.25 | 127000 | 8200000 |
| KOI 1843.03[1] | 0.6 | 12600 | 810000 |

[1] Assuming an Iron Planet
[2] We assume a magma ocean shore that begins where the surface temperature is equal to the liquidus temperature of ocean composition.

In addition to our planetary parameter phase space exploration, we also ran our model for a number of different discovered close-in solid exoplanets. While the general features of varying specific planetary, orbital and stellar parameters discussed in the previous section can give a general sense of dynamics and resurfacing processes on these planets the specific values are particularly interesting because they can be used to inform observations. A basic

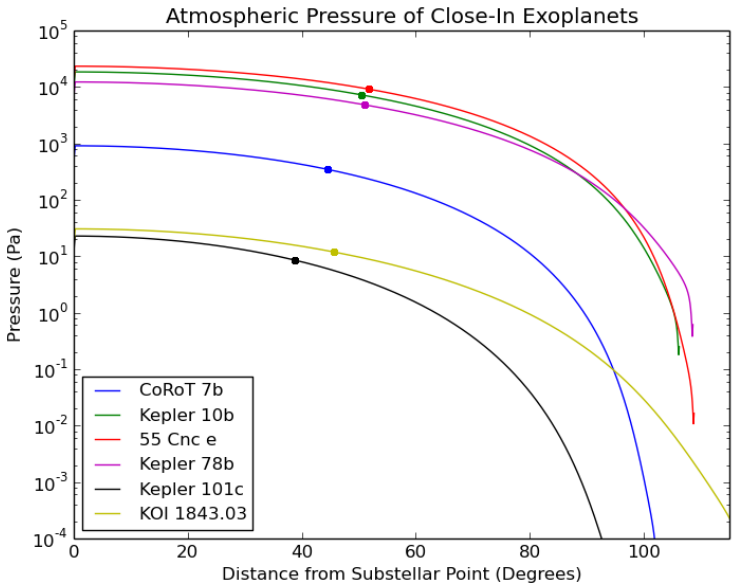


Figure 2.14: Atmospheric Pressure as a function of the angular distance away from the substellar point for a number of discovered close-in solid exoplanets. The location of individual sonic points are marked with dots.

summary of the main purpose of this study - to determine whether such planets experience such severe atmospheric resurfacing as to potentially change their rotation - is given in table 2.2. In that table the examined planets are listed along with timescales that correspond to the amount of time it would take that planet's atmosphere to move an amount of mass past it's magma ocean shore that would be equivalent to a proportional 'Tharsis Bulge' and to 10% of the total mass of the planet. Figures that summarize the atmospheric pressure profile (figure 2.14), the atmospheric horizontal velocity in m/s (figure 2.15) and mach (figure 2.16), and the atmospheric temperature (figure 2.17) are given.

Additionally, figures are also produced that display the resurfacing rate per orbital period integrated over latitude as a function of the angular distance away from the substellar point for all planets (figure 2.18) and for planets whose resurfacing rates in such cases are so much smaller that they benefit from rescaling (figure 2.19). Finally, timescale figures are

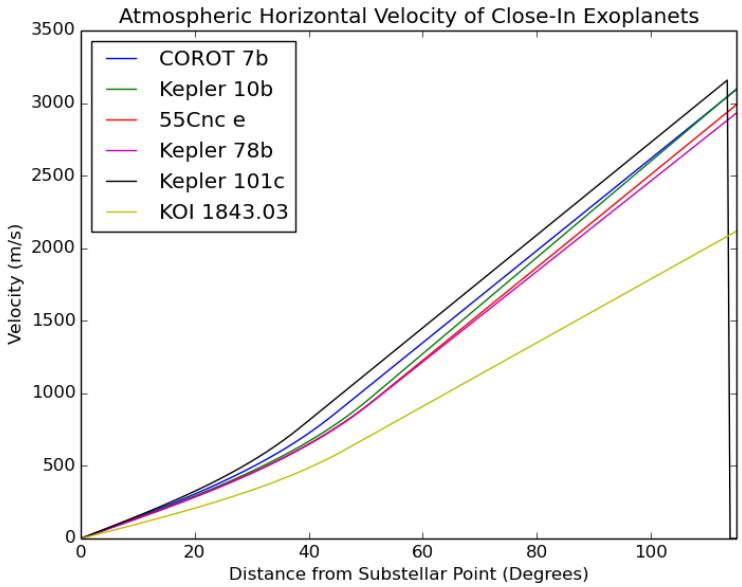


Figure 2.15: Atmospheric horizontal velocity in meters per second as a function of the angular distance away from the substellar point for a number of different discovered close-in solid exoplanets.

produced that show how long it would take for the individual planets to advect different percentages of the total planetary mass for both the case of the liquidus ocean shore (figure 2.20) and for the maximum ocean shore extent (figure 2.21).

Along with visualizations of the atmospheres and resurfacing occurring on these planets, the following is a short description of the atmospheric dynamics and resurfacing processes on each planet:

- Corot 7b

  Corot 7b has a thin atmosphere whose pressure is nearly $10^3$ pascals at it's substellar point. It's dynamics are marked by a sonic point near 44 degrees and regions of maximum evaporation/sublimation and condensation/deposition that roughly correspond to 25 and 65 degrees from the substellar point. Neither the estimate for the maximum or liquidus magma ocean shore extent result in a magma ocean that extends over 50%

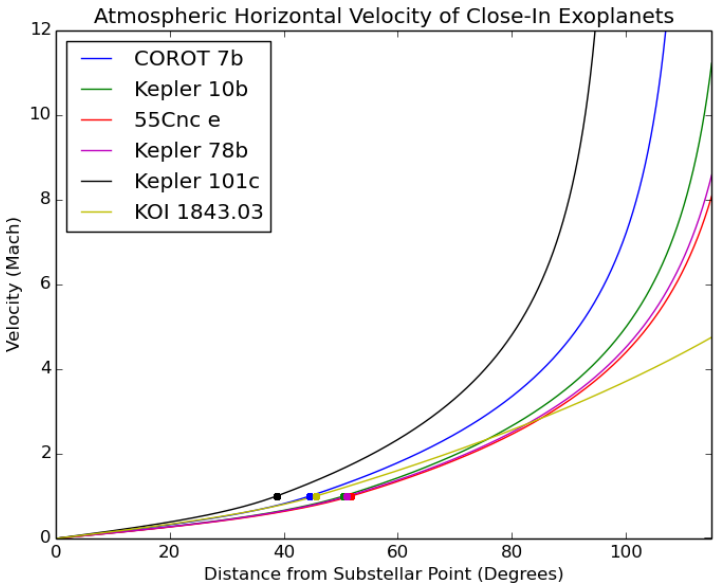


Figure 2.16: Atmospheric Horizontal Velocity in terms of Mach Number as a function of the angular distance away from the substellar point for a number of different discovered close-in solid exoplanets. The location of individual sonic points are marked with dots.

of the planet. Timescales for advection of 15% of the total planet mass past the ocean shore extent (given a large reservoir of it's main atmospheric constituent) are under 5 million years in both cases.

- Kepler 10b

  Kepler 10b has a thin atmosphere whose pressure is a little more than $10^4$ pascals at it's substellar point. It's dynamics are marked by a sonic point near 48 degrees and regions of maximum evaporation/sublimation and condensation/deposition that roughly correspond to 27 and 72 degrees from the substellar point. The estimate for the maximum magma ocean shore extent results in a magma ocean that extends over 50% of the planet. The liquidus ocean shore extent model does not result in a magma ocean that extends over 50% of the planet. The Timescale for advection of 15% of the total planet mass past the ocean shore extent (given a large reservoir of it's main

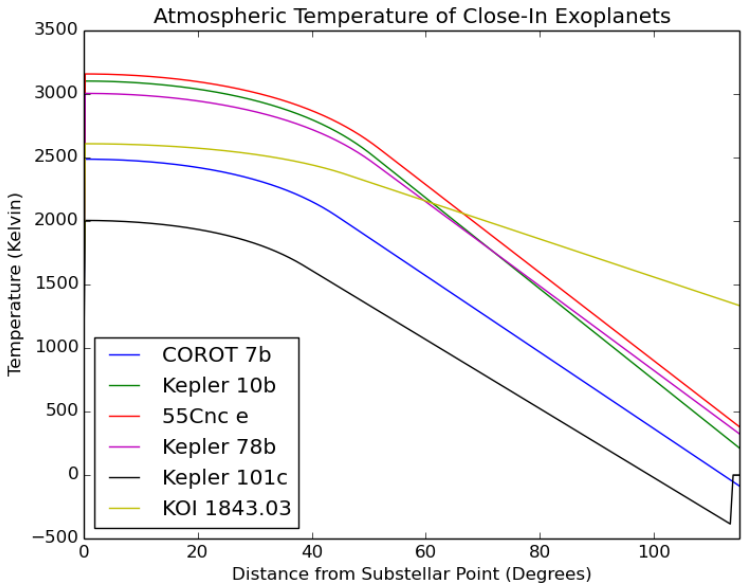


Figure 2.17: Atmospheric Temperature as a function of the angular distance away from the substellar point for a number of different discovered close-in solid exoplanets.

atmospheric constituent) is under 75,000 years in the liquidus ocean shore case while the maximum ocean extent case has no mass that is advected beyond the ocean shore.

- 55 Cnc e

  55 Cnc e has a moderately thin atmosphere whose pressure is a several factors greater than $10^4$ pascals at it's substellar point. It's dynamics are marked by a sonic point near 51 degrees and regions of maximum evaporation/sublimation and condensation/deposition that roughly correspond to 27 and 75 degrees from the substellar point. The estimate for the maximum magma ocean shore extent results in a magma ocean that extends over 50% of the planet. The liquidus ocean shore extent model does not result in a magma ocean that extends over 50% of the planet. The Timescale for advection of 15% of the total planet mass past the ocean shore extent (given a large reservoir of it's main atmospheric constituent) is under 250,000 years in the liquidus ocean shore case while the maximum ocean extent case has no mass that is advected

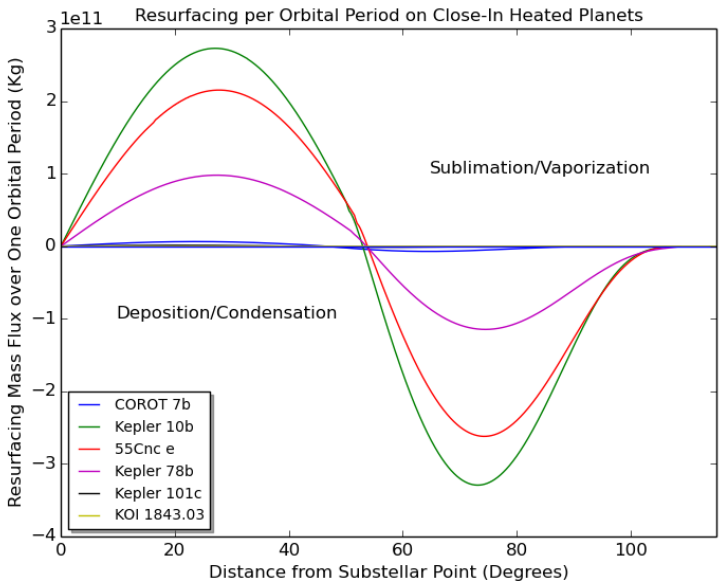


Figure 2.18: Resurfacing rate per orbital period integrated over latitude as a function of the angular distance away from the substellar point for a number of different discovered close-in solid exoplanets.

beyond the ocean shore.

- Kepler 78b

  Kepler 78b has a thin atmosphere whose pressure is a little greater than $10^4$ pascals at it's substellar point. It's dynamics are marked by a sonic point near 50 degrees and regions of maximum evaporation/sublimation and condensation/deposition that roughly correspond to 27 and 75 degrees from the substellar point. The estimate for the maximum magma ocean shore extent results in a magma ocean that extends over 50% of the planet. The liquidus ocean shore extent model does not result in a magma ocean that extends over 50% of the planet. The Timescale for advection of 15% of the total planet mass past the ocean shore extent (given a large reservoir of it's main atmospheric constituent) is under 50,000 years in the liquidus ocean shore case while the maximum ocean extent case has no mass that is advected beyond the ocean shore.

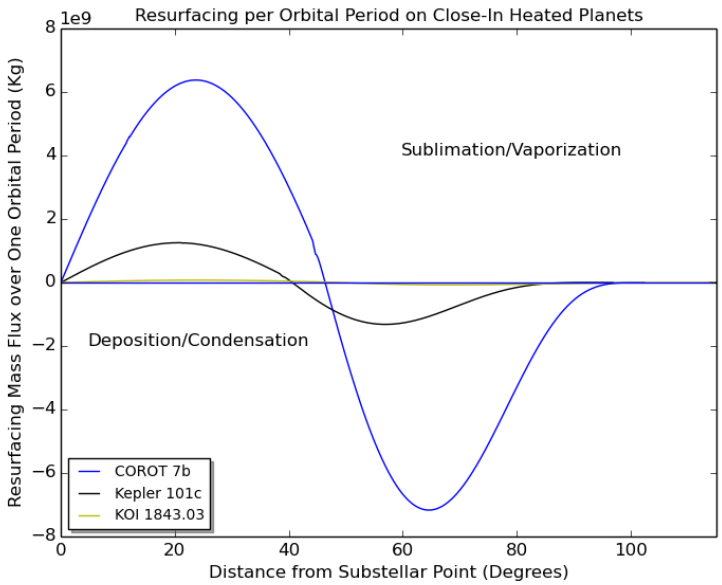


Figure 2.19: Resurfacing rate per orbital period integrated over latitude as a function of the angular distance away from the substellar point for a number of different discovered close-in solid exoplanets. These planets were included in the previous image but their resurfacing processes are more clearly seen on this different scale.

- Kepler 101c

  Kepler 101c has a very thin atmosphere whose pressure is a little more than 20 pascals at it's substellar point. It's dynamics are marked by a sonic point near 40 degrees and regions of maximum evaporation/sublimation and condensation/deposition that roughly correspond to 20 and 58 degrees from the substellar point. Neither the estimate for the maximum or liquidus magma ocean shore extent result in a magma ocean that extends over 50% of the planet. Timescales for advection of 15% of the total planet mass past the ocean shore extent (given a large reservoir of it's main atmospheric constituent) are under 20 million years in both cases.

- KOI 1843.03

  KOI 1843.03 is modeled as an Iron planet with an Iron atmosphere and magma ocean,

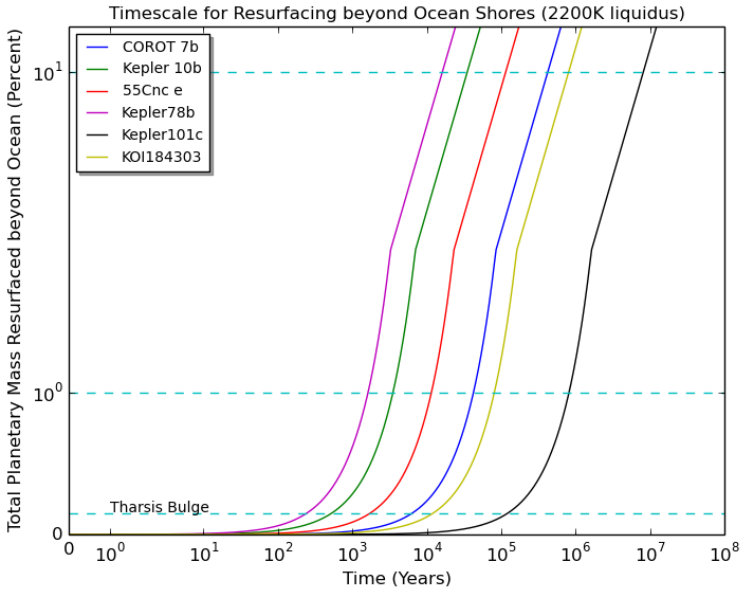


Figure 2.20: The time required to advect a given percentage of total planetary mass beyond a putative liquidus temperature based shoreline of a magma ocean. The mass deposited beyond the ocean shore is treated as having been removed permanently from the magma ocean as cycling processes are assumed to be very slow in that region of the planet.

which changes it's atmospheric dynamics and resurfacing from what would otherwise be expected for such a small and hot planet. It has a very thin atmosphere whose pressure is less than 50 pascals at it's substellar point. It's dynamics are marked by a sonic point near 45 degrees and regions of maximum evaporation/sublimation and condensation/deposition that roughly correspond to 20 and 70 degrees from the substellar point. Neither the estimate for the maximum or liquidus magma ocean shore extent result in a magma ocean that extends over 50% of the planet. Timescales for advection of 15% of the total planet mass past the ocean shore extent (given a large reservoir of it's main atmospheric constituent) are under 2 million years in both cases.

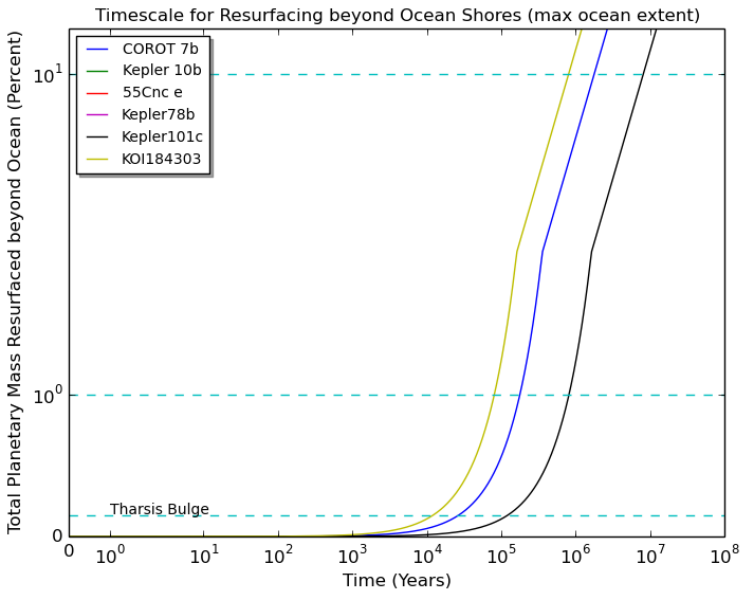


Figure 2.21: The time required to advect a given percentage of total planetary mass beyond a putative maximum angular extent shoreline of a magma ocean. The mass deposited beyond the ocean shore is treated as having been removed permanently from the magma ocean as cycling processes are assumed to be very slow in that region of the planet. Some of the planets do not appear on the graph because magma ocean extent is so large in this case that no mass is deposited beyond it.

### 2.3.4 Conclusion and Additional Effects

The results of our modeling of the atmospheric dynamics and resurfacing processes of close in solid planets indicates that atmospheric mass advection by these planets beyond their magma ocean shores is likely massive and quick enough to alter the moment of inertia of these planets. This in turn can affect the planet's rotation - this may be in the form of additional constant torque applied to the planet's rotation, librations or some other unique manifestation - additional work is needed to interpret the details. In addition, the localized deposition profiles on these planets beyond their magma ocean shore may suggest a potential interpretation of transit photometry phase curve features which indicate a spatial variability

in planetary albedo.

While these results are promising, it is also important to note the limits of such modeling. Some of the assumptions that underpin the model should be relaxed in order to gain a better understanding of atmospheric dynamics and resurfacing on these planets. In particular, planetary rotation should be included as it should break symmetries that may effect atmospheric structure and dynamics and resurfacing profiles. To this extent, such planets would also benefit from simple 3d models exploring their atmospheres. While less is known about parameters on these planets that are typically used to characterize such models, even 3d toy models of their atmosphere may provide a substantial advance in understanding. Other improvement can be made in a better understanding of how stellar activity might effect such atmospheres - whether though interactions with the solar wind or due to other transient phenomena. A critical improvement that would enable better resurfacing estimates and insight into potential cycling through atmospheric constituents would be incorporating multiple atmospheric constituents into a model that also includes their reservoirs. Finally, another interesting effect should be considered that is the subject of the other project in this thesis - the likely aspherical shape of these planets. This asphericity will change the apparent gravity as a function of the angle away from the substellar point and may also be an important factor in understanding the physical environment on these worlds.

# Chapter 3: The Observational Effects and Signatures of Tidally Distorted Solid Exoplanets

The other main project that constitutes this thesis grew out of a second order effect that was examined in the context of hot close-in solid planet atmospheres. Some of the planets studied in the previous project are likely tidally and rotationally distorted to a significant extent. This effect on atmospheric dyanamics and structure is currently relatively unexplored in literature and was consequently ignored for simplicity in the previous project due to ambinguity in potential effects. However, the relatively significant tidal bulges that were calculated for planets such as CoRot-7b in the previous project necessitated a study of what types of observational signatures their asphericity could produce. The following project examines these close-in solid planets' asphericity in order to ascertain potential observational signatures that may be produced that could both confound and enable characterization of these planets. Such signatures are then examined in the context of the census of exoplanets that is available currently and that will be available in the near future. This project was carried out in collaboration with Prof. Michael Summers and Alex Panka.

## 3.1 Introduction

The distortion of an astronomical object's spherical shape has long been known to provide insight to the interior structure, composition and evolution of a body. Research exploring shape has spanned over many different types of objects including gaseous bodies [Chandrasekhar, 1933, Lai et al., 1993] as well as solid, solar system bodies [Dermott, 1979]. Interest in the shape of an object as a proxy for other parameters has extended to the burgeoning field of exoplanets.

Theoretical and modeling work has already yielded a number of predictions and constraints on the ability to detect rotational and tidal deformation in gas giant exoplanets. Additionally, similar work has also explored the potential effects of such distortions on the ability to accurately describe an exoplanet system. Early estimates of a detectable variation in transit depth within a light curve due to oblateness yielded results which even for the most favorable scenarios were very close to observational limits [Seager and Hui, 2002, Barnes and Fortney, 2003]. On the other hand, the reflection effect for tidally distorted planets has been shown to be potentially significant in certain cases [Budaj, 2011]. In that study, Budaj demonstrated the significant light curve variations that arise for Roche Model approximated tidally distorted planets when the bond albedo of the planet is varied to simulate different levels of reflected starlight versus absorbed/re-radiated/redistributed light. Indeed, there have been observational results which have suggested potential detection of just such a deformation in the shape of a gas giant exoplanet. Ellipsoidal variations in transit depth of the light curve of WASP-12b [Cowan et al., 2012] have been roughly fitted and suggest a near 3:2 ratio between the planets longest and shortest axes.

In addition to these variations, a number of studies concluded that the gravitational quadrupole field which would arise from tidal and rotational bulges could induce apsidal precession that would manifest itself as predictable transit timing effects [Jordán and Bakos, 2008, Ragozzine and Wolf, 2009, Kane et al., 2012]. In addition to apsidal precession, exoplanet oblateness and obliquity would also induce spin precession that under certain conditions could yield detectable signals for certain gas giants [Carter and Winn, 2010b]. Observational results have been used to constrain the oblateness of HD189733b through non-detections of transit depth changes due to such precession and by non-detection of potential transit timing variations [Carter and Winn, 2010a].

An important effect of potential distortions to the shape of an exoplanet is the potential for particular orbital orientations to bias the volume measurement of a planet and subsequently other derived parameters. For planets in a synchronous orbit that are close in to the host star the projected area of the ellipsoidal shape of the planet caused by rotational

and tidal effects can result in an underestimate of the radius of the planet [Leconte et al., 2011]. In some cases these distortions may result in biases of 10% or higher in the light curves and radius measurements of these planets [Li et al., 2010]. Parameters which are subsequently derived from these radius estimates such as density and size of the solid inner cores of gas giants can then also be estimated incorrectly [Burton et al., 2014]. While such an effect has been explored for gas giants, one of the main topics of this study is to look at whether this bias may also exist for solid exoplanets with distorted shapes. In addition this project also examines the assumption that the effects of an aspherical solid exoplanet in its transit photometry are too small to be observationally significant. In particular, it attempts to quantify the variation in the projected area of a solid planet within its light curve.

Solid exoplanets constitute a significant portion and increasing portion of the current census of planets outside our solar system. Characterization of a planet as a likely solid planet is obtained using bulk properties of a planet such as density from observed constraints on radius and mass [Valencia et al., 2007b]. While degeneracy over interior models still remain, such a parameterization can to first order divide a planet between a gaseous or solid planet. Estimates of occurrence rates for planets vary significantly based on the spectral class of the host star and the orbital separation of the planet from the star [Dressing and Charbonneau, 2013, Mulders et al., 2015]. However, bound planets have been detected at distances from almost right at the Roche limit for their host star [Hellier et al., 2011, Gillon et al., 2014, Rappaport et al., 2013] to much farther out from their host star than any planet in our solar system. This substantial parameter space which we are faced with when trying explore the potential bias and observable signatures of distorted aspherical solid planets is resolved by the fact that previous work examining shape distortions on gas giant planets have required certain orbital and observational constraints which also neatly align with the bias of transit photometry to detect close-in exoplanets.

In the next section, there is an examination of observational bias effects in the measured radius of solid exoplanets due to planetary asphericity. The theory and assumptions made

regarding the orbits, rotation and shape distortions of these planets is addressed. Results are then produced which quantify observational bias and subsequent bias in estimated planetary parameters for a range of different sized exoplanets around different spectral classes. In the following section the project addresses the possibility and magnitude of any in-transit signal that can be detected due to these distortions to planetary shape and discusses the potential for ellipsoidal variations. Finally, in section 4 I comment on the results of the estimates and discuss implications and potential future of areas of study.

## 3.2 Measuring Observational Bias in Radius Estimates

### 3.2.1 Tidal and Rotational Deformation Theory and Assumptions

A rotating planet orbiting a star will be subject to both tidal and rotational forces which distort the shape of the planet. Since the gravitational potential due to the star varies inversely with distance, the resulting gradient across the discrete boundaries of the orbiting planet will induce a symmetric tidal bulge in the direction of the tide-inducing body that will deform the object into a prolate ellipsoid. The gravitational potential V felt by a point P on the surface of a planet due to some external body treated as a point mass such as the host star can be written as

$$V = -G\frac{m_s}{a}[1 + \frac{R_p}{a}\cos\psi + (\frac{R_p}{a})^2\frac{1}{2}(3\cos^2\psi - 1) + ...] \tag{3.1}$$

[Murray, C. D. and Dermott, S. F., 2000]

Where G is the gravitational constant, $m_s$ is the mass of the star, a is the orbital separation of the two objects, $R_p$ is the radius of the planet, and $\psi$ is an angle measured from the line joining the centers of the two bodies to the point on the surface.

The potential here is the result of binomial expansion of the distance from the perturbing body to the point on the surface, which assumes $R_p/a \ll 1$. This will be a generally well held assumption for nearly all the cases examined (for example a 2 Earth Radii planet orbiting

at the fluid Roche Limit of a M1 V star will have a $^{R_p}/_a$ approximately equal to that of the Earth-moon system). Even for the scenario with largest and closest orbiting planet around the smallest host star, the value of $^{R_p}/_a$ is $< 0.1$. The tide raising part of the potential is the $2^{nd}$ order term and can be written in terms of the Legendre polynomial of degree two given by:

$$P_2(\cos\psi) = \frac{1}{4}(3\cos 2\psi + 1) \tag{3.2}$$

In order for the surface of the planet to be on an equipotential the deformed shape of the planet can then be described by the same solid spherical harmonic of the second degree that describes the tide raising potential. Taking into account implied symmetry about the line joining the two bodies from the dependence on the angle $\psi$ one can then describe the deformed shape of an incompressible planet as

$$R_{cb}(\psi) = A[1 + S_2 P_2(\cos\psi)] \tag{3.3}$$

Where R is the distance of the surface from the center of the planet, A is the mean radius and $S_2$ is a constant which describes the ellipticity of the planets shape. Murray, C. D. and Dermott, S. F. [2000] also extend the treatment of the planet as a two layer incompressible body. They take into account additional forces acting at the boundary of the two layers including variational forces within the layers leading to loading terms as well as the internal potentials of each layer with their own separate densities. For our study we use a first order calculation of the deformed shape of the body as a one layer uniform body equivalent to the scenario described by Murray and Dermott of the deformation of the core boundary if the ocean were removed. Due to the degeneracy of potential interior structures of exoplanets when just given bulk values such as mass and volume we find it sufficient to characterize the shape deforming factors with as few variables as possible.

In the case of a planet modeled with a single uniform layer the equilibrium tide and consequently the ellipticity of the planet can be characterized by just the orbital separation

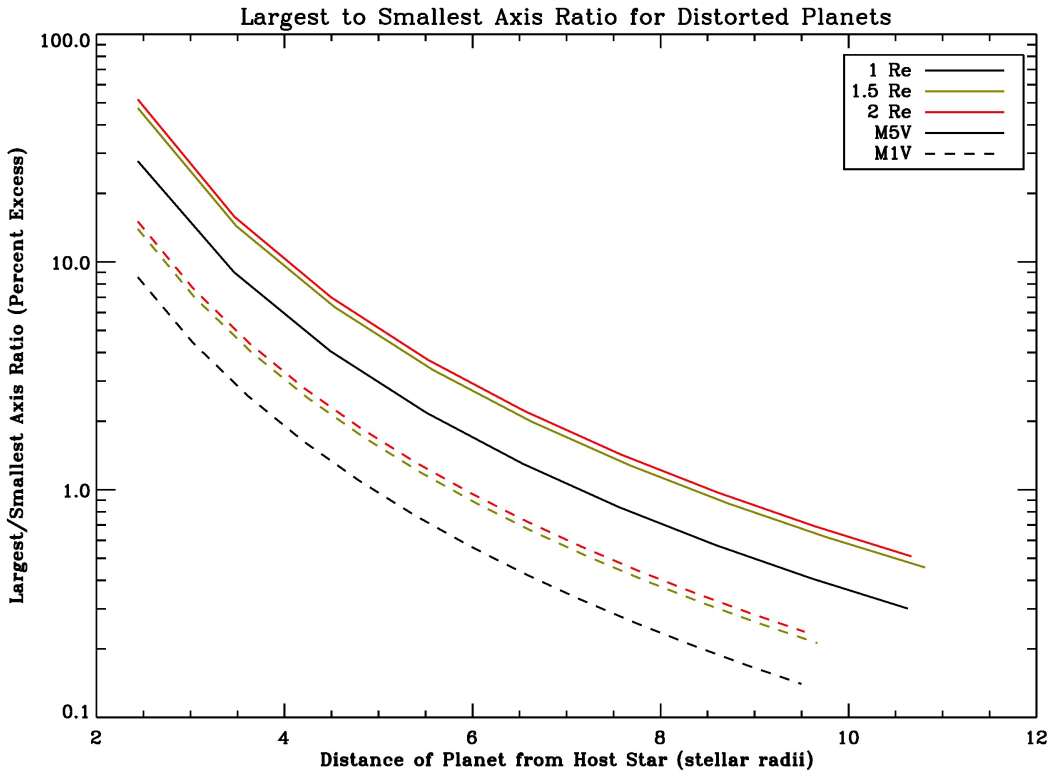


Figure 3.1: The ratio of the longest to smallest axis for triaxial ellipsoid planets of 1, 1.5 and 2 Earth Radii orbiting M5V and M1V stars. For 1.5 and 2 Earth Radii planets orbiting an M5V star the ratio can approach 3:2 near the fluid Roche limit. Around M1V stars a longest axis about 10% larger than the shortest axis is typical for all three planets near the fluid Roche limit.

of the bodies, bulk parameters of mass and mean radius and the effective rigidity of the planet. The amplitude of the equilibrium tide induced by the host star is just

$$AS_2 = \frac{(5/2)\zeta_c}{1+\tilde{\mu}} \tag{3.4}$$

where

$$\zeta = \frac{m_s}{m_p}(\frac{R_p}{a})^3 R_p \tag{3.5}$$

Where $m_p$ is the mass of the planet and the dimensionless variable $\tilde{\mu}$ is the effective rigidity, which relates the elastic strength of the planet to its gravity and which is given by:

$$\tilde{\mu} = \frac{19\mu}{2\rho g_c A} \tag{3.6}$$

where $\rho$ is just density of the planet, g is just the planets gravitational constant, and $\mu$ is the rigidity. We assume a value of $\mu$ of $\sim$ 100 GPa, about the mean value for the Earth [Fowler, 2005], for the planets we test. We choose this value in order to make as few assumptions about the compositional and structural nature of these planets given the current inability to observationally constrain those parameters (of course choosing an Earth-like rigidity value is an assumption in itself). Additionally, given that current hypotheses regarding the nature of these planets range from ostensibly rigid Iron-core Hot Jupiter remnants to planets which may significantly be less rigid due to partial or whole scale melting any assumed rigidity value would be somewhat arbitrary. We do however also test a slightly higher value of $\mu \sim$ 300 GPa, the predicted rigidity value of the Earth's core [Bullen, 1969, Goldreich and Peale, 1968], in order to test the effect of different rigidity values in terms of the change in bias of observed planetary parameters and whether direct observations of elliptical shape would be sensitive enough to constrain mean planetary rigidity values.

Once we have found the constants quantifying the tidal effect on planetary shape we can now use an additional assumptions of synchronous rotation of these planets in a near-equatorial (with zero impact parameter), near circular orbit around their host stars and easily add rotational deformation contributions to the planets shape. It can be shown that the rotational potential responsible for deformation at a point within the planet can also be written as a second degree solid harmonic [Dermott, 1979]. In fact the only difference between the two potentials is that the rotational deformation is 1/3 the magnitude of the tidal potential and has a different axis of symmetry (in the case we refer to here it is the z axis). As a result we can use the same shape function of the planet as we did before and linearly add the rotational and tidal contributions for the corresponding angles along their separate axes of symmetry. The resulting triaxial ellipsoid then has its axes parameterized as follows:

$$a = A(1 + \frac{7S_2}{6}) \tag{3.7}$$

$$b = A(1 - \frac{S_2}{3}) \tag{3.8}$$

$$c = A(1 - \frac{5S_2}{6}) \tag{3.9}$$

where a is the axis pointed towards the host star, b is the axis orthogonal to it in the planet-star system's equatorial plane and c is the orthogonal axis of rotation of the planet.

The synchronous orbit assumption ensures a special geometric configuration where the longest axis of the planet is always oriented towards the star - this ensures the mid transit alignment from the perspective of the observer will yield a predictable projected area of the planet transiting its host star given by the product of the two other orthogonal axes. The bias in transit depth at mid transit for a planet with mean radius $R_p$ is then just given by

$$\frac{(bc) - (R_p^2)}{R_s^2} \tag{3.10}$$

where $R_s$ is the mean radius of the star. This bias was calculated for a number of different planet sizes and different spectral classes. In particular, bias values were calculated for 1, 1.1447, 1.5, 2, 2.154 and 2.25 $R_e$ solid planets with bulk densities taken from the relation given in equation 1 of Weiss and Marcy [2014]. While that density relation was for putative terrestrial planets smaller then 1.5 $R_e$, we extend it to larger planets since the question of whether large planets close in can retain a significant gaseous envelope is still open. These bias values were calculated for 6 different main sequence spectral classes: M6, M5, M1, K, G, and F. Most of the images in this study will focus on results for the second smallest star (M5 V) as confirmed planet detections have only been made for stars down to that spectral class and because that is the limiting spectral type the *Transiting Exoplanet Survey Satellite (TESS)* [Ricker et al., 2014] will be sensitive to. Main sequence stars larger than F class stars were not tested as any bias or distortion signal would be too minimal given the large projected area of the stars - an assumption that is well founded based upon the following results and currently observed upper bounds on radii of solid planets [Dumusque et al., 2014b]. Physical parameters for M dwarfs were taken from literature [Reid and Hawley, 2005] while the parameters used for the F, G and K class stars were from well-known examples (61 Cygni (K5 V), The Sun (G2 V), Pi3 Orionis (F6 V) respectively).

Finally, orbital distances for which tidal bulges and biases were calculated were based on an inner distance defined by the fluid Roche limit of each star-planet system and an outer distance at which a 1.5 $M_e$ planet with the corresponding fitted bulk density would be tidally locked within 1 billion years around different stars [Gladman et al., 1996]. An initial spin rate of one rotation per 13.5hrs was used [Goldreich and Soter, 1966] based on the predicted initial spin state for Venus. This is a highly speculative choice but was made because the types of planets examined in this study are much larger than Mercury and because the most appropriate analogue choice, the Earth, has had its rotational history

significantly modified by interactions with the moon. In any event, initial rotation rates were varied from 1.5 hrs to 1 day and found to have minimal effect on the outer radius limit tested due to the one sixth power they are raised to. In addition, the induced tidal bulges raised closer to the outer distances are minimal for the purpose of this study. The fluid Roche limit is a conservative assumption as solid planets have been found interior to it [Rappaport et al., 2013] while bias and bulge estimates are minimal for the outer distance.

The importance of the synchronous rotation assumption necessitates a discussion of the likelihood of such a state. Recent work has shown that pseudosynchronous rotation for terrestrial bodies is an unphysical state based on an improper treatment of the tidal torque [Makarov and Efroimsky, 2013] and that most planets with a high enough eccentricity fall into higher order resonances. Given that many close-in planets have potentially been excited to higher eccentricities during their orbital history before their orbits were circularized this may mean that even for close-in planets synchronous rotation may be an atypical state.

However, there are different scenarios under which such planets which may fall into synchronous rotation - while these are used as justification for such an assumption, the potential to detect bulge signatures may also act as a test for the spin state. In particular, planets on very circular orbits with low eccentricity, planets that at some point were thrown into retrograde orbit (either by migration or capture), and bodies that were relatively cold and not very responsive to tidal torques may have fallen into synchronous rotation. Importantly, significantly triaxial bodies may also have a triaxiality caused torque if their average inertia axis is tilted with respect to the primary-secondary axis that can then compensate for the nonzero secular tidal torque and result in a synchronous orbit (Efroimsky 2014, private comm.).

### 3.2.2 Bias Results

Estimates of the distortion to a planet's shape around M5V and M1V stars are given in figure 3.9. These are the cases where the shape of the planet is the most deformed and where the deformation is most easily observable - in some cases reaching around a 3:2 ratio

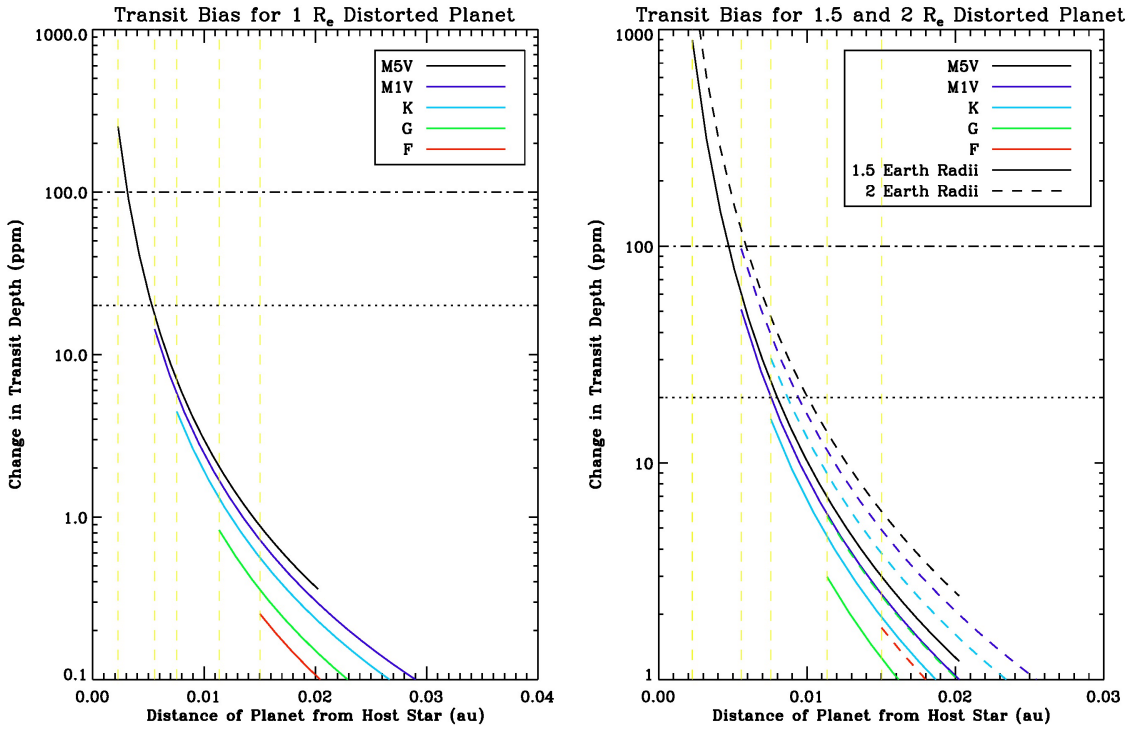


Figure 3.2: Transit biases for 1, 1.5 and 2.0 Earth Radii planets due to shape distortion from tidal and rotational effects. The dotted and dash dotted lines are 20 and 100 ppm levels. The vertical dashed yellow lines indicate the fluid Roche Limit for an M5V, M1V, K, G and F class star going from left to right for Earth like densities. Due to the one third power dependence on ratio of densities, the fluid Roche Limit for 1.5 and 2 Earth Radii planets isn't significantly different. The right panel contains transit bias values for 1.5 and 2 Earth radii

of the largest to smallest axis. The deformations to planetary shape swamp even some putative atmospheric heights in these cases. For example, for a 1.5 $R_e$ planet at the fluid Roche limit around a M5V star with an effective temperature of 2800, the atmospheric scale height of a pure sodium atmosphere [Miguel et al., 2011] at the substellar point of the planet is about 85 times smaller than the distortion of the planetary axis in that direction. This would suggest the gravitational potential gradient that exists for atmospheric flow from the substellar point to the terminators of these planets would appear to be significant and may potentially affect observational atmospheric retrieval. However, understanding of the dynamics of atmospheres of very hot close in planets is still very basic and would need to be explored in greater depth to derive any conclusions. The transit bias for a particular mean radius planet due to the smaller observed mid-transit cross section of the distorted planet is given in figure 3.2. The bias is shown for 1, 1.5, and 2 $R_e$ planets and results are close for the other similar sized planets. Dash-dot and dotted lines are given for 100 and 20 ppm thresholds which correspond to the *Kepler Telescope's* [Borucki et al., 2010] combined differential photometric precision over a 6.5 hour integration for a 15th and 12th magnitude star respectively.

For the smallest star tested, the M6 V star, the underestimates in transit depth can be very significant and indeed for 1.5 $R_e$ planets and larger over an order of magnitude greater than projected *TESS's* photometric precision of 200 ppm in 1 hour on an I=10 star. Even for a 1 $R_e$ planet the transit depth difference can approach about 0.1%. For the M5 V star the effects are somewhat smaller but still observationally significant for even the 200 ppm threshold for a 1 $R_e$ planet. The larger M1 V star may have biases which are not quite observationally significant for 1 $R_e$ but which become so for 1.5 $R_e$ planets and larger (in fact the 2 $R_e$ values reflected by the dashed green line are greater over equivalent distances then a 1.5 $R_e$ planet around an M5 V star). This suggests that for M dwarf stars such a bias needs to be considered when looking at close-in planets. In fact, for large solid planets 2 $R_e$ and greater it appears such an effect may even be detectable around larger K class dwarf stars. Unsurprisingly, the effect is small around the G and F class dwarf stars. Also

as expected, biases were smaller for planets with greater rigidity and larger for less rigid planets. The transit depth differences can then be calculated as the corresponding radius underestimates for the planets in each system as shown for planets around M1V and M5V stars in figure 3.4.

Figure 3.4 reflects the fact that planets which are the most distorted and which orbit smaller stars in this particular configuration will yield the most biased radius measurements. Radius underestimates are small and within uncertainty limits for planets around the much larger K and G Dwarf stars (see figure 3.3). However, in the case of the planets around the M5 V star, underestimates all reach about 1% by 0.005 AU and steeply increase to greater than 7% as they approach the fluid Roche limit. Around the larger M1 V star the

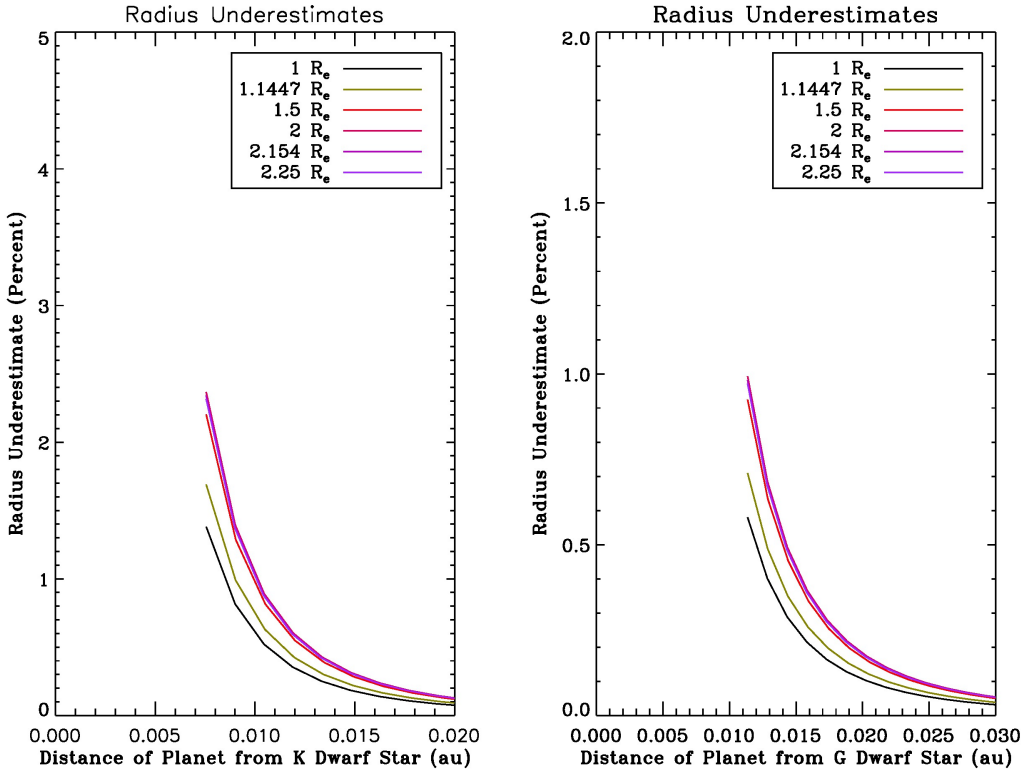


Figure 3.3: Radius underestimates for different sized solid planets due to tidal and rotational distortions. The left image is for synchronously rotating planets around K stars and right for G stars.

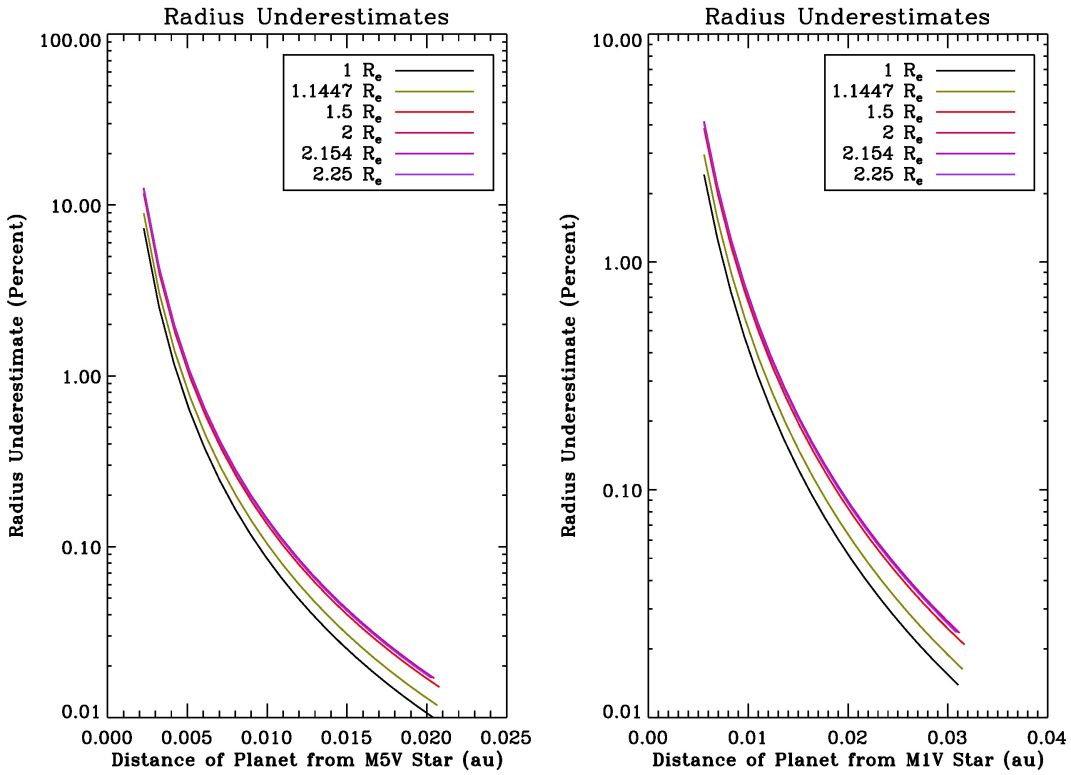


Figure 3.4: Radius underestimates for different sized solid planets due to tidal and rotational distortions. The left image is for synchronously rotating planets around M5 V stars and right for M1 V stars.

underestimates reach around 1% between .007 and 0.01 AU and range from about 2.5 to 5.5% at the fluid Roche limits. Underestimates are small for larger stars with values ranging from 0.5 to 1.5% at the fluid Roche limit for the G class dwarf star.

The radius underestimates result in density overestimates for these planets. For a 1% radius underestimate the calculated value for the density will actually be a 3% overestimate of the real value. For cases around the M5 V star density overestimates then range from 3% at 0.05 AU to about 20-25% greater than the actual value for a 7-10% radius underestimate at the fluid Roche limit. The 2.5-5.5% radius underestimates around the M1 V star correspond to estimated density values which are 7-15% greater than the actual value. Clearly, for some of these planets their aspherical shape can lead to significantly overestimated bulk

density values.

## 3.3 Photometric Signatures of Asphericity

### 3.3.1 In Transit Signatures

The synchronous rotation of these planets means that the projected area of a planet will appear to change as it travels around in orbit. The maximum projected area will be at quadrature in the planet's orbit around its host star as the two projected axes will be the longest axis and the polar axis. Conversely, at mid transit the projected area of the planet will be at a minimum as the visible axes will be the smallest axis and the polar axis. This change in projected area has been previously recognized as a potential signature of planetary asphericity that is proportional during the transit portion of the light curve to $R_s/a$ [Ragozzine and Wolf, 2009, Carter and Winn, 2010b] and has been generally assumed to be too minimal to use for system characterization. In addition, there have been concerns that such a signal would in any event be degenerate with stellar limb darkening contributions. However, the direct signal of an aspherical synchronous transiting planet should actually have the opposite effect of limb darkening by obscuring progressively less light through mid transit [Leconte et al., 2011, fig. 5] whereas stellar limb darkening effects result in a greater apparent stellar flux being blocked as the planet approaches mid transit. For unknown limb darkening parameters this signal may be difficult to extract but as we will discuss in the next section there now exists the potential to disentangle such effects.

Due to large bias values we saw for certain systems in the last section and the unique nature of a potential signal for an apsherical transiting planet we quantify the change in transit signal due to asphericity from the beginning of full transit to mid transit in the systems we examined. The change in the projected area of the planet in this case (from the beginning of full to mid transit) is roughly proportional to one half the projected angle of the full orbit subtended by the star. We calculate the total subtended angle of the transit as

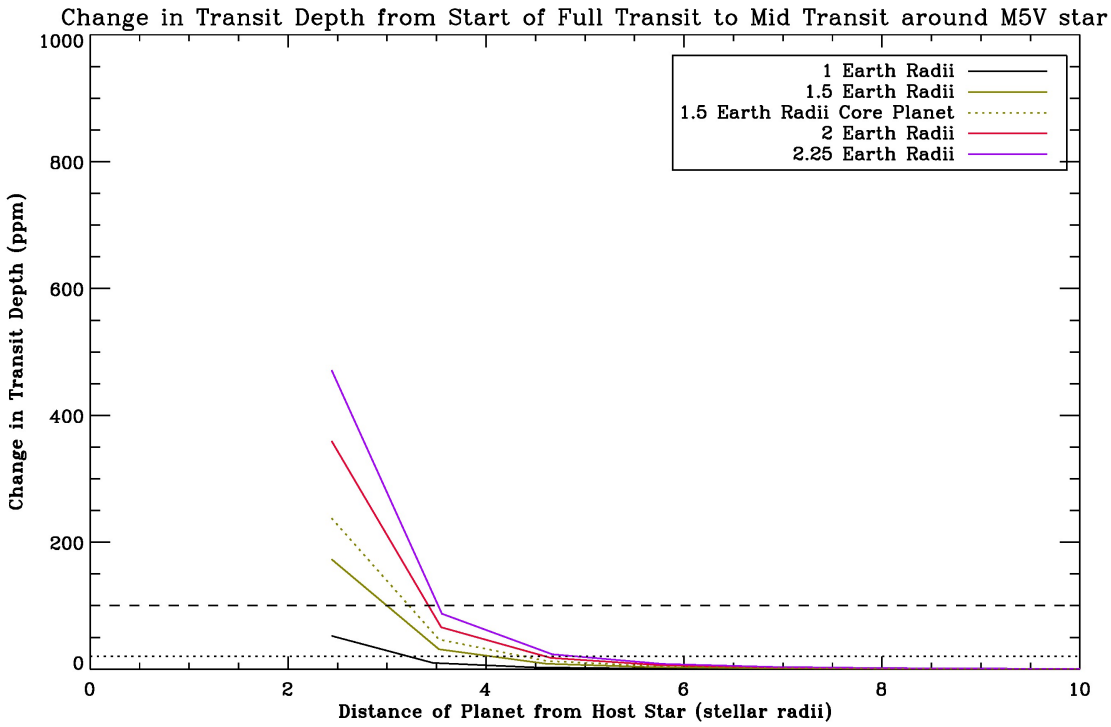


Figure 3.5: The change in transit depth from beginning of full transit to mid transit for different planets around an M5 V star.

$$\theta \approx \arcsin \frac{(R_s - R_p)}{a} \tag{3.11}$$

This is an approximate expression because the angles are calculated using the mean radius of the planet when finding the start of full transit. In reality at the beginning of full transit the planet will be rotated by the angle corresponding to the beginning of full transit and will have a slightly different b axis value - however the change in the area of the full planetary orbit that is subtended due to this effect is likely to be minimal (much smaller than change in total projected area of the planet as the planet transits). From this angle we then calculate the total change in transit depth from beginning of full transit to mid transit due to the changing projected area of the planet caused by its asphericity. We use

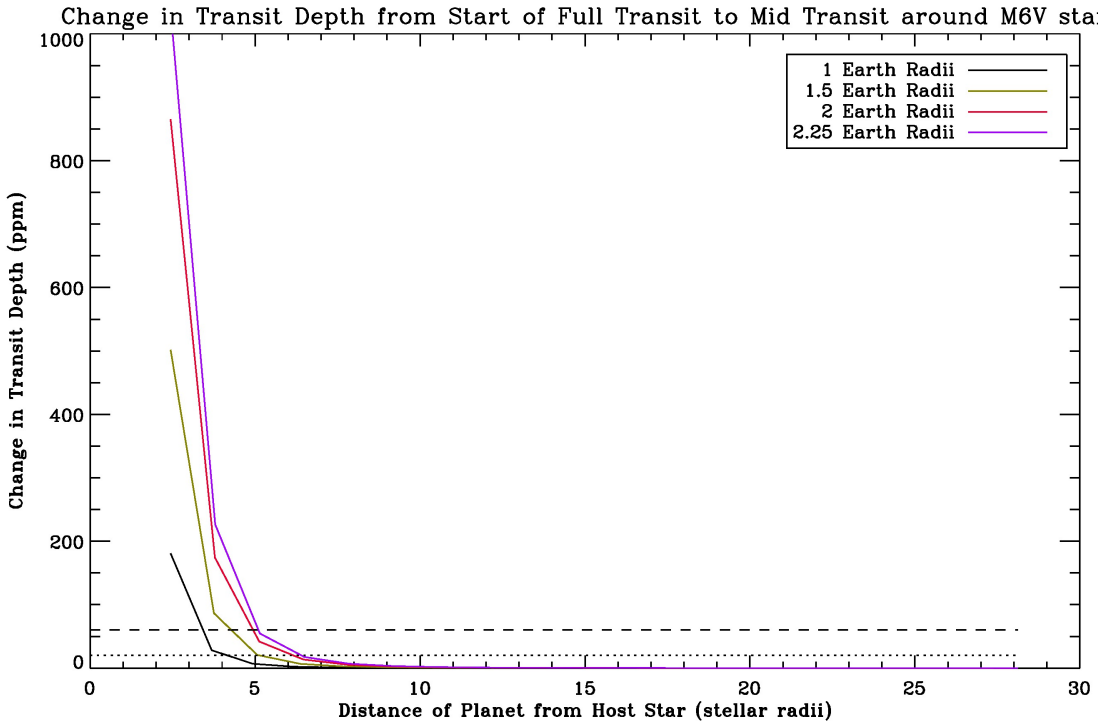


Figure 3.6: The change in transit depth from beginning of full transit to mid transit for different planets around an M6 V star. Depth changes remain above Kepler 20 ppm precision to distances near ∼3 fluid Roche limit radii.

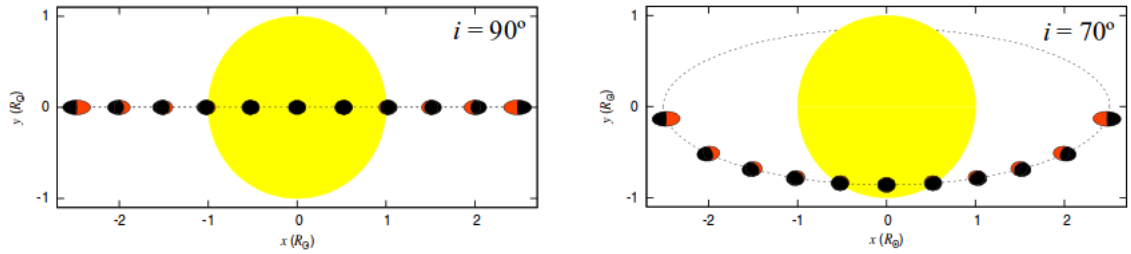


Figure 3.7: The change in a planet's apparent project area as it travels in synchronous orbit around it's host star. The majority of the change in projected area occurs in the out of the transit portion of the light curve because the star only subtends a small portion of the orbit. Ellipsoidal variations due to the apparent change in the shape of the planet may be a powerful way to constrain shape. Figure from Correia [2014]

the same equation as the one used to calculate the bias except the b axis is now rotated by the angle 90 - $\theta$ degrees for the projected area at the beginning of full transit and is compared to the mid transit projected area (with $\theta = 0$ at mid transit) versus an idealized spherical case. Thus while the rotational contribution to the b axis remains the same at the beginning of full transit in this co-planar case the tidal contribution we add to it is now $S_2(P_2 \cos(\frac{\pi}{2} - \psi))$.

The results of these calculations show that the change in transit depth during the course of the transit is minimal for most of the stars with the exception of the M dwarfs. Figure 3.5 of the change around an M5V star shows that close-in to smaller M dwarf stars the in-transit signature of a distorted planet may in fact be observationally detectable and significant. In fact, most of the planets tested yield signatures which exceed the 20 ppm limit at distances $\sim 2$ times the fluid Roche limit. Nearer to the fluid Roche limit the change in transit depth is much greater and even for the 1.5 Re case approaches 200 ppm. These signatures are increased by nearly a factor of two for M6 V stars (see figure 3.6). We also test whether such a direct signature can then also be used to constrain rigidity and find that near the fluid Roche limit the difference between the two planets meet or exceeds the 20 ppm threshold. The green dotted line for a 1.5 $R_e$ Iron-Ni Core remnant diverges from the 1.5 $R_e$ planet

with a rigidity value close to the Earths as they approach the fluid Roche limit.

### 3.3.2 Ellipsoidal Variations

The complementary change in the projected area of these planets occurs in the out of transit portion of the light curve (as demonstrated in figure 3.7). Since the area of the total orbit subtended by the in transit portion is typically small, most of the change in the projected area of the planet occurs when it is not transiting its host star. As a result one can use the long to short axis ratio of the deformed planet (given in figure 3.9) to approximate the total change in the emitted flux contribution from the planet in the out of transit portion of the light curve. Given a favorable planet to star contrast ratio in the infrared such changes may result in detectable ellipsoidal variations in the planet. Such a variation would be immune to stellar limb darkening and may be an effective pathway to constraining the asphericity and subsequently bulk properties of the planet. There may even be the potential to observe ellipsoidal variations in the star in conjunction with variations in the planet in order to constrain planetary bulk properties. Using the expression given in equation 2 of Faigler and Mazeh [2011] a 1.5 $R_e$ planet at its fluid Roche limit around a M5V star may be expected to produce ellipsoidal variations in the star of $\sim 10$ ppm assuming a stellar limb darkening coefficient of 1 from Claret [1998] and a stellar gravity darkening coefficient of 0.6.

## 3.4 Discussion and Analysis

From the results in the previous sections it is clear that for certain planet-star systems the tidal and rotational distortions to a solid planets shape can result in underestimates of those planets radii and subsequent values based off the inferred volume. Additionally, in the case of planets that are close in to smaller M dwarfs the distorted shapes of the planets may actually produce an observable signature of the shape in the transit itself. Statistical occurrence rates for such planets are still limited due to a lack of data for mid to late M dwarfs [Dressing and Charbonneau, 2013]. However solid planets interior to their fluid Roche limit, planets with orbital separations with similar a/$R_{stellar}$ values and planets

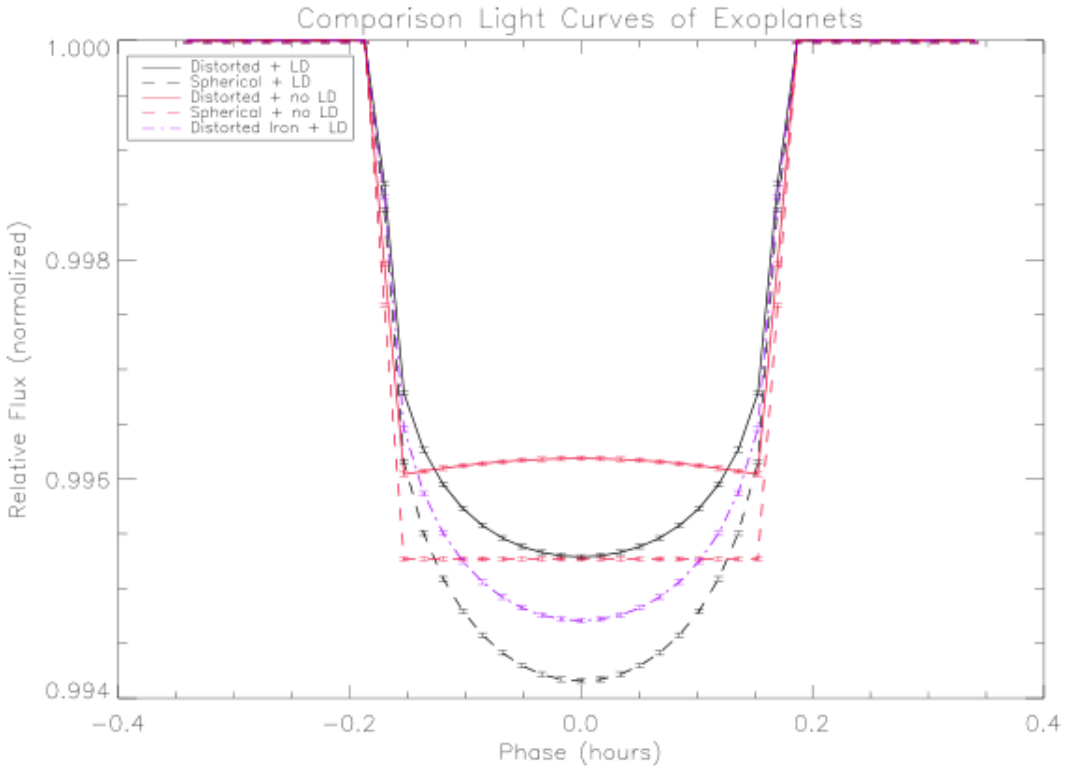


Figure 3.8: Light curves of a 1.5 $R_e$ planet transiting a M5V star at an orbital separation equal to the fluid Roche limit. Tidally and rotationally distorted planets with the empirically fit densities are given by the solid lines. Spherical planets are given by the dashed lines. The putative distorted Iron planet is given by the purple dash dot line. Red lines correspond to cases with no stellar limb darkening while black lines correspond to cases with stellar limb darkening values produced by Exofast for the relevant stellar parameters. Error bars correspond to the 20 ppm uncertainty.

close to the fluid Roche limit for other stellar classes have all been found. The variation of rigidity of a planet may produce a small but detectable signal in the cases that were tested as one gets very close to the fluid Roche limit, and again it is important to remember planets have also been detected interior to the fluid Roche limit (the inner distance bound). Merely the constraining of tidal bulge amplitude along with Roche limit considerations may put meaningful limits on interior structure. The ability to directly constrain the shape of a planet would provide clues towards tidal theory, the orbital configuration of the system and bulk properties of the planet.

Our group's preliminary work (see figure 3.8) on the nature of such a signature suggests that such an effect can make the transit portion of a light curve more box-like as a planet's decreasing projected area towards mid transit in effect compensates for some of the limb darkening effects - an effect that has already been noted in the case of WASP-12b [Cowan et al., 2012]. Limb darkening effects are several factors greater than the effect of asphericity in figure 3.8 and as a result the distinctive W shape of the transit produced by asphericity is not visible and instead manifests itself as what may be interpreted as merely different stellar limb darkening parameter fits. Specific studies of distorted planets in synchronous orbit may be able to use limb darkening studies of similar host stars [Müller et al., 2013] to resolve the effect of the distortion, though care needs to be taken when fixing the limb darkening parameters [Csizmadia et al., 2013]. Close-in planets may also typically be in multi planet systems with other planets farther out [Sanchis-Ojeda et al., 2014] which may enable comparative studies of the planets' transits to help glean shape effects from an ultra short period planet. Limb darkening degeneracies may also be broken by obtaining light curves in multiple wavelengths using the *Spitzer Space Telescope* [Werner et al., 2004] and in the future, the *James Webb Space Telescope* [Gardner et al., 2006]. Finally, additional thermal and reflected phase variation effects of an aspherical planet [Budaj, 2011] may also be helpful in corroborating the in-transit signature of a planet's shape, particularly given that these extremely hot planets may lack degeneracy inducing atmospheres. While ellipsoidal variations in the star which are induced by the planet's tidal effect may complicate

this [Loeb and Gaudi, 2003] they may be able to be estimated.

The assumptions made to calculate the specific biases and signatures are not likely to hold for many systems. However, the general physical principles will apply across a number of different planet-star systems and should be applicable when considering the more general question of determining the spin state of a planet. Given that the equilibrium tide can produce potentially observable signatures for planets around some stars even when considering rotational deformation, such a signature may produce idiosyncratic signatures for planets in particular resonances or even more general orbital configurations. This needs to be explored for simple cases including those that examine gas giants and then also for more realistic cases that vary orbital parameters. Indeed, there have been dozens of Hot Jupiters found interior to 2.5 Roche radii of their stars [Gillon et al., 2014, fig. 4]. Finally, for solid planets it is clear that planetary systems around M dwarfs may be particularly amenable to exploration of the orbital state and bulk characteristics of a planet due to the compact nature of allowed systems, the tendency for such stars to host smaller planets and the simple fact that any planetary effect will have a much larger observational signature around these smaller stars. This should encourage investigations of M dwarfs in addition to the current work of the MEarth survey [Nutzman and Charbonneau, 2008] and *K2 mission* [Howell et al., 2014] and the planned survey of close and bright M dwarfs by *TESS*.

### 3.4.1 Relevance to Existing and Future Data

Further encouragement of investigations of exoplanet asphericity comes from estimates of how many such planets current and future missions are expected to detect. Table 3.4.1 indicates that there will be a number of aspherical exoplanets detected that may be potential Rosetta Stones for exoplanet characterization. These estimates were made based upon occurrence rate estimates for close-in planets combined with the number of M dwarf stars that will be or have been targeted by different missions - this focus on M dwarfs follows from the findings of this project which have shown that those are the systems that are most amenable to exoplanet asphericity characterization. There are two complicating factors that

will affect yields - magnitude dependent precision of potential targets and the stellar activity of stars most likely to host characterizable aspherical exoplanets. Since, M dwarfs are less luminous than larger counterparts, their photometric statistics are often poorer. This results in coarser precision levels for potential systems. However, the likelihood of multiple transits due to the close in nature of the planets of interest combined with the purposeful targeting of the brightest M dwarf candidates is likely to mitigate precision issues to some extent. The other factor is related to the potential for magnetic activity of host stars to make planetary and asphericity characterization more difficult. The literature suggests that mid to late type M dwarfs may possess somewhat greater stellar activity [Browning et al., 2010] than early type M dwarfs. This additional stellar activity may also make identification and characterization of asphericity more difficult. However, despite those factors, just the sheer number of potential aspherical candidates puts the odds in favor of characterization efforts. In fact, there may already be solid planets in existing archives that have retrievable asphericity signatures.

Table 3.1: Expected Aspherical Exoplanet Yields

| Mission | Years of Operation | # of M Dwarf Stars targeted | Expected Yield[1,6] of Characterizable Aspherical Rocky Planets | Expected Yield of[1,6] Characterizable Aspherical Gaseous and Rocky Planets |
|---|---|---|---|---|
| Kepler[2] | 2009-2013 | $\sim 3000$ | $\sim 10$ | $\sim 15$ |
| K2[3] | 2014-2016 | >2000 | $\sim 5$ | $\sim 10$ |
| TESS[4] | 2017-2020 | >1000 | $\geq 3$ | >5 |
| PLATO[5] | 2024-2030 | >5000 | >13 | >25 |

[1] Using M dwarf Occurrence Rates of 1% for likely solid planets on sub 1.25 day orbits and 2.5% for large rocky and gaseous on sub 1.75 day planets on sub 1.75 day orbits from [Dressing and Charbonneau, 2015]
[2] M dwarfs targeted from [Batalha et al., 2010] - yields taken from NASA Exoplanet Archive
[3] Estimate of Targeted M Dwarfs from accepted proposals listed on K2 mission website
[4] Information taken from [Ricker et al., 2014]
[5] [PLATO Study Team, 2013]
[6] Probability of transit calculated using a 1.25 day (∼25%) and 1.75 day (∼20%) orbit respectively around an M1V star

In figure 3.9, I have plotted Kepler Objects of Interest from the Exoplanet Archive [Akeson et al., 2013] which are either confirmed or candidate planets of radius<1.6 $R_e$ that have an orbital separation greater than their fluid Roche limit and less than 8 stellar radii and which orbit stars whose temperature and radii are less than or equal to that of a K class main sequence star. The expected long to short axis ratios for these are produced using the same assumptions as in Saxena et al. [2015] and are plotted as a function of their orbital distance and compared to the expected axis ratios of different sized solid planets orbiting at comparable distances around M5V, M1V and K class stars. It is apparent that at least some of these planets have axis ratios greater than 1.03 and may produce signals which are detectable in their analagous cases. This is particularly interesting given the fact that this plot actually probably undersells the case that there likely already exists data for solid planets that have detectable and constrainable asphericity because that plot does not include several dozen other Kepler candidates that are located *interior* to their putative

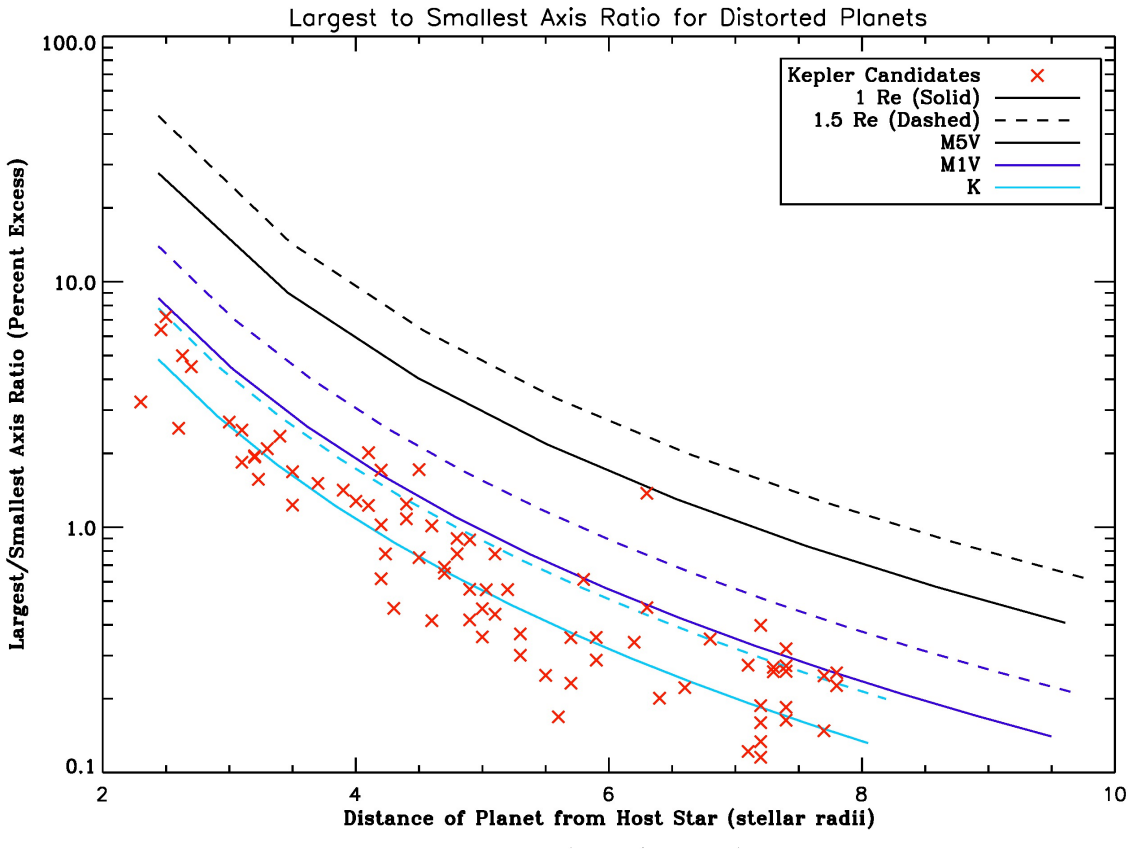


Figure 3.9: The ratio of the longest to smallest axis for triaxial ellipsoid planets of 1 and 1.5 $R_e$ orbiting M5V, M1V and K stars. X's are long/short axis ratio values calculated for specific close in Kepler Objects of Interest using the methodology in Saxena et al. [2015]. The methodology includes a bulk rigidity similar to the Earth, a density taken from Weiss and Marcy [2014], and a circular orbit coplanar with the star's equator. For 1.5 Earth Radii planets orbiting an M5V star the ratio can approach 3:2 near the fluid Roche limit and around M1V stars a longest axis about 10% larger than the shortest axis is typical for both planets near the fluid Roche limit. *This suggests that data for candidates with detectable asphericity lurks in existing archives, and that a focus on lower mass stars will yield even more targets.*

fluid Roche limit (which was the conservative assumption used in the early calculations) [Sanchis-Ojeda et al., 2014].

Finally, the reason the top half of figure 3.9 doesn't have as many overlaid Kepler candidates is a function of the fact that surveys up to this point haven't targeted the mid type M dwarfs for which the most unambiguous asphericity signals likely exist. For the

candidates overplotted here and candidates identified around lower mass stars in Kepler there is a general bias towards K and early type M dwarf stars [Dressing and Charbonneau, 2013] because of Kepler's focus on sun-like stars. Thankfully, the near future holds attempts to fill in this data gap as K2, TESS and the MEarth surveys will all observe some of the closest and brightest mid type M dwarfs. If the yield resembles what surveys up to this point have found there will be an urgent need for a way to constrain and interpret asphericity of detected close in planets and unlock the physical secrets that lurk within those distorted planets' signatures.

# Chapter 4: Conclusion including Current and Future Work

The work done as part of this thesis leads to two main conclusions:

- Simplified models for the atmosphere and resurfacing on close-in solid exoplanets indicate that resurfacing on those planets can be significant enough to effect the rotation of those planets. The resurfacing on these planets may also produce observable transit signatures.

- An examination of the tidal and rotational distortion of the same planets indicates that their predicted asphericity should already be observable and will certainly be observable in the near future. Such asphericity may also be a critical tool in characterizing bulk parameters of these planets and be an important key to understanding their rotation and climates.

In addition to those projects, a related topic which is currently being explored is an examination of the effect of planetary asphericity of these planets on the dynamics of their atmospheres in ways that impact atmospheric retrieval. Given the likely long to short axis ratios demonstrated for such planets, there exists the potential for effects analogous to gravity darkening and brightening in their atmospheres. This in turn has the potential to influence atmospheric retrieval  providing potential atmospheric markers even on planets around larger stars where transit features are not typically extractable. As a result, asphericity and it's subsequent scientific value may be extractable using spectroscopy. This project will focus on the aspherical length scales where such effects become relevant to the atmosphere by impacting variables such as atmospheric temperature, pressure and velocity.

# Bibliography

M. Agúndez, V. Parmentier, O. Venot, F. Hersant, and F. Selsis. Pseudo 2D chemical model of hot-Jupiter atmospheres: application to HD 209458b and HD 189733b. *AAP*, 564:A73, Apr. 2014. doi: 10.1051/0004-6361/201322895.

R. L. Akeson, X. Chen, D. Ciardi, M. Crane, J. Good, M. Harbut, E. Jackson, S. R. Kane, A. C. Laity, S. Leifer, M. Lynn, D. L. McElroy, M. Papin, P. Plavchan, S. V. Ramírez, R. Rey, K. von Braun, M. Wittman, M. Abajian, B. Ali, C. Beichman, A. Beekley, G. B. Berriman, S. Berukoff, G. Bryden, B. Chan, S. Groom, C. Lau, A. N. Payne, M. Regelson, M. Saucedo, M. Schmitz, J. Stauffer, P. Wyatt, and A. Zhang. The NASA Exoplanet Archive: Data and Tools for Exoplanet Research. *PASP*, 125:989–999, aug 2013. doi: 10.1086/672273.

L. Arnold, D. Ehrenreich, A. Vidal-Madjar, X. Dumusque, C. Nitschelm, R. R. Querel, P. Hedelt, J. Berthier, C. Lovis, C. Moutou, R. Ferlet, and D. Crooker. The Earth as an extrasolar transiting planet. II. HARPS and UVES detection of water vapour, biogenic $O_2$, and $O_3$. *AAP*, 564:A58, Apr. 2014. doi: 10.1051/0004-6361/201323041.

V. Bailey, T. Meshkat, M. Reiter, K. Morzinski, J. Males, K. Y. L. Su, P. M. Hinz, M. Kenworthy, D. Stark, E. Mamajek, R. Briguglio, L. M. Close, K. B. Follette, A. Puglisi, T. Rodigas, A. J. Weinberger, and M. Xompero. HD 106906 b: A Planetary-mass Companion Outside a Massive Debris Disk. *ApJL*, 780:L4, Jan. 2014. doi: 10.1088/2041-8205/780/1/L4.

P. Ballerini, G. Micela, A. F. Lanza, and I. Pagano. Multiwavelength flux variations induced

by stellar magnetic activity: effects on planetary transits. *AAP*, 539:A140, Mar. 2012. doi: 10.1051/0004-6361/201117102.

I. Baraffe, G. Chabrier, J. Fortney, and C. Sotin. Planetary Internal Structures. *Protostars and Planets VI*, pages 763–786, 2014. doi: $10.2458/\mathrm{azu}_u apress_9 780816531240 - ch033$.

T. Barclay, J. F. Rowe, J. J. Lissauer, D. Huber, F. Fressin, S. B. Howell, S. T. Bryson, W. J. Chaplin, J.-M. Désert, E. D. Lopez, G. W. Marcy, F. Mullally, D. Ragozzine, G. Torres, E. R. Adams, E. Agol, D. Barrado, S. Basu, T. R. Bedding, L. A. Buchhave, D. Charbonneau, J. L. Christiansen, J. Christensen-Dalsgaard, D. Ciardi, W. D. Cochran, A. K. Dupree, Y. Elsworth, M. Everett, D. A. Fischer, E. B. Ford, J. J. Fortney, J. C. Geary, M. R. Haas, R. Handberg, S. Hekker, C. E. Henze, E. Horch, A. W. Howard, R. C. Hunter, H. Isaacson, J. M. Jenkins, C. Karoff, S. D. Kawaler, H. Kjeldsen, T. C. Klaus, D. W. Latham, J. Li, J. Lillo-Box, M. N. Lund, M. Lundkvist, T. S. Metcalfe, A. Miglio, R. L. Morris, E. V. Quintana, D. Stello, J. C. Smith, M. Still, and S. E. Thompson. A sub-Mercury-sized exoplanet. *Nature*, 494:452–454, Feb. 2013. doi: 10.1038/nature11914.

J. W. Barnes. Effects of Orbital Eccentricity on Extrasolar Planet Transit Detectability and Light Curves. *PASP*, 119:986–993, Sept. 2007. doi: 10.1086/522039.

J. W. Barnes and J. J. Fortney. Measuring the Oblateness and Rotation of Transiting Extrasolar Giant Planets. *ApJ*, 588:545–556, May 2003. doi: 10.1086/373893.

R. Barnes, S. N. Raymond, R. Greenberg, B. Jackson, and N. A. Kaib. CoRoT-7b: Super-Earth or Super-Io? *ApJL*, 709:L95–L98, Feb. 2010. doi: 10.1088/2041-8205/709/2/L95.

N. J. Baskin, H. A. Knutson, A. Burrows, J. J. Fortney, N. K. Lewis, E. Agol, D. Charbonneau, N. B. Cowan, D. Deming, J.-M. Desert, J. Langton, G. Laughlin, and A. P. Showman. Secondary Eclipse Photometry of the Exoplanet WASP-5b with Warm Spitzer. *ApJ*, 773: 124, Aug. 2013. doi: 10.1088/0004-637X/773/2/124.

N. M. Batalha, W. J. Borucki, D. G. Koch, S. T. Bryson, M. R. Haas, T. M. Brown, D. A. Caldwell, J. R. Hall, R. L. Gilliland, D. W. Latham, S. Meibom, and D. G. Monet. Selection,

Prioritization, and Characteristics of Kepler Target Stars. *ApJL*, 713:L109–L114, Apr. 2010. doi: 10.1088/2041-8205/713/2/L109.

J. L. Bean, E. Miller-Ricci Kempton, and D. Homeier. A ground-based transmission spectrum of the super-Earth exoplanet GJ 1214b. *Nature*, 468:669–672, Dec. 2010. doi: 10.1038/nature09596.

B. Béky, D. M. Kipping, and M. J. Holman. SPOTROD: a semi-analytic model for transits of spotted stars. *MNRAS*, 442:3686–3699, Aug. 2014. doi: 10.1093/mnras/stu1061.

J. Bento, P. J. Wheatley, C. M. Copperwheat, J. J. Fortney, V. S. Dhillon, R. Hickman, S. P. Littlefair, T. R. Marsh, S. G. Parsons, and J. Southworth. Optical transmission photometry of the highly inflated exoplanet WASP-17b. *MNRAS*, 437:1511–1518, Jan. 2014. doi: 10.1093/mnras/stt1979.

S. V. Berdyugina, A. V. Berdyugin, D. M. Fluri, and V. Piirola. Polarized Reflected Light from the Exoplanet HD189733b: First Multicolor Observations and Confirmation of Detection. *ApJL*, 728:L6, Feb. 2011. doi: 10.1088/2041-8205/728/1/L6.

A. S. Bonomo, A. Sozzetti, C. Lovis, L. Malavolta, K. Rice, L. A. Buchhave, D. Sasselov, A. C. Cameron, D. W. Latham, E. Molinari, F. Pepe, S. Udry, L. Affer, D. Charbonneau, R. Cosentino, C. D. Dressing, X. Dumusque, P. Figueira, A. F. M. Fiorenzano, S. Gettel, A. Harutyunyan, R. D. Haywood, K. Horne, M. Lopez-Morales, M. Mayor, G. Micela, F. Motalebi, V. Nascimbeni, D. F. Phillips, G. Piotto, D. Pollacco, D. Queloz, D. Ségransan, A. Szentgyorgyi, and C. Watson. Characterization of the Kepler-101 planetary system with HARPS-N. A hot super-Neptune with an Earth-sized low-mass companion. *ArXiv e-prints*, Sept. 2014.

W. J. Borucki, D. Koch, G. Basri, N. Batalha, T. Brown, D. Caldwell, J. Caldwell, J. Christensen-Dalsgaard, W. D. Cochran, E. DeVore, E. W. Dunham, A. K. Dupree, T. N. Gautier, J. C. Geary, R. Gilliland, A. Gould, S. B. Howell, J. M. Jenkins, Y. Kondo, D. W.

Latham, G. W. Marcy, S. Meibom, H. Kjeldsen, J. J. Lissauer, D. G. Monet, D. Morrison, D. Sasselov, J. Tarter, A. Boss, D. Brownlee, T. Owen, D. Buzasi, D. Charbonneau, L. Doyle, J. Fortney, E. B. Ford, M. J. Holman, S. Seager, J. H. Steffen, W. F. Welsh, J. Rowe, H. Anderson, L. Buchhave, D. Ciardi, L. Walkowicz, W. Sherry, E. Horch, H. Isaacson, M. E. Everett, D. Fischer, G. Torres, J. A. Johnson, M. Endl, P. MacQueen, S. T. Bryson, J. Dotson, M. Haas, J. Kolodziejczak, J. Van Cleve, H. Chandrasekaran, J. D. Twicken, E. V. Quintana, B. D. Clarke, C. Allen, J. Li, H. Wu, P. Tenenbaum, E. Verner, F. Bruhweiler, J. Barnes, and A. Prsa. Kepler Planet-Detection Mission: Introduction and First Results. *Science*, 327:977–, Feb. 2010. doi: 10.1126/science.1185402.

V. Bourrier, A. Lecavelier des Etangs, and A. Vidal-Madjar. The Mg i line: a new probe of the atmospheres of evaporating exoplanets. *AAP*, 573:A11, Jan. 2015. doi: 10.1051/0004-6361/201323266.

M. K. Browning, G. Basri, G. W. Marcy, A. A. West, and J. Zhang. Rotation and Magnetic Activity in a Sample of M-Dwarfs. *AJ*, 139:504–518, Feb. 2010. doi: 10.1088/0004-6256/139/2/504.

L. A. Buchhave, M. Bizzarro, D. W. Latham, D. Sasselov, W. D. Cochran, M. Endl, H. Isaacson, D. Juncher, and G. W. Marcy. Three regimes of extrasolar planet radius inferred from host star metallicities. *Nature*, 509:593–595, May 2014. doi: 10.1038/nature13254.

J. Budaj. The Reflection Effect in Interacting Binaries or in Planet-Star Systems. *AJ*, 141: 59, Feb. 2011. doi: 10.1088/0004-6256/141/2/59.

K. E. Bullen. The Interiors of the Planets. *ARA&A*, 7:177, 1969. doi: 10.1146/annurev.aa.07.090169.001141.

A. S. Burrows. Highlights in the study of exoplanet atmospheres. *Nature*, 513:345–352, Sept. 2014. doi: 10.1038/nature13782.

J. R. Burton, C. A. Watson, A. Fitzsimmons, D. Pollacco, V. Moulds, S. P. Littlefair, and P. J. Wheatley. Tidally Distorted Exoplanets: Density Corrections for Short-period Hot-Jupiters

Based Solely on Observable Parameters. *ApJ*, 789:113, July 2014. doi: 10.1088/0004-637X/789/2/113.

J. A. Carter and J. N. Winn. Empirical Constraints on the Oblateness of an Exoplanet. *ApJ*, 709:1219–1229, Feb. 2010a. doi: 10.1088/0004-637X/709/2/1219.

J. A. Carter and J. N. Winn. The Detectability of Transit Depth Variations Due to Exoplanetary Oblateness and Spin Precession. *ApJ*, 716:850–856, June 2010b. doi: 10.1088/0004-637X/716/1/850.

A. Cassan, D. Kubas, J.-P. Beaulieu, M. Dominik, K. Horne, J. Greenhill, J. Wambsganss, J. Menzies, A. Williams, U. G. Jørgensen, A. Udalski, D. P. Bennett, M. D. Albrow, V. Batista, S. Brillant, J. A. R. Caldwell, A. Cole, C. Coutures, K. H. Cook, S. Dieters, D. D. Prester, J. Donatowicz, P. Fouqué, K. Hill, N. Kains, S. Kane, J.-B. Marquette, R. Martin, K. R. Pollard, K. C. Sahu, C. Vinter, D. Warren, B. Watson, M. Zub, T. Sumi, M. K. Szymański, M. Kubiak, R. Poleski, I. Soszynski, K. Ulaczyk, G. Pietrzyński, and Ł. Wyrzykowski. One or more bound planets per Milky Way star from microlensing observations. *Nature*, 481:167–169, Jan. 2012. doi: 10.1038/nature10684.

T. Castan and K. Menou. Atmospheres of Hot Super-Earths. *ApJL*, 743:L36, Dec. 2011. doi: 10.1088/2041-8205/743/2/L36.

S. Chandrasekhar. The equilibrium of distorted polytropes. I. The rotational problem. *MNRAS*, 93:390–406, Mar. 1933.

S. Charpinet, G. Fontaine, P. Brassard, E. M. Green, V. Van Grootel, S. K. Randall, R. Silvotti, A. S. Baran, R. H. Østensen, S. D. Kawaler, and J. H. Telting. A compact system of small planets around a former red-giant star. *Nature*, 480:496–499, Dec. 2011. doi: 10.1038/nature10631.

A. Claret. Very low mass stars: non-linearity of the limb-darkening laws. *AAP*, 335:647–653, July 1998.

A. C. M. Correia. Transit light curve and inner structure of close-in planets. *AAP*, 570:L5, Oct. 2014. doi: 10.1051/0004-6361/201424733.

N. B. Cowan and E. Agol. The Statistics of Albedo and Heat Recirculation on Hot Exoplanets. *ApJ*, 729:54, Mar. 2011. doi: 10.1088/0004-637X/729/1/54.

N. B. Cowan, E. Agol, and D. Charbonneau. Hot nights on extrasolar planets: mid-infrared phase variations of hot Jupiters. *MNRAS*, 379:641–646, Aug. 2007. doi: 10.1111/j.1365-2966.2007.11897.x.

N. B. Cowan, P. Machalek, B. Croll, L. M. Shekhtman, A. Burrows, D. Deming, T. Greene, and J. L. Hora. Thermal Phase Variations of WASP-12b: Defying Predictions. *ApJ*, 747: 82, Mar. 2012. doi: 10.1088/0004-637X/747/1/82.

I. J. M. Crossfield, B. M. S. Hansen, J. Harrington, J. Y.-K. Cho, D. Deming, K. Menou, and S. Seager. A New 24 $\mu$m Phase Curve for  Andromedae b. *ApJ*, 723:1436–1446, Nov. 2010. doi: 10.1088/0004-637X/723/2/1436.

S. Csizmadia, T. Pasternacki, C. Dreyer, J. Cabrera, A. Erikson, and H. Rauer. The effect of stellar limb darkening values on the accuracy of the planet radii derived from photometric transit observations. *AAP*, 549:A9, Jan. 2013. doi: 10.1051/0004-6361/201219888.

D. Deming, A. Wilkins, P. McCullough, A. Burrows, J. J. Fortney, E. Agol, I. Dobbs-Dixon, N. Madhusudhan, N. Crouzet, J.-M. Desert, R. L. Gilliland, K. Haynes, H. A. Knutson, M. Line, Z. Magic, A. M. Mandell, S. Ranjan, D. Charbonneau, M. Clampin, S. Seager, and A. P. Showman. Infrared Transmission Spectroscopy of the Exoplanets HD 209458b and XO-1b Using the Wide Field Camera-3 on the Hubble Space Telescope. *ApJ*, 774:95, Sept. 2013. doi: 10.1088/0004-637X/774/2/95.

D. Deming, H. Knutson, J. Kammer, B. J. Fulton, J. Ingalls, S. Carey, A. Burrows, J. J. Fortney, K. Todorov, E. Agol, N. Cowan, J.-M. Desert, J. Fraine, J. Langton, C. Morley, and A. P. Showman. Spitzer Secondary Eclipses of the Dense, Modestly-irradiated, Giant Exoplanet HAT-P-20b Using Pixel-Level Decorrelation. *ArXiv e-prints*, Nov. 2014.

S. F. Dermott. Shapes and gravitational moments of satellites and asteroids. *Icarus*, 37: 575–586, Mar. 1979. doi: 10.1016/0019-1035(79)90015-0.

H. Diamond-Lowe, K. B. Stevenson, J. L. Bean, M. R. Line, and J. J. Fortney. New Analysis Indicates No Thermal Inversion in the Atmosphere of HD 209458b. *ApJ*, 796:66, Nov. 2014. doi: 10.1088/0004-637X/796/1/66.

C. Dorn, A. Khan, K. Heng, Y. Alibert, J. A. D. Connolly, W. Benz, and P. Tackley. Can we constrain interior structure of rocky exoplanets from mass and radius measurements? *ArXiv e-prints*, Feb. 2015.

C. D. Dressing and D. Charbonneau. The Occurrence Rate of Small Planets around Small Stars. *ApJ*, 767:95, Apr. 2013. doi: 10.1088/0004-637X/767/1/95.

C. D. Dressing and D. Charbonneau. The Occurrence of Potentially Habitable Planets Orbiting M Dwarfs Estimated from the Full Kepler Dataset and an Empirical Measurement of the Detection Sensitivity. *ArXiv e-prints*, Jan. 2015.

X. Dumusque, I. Boisse, and N. C. Santos. SOAP 2.0: A Tool to Estimate the Photometric and Radial Velocity Variations Induced by Stellar Spots and Plages. *ApJ*, 796:132, Dec. 2014a. doi: 10.1088/0004-637X/796/2/132.

X. Dumusque, A. S. Bonomo, R. D. Haywood, L. Malavolta, D. Ségransan, L. A. Buchhave, A. Collier Cameron, D. W. Latham, E. Molinari, F. Pepe, S. Udry, D. Charbonneau, R. Cosentino, C. D. Dressing, P. Figueira, A. F. M. Fiorenzano, S. Gettel, A. Harutyunyan, K. Horne, M. Lopez-Morales, C. Lovis, M. Mayor, G. Micela, F. Motalebi, V. Nascimbeni, D. F. Phillips, G. Piotto, D. Pollacco, D. Queloz, K. Rice, D. Sasselov, A. Sozzetti, A. Szentgyorgyi, and C. Watson. The Kepler-10 Planetary System Revisited by HARPS-N: A Hot Rocky World and a Solid Neptune-Mass Planet. *ApJ*, 789:154, July 2014b. doi: 10.1088/0004-637X/789/2/154.

D. Ehrenreich and J.-M. Désert. Mass-loss rates for transiting exoplanets. *AAP*, 529:A136, May 2011. doi: 10.1051/0004-6361/201016356.

L. T. Elkins-Tanton and S. Seager. Ranges of Atmospheric Mass and Composition of Super-Earth Exoplanets. *ApJ*, 685:1237–1246, Oct. 2008. doi: 10.1086/591433.

S. Faigler and T. Mazeh. Photometric detection of non-transiting short-period low-mass companions through the beaming, ellipsoidal and reflection effects in Kepler and CoRoT light curves. *MNRAS*, 415:3921–3928, Aug. 2011. doi: 10.1111/j.1365-2966.2011.19011.x.

B. Fegley and A. G. W. Cameron. A vaporization model for iron/silicate fractionation in the Mercury protoplanet. *Earth and Planetary Science Letters*, 82:207–222, Apr. 1987. doi: 10.1016/0012-821X(87)90196-8.

J. J. Fortney, C. S. Cooper, A. P. Showman, M. S. Marley, and R. S. Freedman. The Influence of Atmospheric Dynamics on the Infrared Spectra and Light Curves of Hot Jupiters. *ApJ*, 652:746–757, Nov. 2006. doi: 10.1086/508442.

J. J. Fortney, M. S. Marley, and J. W. Barnes. Planetary Radii across Five Orders of Magnitude in Mass and Stellar Insolation: Application to Transits. *ApJ*, 659:1661–1672, Apr. 2007. doi: 10.1086/512120.

C. M. R. Fowler. *The Solid Earth*. Feb. 2005.

J. Fraine, D. Deming, B. Benneke, H. Knutson, A. Jordán, N. Espinoza, N. Madhusudhan, A. Wilkins, and K. Todorov. Water vapour absorption in the clear atmosphere of a Neptune-sized exoplanet. *Nature*, 513:526–529, Sept. 2014. doi: 10.1038/nature13785.

F. Fressin, G. Torres, J.-M. Désert, D. Charbonneau, N. M. Batalha, J. J. Fortney, J. F. Rowe, C. Allen, W. J. Borucki, T. M. Brown, S. T. Bryson, D. R. Ciardi, W. D. Cochran, D. Deming, E. W. Dunham, D. C. Fabrycky, T. N. Gautier, III, R. L. Gilliland, C. E. Henze, M. J. Holman, S. B. Howell, J. M. Jenkins, K. Kinemuchi, H. Knutson, D. G. Koch, D. W. Latham, J. J. Lissauer, G. W. Marcy, D. Ragozzine, D. D. Sasselov, M. Still, P. Tenenbaum, and K. Uddin. Kepler-10 c: a 2.2 Earth Radius Transiting Planet in a Multiple System. *ApJS*, 197:5, Nov. 2011. doi: 10.1088/0067-0049/197/1/5.

J. P. Gardner, J. C. Mather, M. Clampin, R. Doyon, M. A. Greenhouse, H. B. Hammel, J. B. Hutchings, P. Jakobsen, S. J. Lilly, K. S. Long, J. I. Lunine, M. J. McCaughrean, M. Mountain, J. Nella, G. H. Rieke, M. J. Rieke, H.-W. Rix, E. P. Smith, G. Sonneborn, M. Stiavelli, H. S. Stockman, R. A. Windhorst, and G. S. Wright. The James Webb Space Telescope. , 123:485–606, Apr. 2006. doi: 10.1007/s11214-006-8315-7.

B. S. Gaudi. *Microlensing by Exoplanets*, pages 79–110. 2011.

J. Z. Gazak, J. A. Johnson, J. Tonry, D. Dragomir, J. Eastman, A. W. Mann, and E. Agol. Transit Analysis Package: An IDL Graphical User Interface for Exoplanet Transit Photometry. *Advances in Astronomy*, 2012:697967, 2012. doi: 10.1155/2012/697967.

M. Gillon, D. R. Anderson, A. Collier-Cameron, L. Delrez, C. Hellier, E. Jehin, M. Lendl, P. F. L. Maxted, F. Pepe, D. Pollacco, D. Queloz, D. Ségransan, A. M. S. Smith, B. Smalley, J. Southworth, A. H. M. J. Triaud, S. Udry, V. Van Grootel, and R. G. West. WASP-103 b: a new planet at the edge of tidal disruption. *AAP*, 562:L3, Feb. 2014. doi: 10.1051/0004-6361/201323014.

B. Gladman, D. D. Quinn, P. Nicholson, and R. Rand. Synchronous Locking of Tidally Evolving Satellites. *Icarus*, 122:166–192, July 1996. doi: 10.1006/icar.1996.0117.

P. Goldreich and S. J. Peale. The Dynamics of Planetary Rotations. *ARA&A*, 6:287, 1968. doi: 10.1146/annurev.aa.06.090168.001443.

P. Goldreich and S. Soter. Q in the Solar System. *Icarus*, 5:375–389, 1966. doi: 10.1016/0019-1035(66)90051-0.

Y.-X. Gong and J.-L. Zhou. The silicate and carbon-rich models of CoRoT-7b, Kepler-9d and Kepler-10b. *Research in Astronomy and Astrophysics*, 12:678–692, June 2012. doi: 10.1088/1674-4527/12/6/008.

C. J. Hansen, J. C. Schwartz, and N. B. Cowan. Features in the broad-band eclipse spectra

of exoplanets: signal or noise? *MNRAS*, 444:3632–3640, Nov. 2014. doi: 10.1093/mnras/stu1699.

A. P. Hatzes, M. Fridlund, G. Nachmani, T. Mazeh, D. Valencia, G. Hébrard, L. Carone, M. Pätzold, S. Udry, F. Bouchy, M. Deleuil, C. Moutou, P. Barge, P. Bordé, H. Deeg, B. Tingley, R. Dvorak, D. Gandolfi, S. Ferraz-Mello, G. Wuchterl, E. Guenther, T. Guillot, H. Rauer, A. Erikson, J. Cabrera, S. Csizmadia, A. Léger, H. Lammer, J. Weingrill, D. Queloz, R. Alonso, D. Rouan, and J. Schneider. The Mass of CoRoT-7b. *ApJ*, 743:75, Dec. 2011. doi: 10.1088/0004-637X/743/1/75.

C. Hellier, D. R. Anderson, A. Collier-Cameron, G. R. M. Miller, D. Queloz, B. Smalley, J. Southworth, and A. H. M. J. Triaud. On the Orbit of the Short-period Exoplanet WASP-19b. *ApJL*, 730:L31, Apr. 2011. doi: 10.1088/2041-8205/730/2/L31.

K. Heng and P. Kopparla. On the Stability of Super-Earth Atmospheres. *ApJ*, 754:60, July 2012. doi: 10.1088/0004-637X/754/1/60.

W. G. Henning, R. J. O'Connell, and D. D. Sasselov. Tidally Heated Terrestrial Exoplanets: Viscoelastic Response Models. *ApJ*, 707:1000–1015, Dec. 2009. doi: 10.1088/0004-637X/707/2/1000.

H. J. Hoeijmakers, R. J. de Kok, I. A. G. Snellen, M. Brogi, J. L. Birkby, and H. Schwarz. A search for TiO in the optical high-resolution transmission spectrum of HD 209458b: Hindrance due to inaccuracies in the line database. *AAP*, 575:A20, Mar. 2015. doi: 10.1051/0004-6361/201424794.

A. W. Howard, G. W. Marcy, S. T. Bryson, J. M. Jenkins, J. F. Rowe, N. M. Batalha, W. J. Borucki, D. G. Koch, E. W. Dunham, T. N. Gautier, III, J. Van Cleve, W. D. Cochran, D. W. Latham, J. J. Lissauer, G. Torres, T. M. Brown, R. L. Gilliland, L. A. Buchhave, D. A. Caldwell, J. Christensen-Dalsgaard, D. Ciardi, F. Fressin, M. R. Haas, S. B. Howell, H. Kjeldsen, S. Seager, L. Rogers, D. D. Sasselov, J. H. Steffen, G. S. Basri, D. Charbonneau, J. Christiansen, B. Clarke, A. Dupree, D. C. Fabrycky, D. A. Fischer,

E. B. Ford, J. J. Fortney, J. Tarter, F. R. Girouard, M. J. Holman, J. A. Johnson, T. C. Klaus, P. Machalek, A. V. Moorhead, R. C. Morehead, D. Ragozzine, P. Tenenbaum, J. D. Twicken, S. N. Quinn, H. Isaacson, A. Shporer, P. W. Lucas, L. M. Walkowicz, W. F. Welsh, A. Boss, E. Devore, A. Gould, J. C. Smith, R. L. Morris, A. Prsa, T. D. Morton, M. Still, S. E. Thompson, F. Mullally, M. Endl, and P. J. MacQueen. Planet Occurrence within 0.25 AU of Solar-type Stars from Kepler. *ApJS*, 201:15, Aug. 2012. doi: 10.1088/0067-0049/201/2/15.

S. B. Howell, C. Sobeck, M. Haas, M. Still, T. Barclay, F. Mullally, J. Troeltzsch, S. Aigrain, S. T. Bryson, D. Caldwell, W. J. Chaplin, W. D. Cochran, D. Huber, G. W. Marcy, A. Miglio, J. R. Najita, M. Smith, J. D. Twicken, and J. J. Fortney. The K2 Mission: Characterization and Early Results. *PASP*, 126:398–408, Apr. 2014. doi: 10.1086/676406.

R. Hu, B. L. Ehlmann, and S. Seager. Theoretical Spectra of Terrestrial Exoplanet Surfaces. *ApJ*, 752:7, June 2012. doi: 10.1088/0004-637X/752/1/7.

A. P. Ingersoll, M. E. Summers, and S. G. Schlipf. Supersonic meteorology of Io - Sublimation-driven flow of SO2. *Icarus*, 64:375–390, Dec. 1985. doi: 10.1016/0019-1035(85)90062-4.

B. Jackson, N. Miller, R. Barnes, S. N. Raymond, J. J. Fortney, and R. Greenberg. The roles of tidal evolution and evaporative mass loss in the origin of CoRoT-7 b. *MNRAS*, 407: 910–922, Sept. 2010. doi: 10.1111/j.1365-2966.2010.17012.x.

A. Jordán and G. Á. Bakos. Observability of the General Relativistic Precession of Periastra in Exoplanets. *ApJ*, 685:543–552, Sept. 2008. doi: 10.1086/590549.

L. Kaltenegger, W. G. Henning, and D. D. Sasselov. Detecting Volcanism on Extrasolar Planets. *AJ*, 140:1370–1380, Nov. 2010. doi: 10.1088/0004-6256/140/5/1370.

S. R. Kane, J. Horner, and K. von Braun. Cyclic Transit Probabilities of Long-period Eccentric Planets due to Periastron Precession. *ApJ*, 757:105, Sept. 2012. doi: 10.1088/0004-637X/757/1/105.

Y. Kaspi and A. Showman. Atmospheric dynamics of terrestrial exoplanets over a wide range of orbital and atmospheric parameters. In *EGU General Assembly Conference Abstracts*, volume 16 of *EGU General Assembly Conference Abstracts*, page 11654, May 2014.

D. M. Kipping. Transiting planets - light-curve analysis for eccentric orbits. *MNRAS*, 389: 1383–1390, Sept. 2008. doi: 10.1111/j.1365-2966.2008.13658.x.

D. M. Kipping, D. Nesvorný, L. A. Buchhave, J. Hartman, G. Á. Bakos, and A. R. Schmitt. The Hunt for Exomoons with Kepler (HEK). IV. A Search for Moons around Eight M Dwarfs. *ApJ*, 784:28, Mar. 2014. doi: 10.1088/0004-637X/784/1/28.

H. A. Knutson, D. Charbonneau, L. E. Allen, J. J. Fortney, E. Agol, N. B. Cowan, A. P. Showman, C. S. Cooper, and S. T. Megeath. A map of the day-night contrast of the extrasolar planet HD 189733b. *Nature*, 447:183–186, May 2007. doi: 10.1038/nature05782.

H. A. Knutson, D. Charbonneau, A. Burrows, F. T. O'Donovan, and G. Mandushev. Detection of A Temperature Inversion in the Broadband Infrared Emission Spectrum of TrES-4. *ApJ*, 691:866–874, Jan. 2009. doi: 10.1088/0004-637X/691/1/866.

G. Kovács, S. Zucker, and T. Mazeh. A box-fitting algorithm in the search for periodic transits. *AAP*, 391:369–377, Aug. 2002. doi: 10.1051/0004-6361:20020802.

L. Kreidberg, J. L. Bean, J.-M. Désert, B. Benneke, D. Deming, K. B. Stevenson, S. Seager, Z. Berta-Thompson, A. Seifahrt, and D. Homeier. Clouds in the atmosphere of the super-Earth exoplanet GJ1214b. *Nature*, 505:69–72, Jan. 2014. doi: 10.1038/nature12888.

M. J. Kuchner. Volatile-rich Earth-Mass Planets in the Habitable Zone. *ApJL*, 596:L105–L108, Oct. 2003. doi: 10.1086/378397.

D. Lai, F. A. Rasio, and S. L. Shapiro. Ellipsoidal figures of equilibrium - Compressible models. *ApJS*, 88:205–252, Sept. 1993. doi: 10.1086/191822.

H. Lammer, K. G. Kislyakova, M. Güdel, M. Holmström, N. V. Erkaev, P. Odert, and M. L. Khodachenko. Stability of Earth-Like $N_2$ Atmospheres: Implications for Habitability. In

J. M. Trigo-Rodriguez, F. Raulin, C. Muller, and C. Nixon, editors, *The Early Evolution of the Atmospheres of Terrestrial Planets*, volume 35 of *Astrophysics and Space Science Proceedings*, page 33, 2013. doi: 10.1007/978-1-4614-5191-$4_4$.

A. Lecavelier Des Etangs, F. Pont, A. Vidal-Madjar, and D. Sing. Rayleigh scattering in the transit spectrum of HD 189733b. *AAP*, 481:L83–L86, Apr. 2008. doi: 10.1051/0004-6361:200809388.

J. Leconte, D. Lai, and G. Chabrier. Distorted, nonspherical transiting planets: impact on the transit depth and on the radius determination. *AAP*, 528:A41, Apr. 2011. doi: 10.1051/0004-6361/201015811.

J. Leconte, F. Forget, and H. Lammer. On the (anticipated) diversity of terrestrial planet atmospheres. *Experimental Astronomy*, July 2014. doi: 10.1007/s10686-014-9403-4.

J. Leconte, H. Wu, K. Menou, and N. Murray. Asynchronous rotation of Earth-mass planets in the habitable zone of lower-mass stars. *Science*, 347:632–635, Feb. 2015. doi: 10.1126/science.1258686.

A. Léger, F. Selsis, C. Sotin, T. Guillot, D. Despois, D. Mawet, M. Ollivier, A. Labèque, C. Valette, F. Brachet, B. Chazelas, and H. Lammer. A new family of planets? "Ocean-Planets". *Icarus*, 169:499–504, June 2004. doi: 10.1016/j.icarus.2004.01.001.

A. Léger, D. Rouan, J. Schneider, P. Barge, M. Fridlund, B. Samuel, M. Ollivier, E. Guenther, M. Deleuil, H. J. Deeg, M. Auvergne, R. Alonso, S. Aigrain, A. Alapini, J. M. Almenara, A. Baglin, M. Barbieri, H. Bruntt, P. Bordé, F. Bouchy, J. Cabrera, C. Catala, L. Carone, S. Carpano, S. Csizmadia, R. Dvorak, A. Erikson, S. Ferraz-Mello, B. Foing, F. Fressin, D. Gandolfi, M. Gillon, P. Gondoin, O. Grasset, T. Guillot, A. Hatzes, G. Hébrard, L. Jorda, H. Lammer, A. Llebaria, B. Loeillet, M. Mayor, T. Mazeh, C. Moutou, M. Pätzold, F. Pont, D. Queloz, H. Rauer, S. Renner, R. Samadi, A. Shporer, C. Sotin, B. Tingley, G. Wuchterl, M. Adda, P. Agogu, T. Appourchaux, H. Ballans, P. Baron, T. Beaufort, R. Bellenger,

R. Berlin, P. Bernardi, D. Blouin, F. Baudin, P. Bodin, L. Boisnard, L. Boit, F. Bonneau, S. Borzeix, R. Briet, J.-T. Buey, B. Butler, D. Cailleau, R. Cautain, P.-Y. Chabaud, S. Chaintreuil, F. Chiavassa, V. Costes, V. Cuna Parrho, F. de Oliveira Fialho, M. Decaudin, J.-M. Defise, S. Djalal, G. Epstein, G.-E. Exil, C. Fauré, T. Fenouillet, A. Gaboriaud, A. Gallic, P. Gamet, P. Gavalda, E. Grolleau, R. Gruneisen, L. Gueguen, V. Guis, V. Guivarc'h, P. Guterman, D. Hallouard, J. Hasiba, F. Heuripeau, G. Huntzinger, H. Hustaix, C. Imad, C. Imbert, B. Johlander, M. Jouret, P. Journoud, F. Karioty, L. Kerjean, V. Lafaille, L. Lafond, T. Lam-Trong, P. Landiech, V. Lapeyrere, T. Larqué, P. Laudet, N. Lautier, H. Lecann, L. Lefevre, B. Leruyet, P. Levacher, A. Magnan, E. Mazy, F. Mertens, J.-M. Mesnager, J.-C. Meunier, J.-P. Michel, W. Monjoin, D. Naudet, K. Nguyen-Kim, J.-L. Orcesi, H. Ottacher, R. Perez, G. Peter, P. Plasson, J.-Y. Plesseria, B. Pontet, A. Pradines, C. Quentin, J.-L. Reynaud, G. Rolland, F. Rollenhagen, R. Romagnan, N. Russ, R. Schmidt, N. Schwartz, I. Sebbag, G. Sedes, H. Smit, M. B. Steller, W. Sunter, C. Surace, M. Tello, D. Tiphène, P. Toulouse, B. Ulmer, O. Vandermarcq, E. Vergnault, A. Vuillemin, and P. Zanatta. Transiting exoplanets from the CoRoT space mission. VIII. CoRoT-7b: the first super-Earth with measured radius. *AAP*, 506:287–302, Oct. 2009. doi: 10.1051/0004-6361/200911933.

A. Léger, O. Grasset, B. Fegley, F. Codron, A. F. Albarede, P. Barge, R. Barnes, P. Cance, S. Carpy, F. Catalano, C. Cavarroc, O. Demangeon, S. Ferraz-Mello, P. Gabor, J.-M. Grießmeier, J. Leibacher, G. Libourel, A.-S. Maurin, S. N. Raymond, D. Rouan, B. Samuel, L. Schaefer, J. Schneider, P. A. Schuller, F. Selsis, and C. Sotin. The extreme physical properties of the CoRoT-7b super-Earth. *Icarus*, 213:1–11, May 2011. doi: 10.1016/j.icarus.2011.02.004.

N. K. Lewis, A. P. Showman, J. J. Fortney, H. A. Knutson, and M. S. Marley. Atmospheric Circulation of Eccentric Hot Jupiter HAT-P-2b. *ApJ*, 795:150, Nov. 2014. doi: 10.1088/0004-637X/795/2/150.

S.-L. Li, N. Miller, D. N. C. Lin, and J. J. Fortney. WASP-12b as a prolate, inflated and disrupting planet from tidal dissipation. *Nature*, 463:1054–1056, Feb. 2010. doi: 10.1038/nature08715.

J. J. Lissauer, R. I. Dawson, and S. Tremaine. Advances in exoplanet science from Kepler. *Nature*, 513:336–344, Sept. 2014. doi: 10.1038/nature13781.

A. Loeb and B. S. Gaudi. Periodic Flux Variability of Stars due to the Reflex Doppler Effect Induced by Planetary Companions. *ApJL*, 588:L117–L120, May 2003. doi: 10.1086/375551.

P. Machalek, P. R. McCullough, C. J. Burke, J. A. Valenti, A. Burrows, and J. L. Hora. Thermal Emission of Exoplanet XO-1b. *ApJ*, 684:1427–1432, Sept. 2008. doi: 10.1086/590140.

N. Madhusudhan, K. K. M. Lee, and O. Mousis. A Possible Carbon-rich Interior in Super-Earth 55 Cancri e. *ApJL*, 759:L40, Nov. 2012. doi: 10.1088/2041-8205/759/2/L40.

N. Madhusudhan, H. Knutson, J. J. Fortney, and T. Barman. Exoplanetary Atmospheres. *Protostars and Planets VI*, pages 739–762, 2014. doi: $10.2458/\mathrm{azu}_u apress_9 780816531240 - ch032$.

C. Majeau, E. Agol, and N. B. Cowan. A Two-dimensional Infrared Map of the Extrasolar Planet HD 189733b. *ApJL*, 747:L20, Mar. 2012. doi: 10.1088/2041-8205/747/2/L20.

V. V. Makarov and M. Efroimsky. No Pseudosynchronous Rotation for Terrestrial Planets and Moons. *ApJ*, 764:27, Feb. 2013. doi: 10.1088/0004-637X/764/1/27.

V. V. Makarov and M. Efroimsky. Tidal Dissipation in a Homogeneous Spherical Body. II. Three Examples: Mercury, IO, and Kepler-10 b. *ApJ*, 795:7, Nov. 2014. doi: 10.1088/0004-637X/795/1/7.

K. Mandel and E. Agol. Analytic Light Curves for Planetary Transit Searches. *ApJL*, 580: L171–L175, Dec. 2002. doi: 10.1086/345520.

A. M. Mandell, K. Haynes, E. Sinukoff, N. Madhusudhan, A. Burrows, and D. Deming. Exoplanet Transit Spectroscopy Using WFC3: WASP-12 b, WASP-17 b, and WASP-19 b. *ApJ*, 779:128, Dec. 2013. doi: 10.1088/0004-637X/779/2/128.

J. W. Mason. *Exoplanets*. 2008. doi: 10.1007/978-3-540-74008-7.

M. Mayor and D. Queloz. A Jupiter-mass companion to a solar-type star. *Nature*, 378: 355–359, Nov. 1995. doi: 10.1038/378355a0.

Y. Miguel, L. Kaltenegger, B. Fegley, and L. Schaefer. Compositions of Hot Super-earth Atmospheres: Exploring Kepler Candidates. *ApJL*, 742:L19, Dec. 2011. doi: 10.1088/2041-8205/742/2/L19.

E. Miller-Ricci Kempton and E. Rauscher. Constraining High-speed Winds in Exoplanet Atmospheres through Observations of Anomalous Doppler Shifts during Transit. *ApJ*, 751: 117, June 2012. doi: 10.1088/0004-637X/751/2/117.

D. Mislis, R. Heller, J. H. M. M. Schmitt, and S. Hodgkin. Estimating transiting exoplanet masses from precise optical photometry. *AAP*, 538:A4, Feb. 2012. doi: 10.1051/0004-6361/201116711.

G. D. Mulders, I. Pascucci, and D. Apai. A Stellar-mass-dependent Drop in Planet Occurrence Rates. *ApJ*, 798:112, Jan. 2015. doi: 10.1088/0004-637X/798/2/112.

H. M. Müller, K. F. Huber, S. Czesla, U. Wolter, and J. H. M. M. Schmitt. High-precision stellar limb-darkening measurements. A transit study of 38 Kepler planetary candidates. *AAP*, 560:A112, Dec. 2013. doi: 10.1051/0004-6361/201322079.

Murray, C. D. and Dermott, S. F. *Solar System Dynamics*. feb 2000.

B. Nelson, E. B. Ford, and M. J. Payne. RUN DMC: An Efficient, Parallel Code for Analyzing Radial Velocity Observations Using N-body Integrations and Differential Evolution Markov Chain Monte Carlo. *ApJS*, 210:11, Jan. 2014. doi: 10.1088/0067-0049/210/1/11.

N. Nikolov, D. K. Sing, F. Pont, A. S. Burrows, J. J. Fortney, G. E. Ballester, T. M. Evans, C. M. Huitson, H. R. Wakeford, P. A. Wilson, S. Aigrain, D. Deming, N. P. Gibson, G. W. Henry, H. Knutson, A. Lecavelier des Etangs, A. P. Showman, A. Vidal-Madjar, and K. Zahnle. Hubble Space Telescope hot Jupiter transmission spectral survey: a detection of Na and strong optical absorption in HAT-P-1b. *MNRAS*, 437:46–66, Jan. 2014. doi: 10.1093/mnras/stt1859.

F. Nimmo and K. Tanaka. Early Crustal Evolution of Mars. *Annual Review of Earth and Planetary Sciences*, 33:133–161, Jan. 2005. doi: 10.1146/annurev.earth.33.092203.122637.

P. Nutzman and D. Charbonneau. Design Considerations for a Ground-Based Transit Search for Habitable Planets Orbiting M Dwarfs. *PASP*, 120:317–327, Mar. 2008. doi: 10.1086/533420.

Y. Ohta, A. Taruya, and Y. Suto. The Rossiter-McLaughlin Effect and Analytic Radial Velocity Curves for Transiting Extrasolar Planetary Systems. *ApJ*, 622:1118–1135, Apr. 2005. doi: 10.1086/428344.

J. T. O'Malley-James, C. S. Cockell, J. S. Greaves, and J. A. Raven. Swansong biospheres II: the final signs of life on terrestrial planets near the end of their habitable lifetimes. *International Journal of Astrobiology*, 13:229–243, July 2014. doi: 10.1017/S1473550413000426.

C. O'Neill and A. Lenardic. Geological consequences of super-sized Earths. *GRL*, 34:L19204, Oct. 2007. doi: 10.1029/2007GL030598.

J. E. Owen and Y. Wu. Kepler Planets: A Tale of Evaporation. *ApJ*, 775:105, Oct. 2013. doi: 10.1088/0004-637X/775/2/105.

M. T. Penny and B. S. Gaudi. Exploring exoplanetary systems beyond 1AU with WFIRST. In M. Booth, B. C. Matthews, and J. R. Graham, editors, *IAU Symposium*, volume 299 of *IAU Symposium*, pages 62–63, Jan. 2014. doi: 10.1017/S1743921313007886.

D. Perez-Becker and E. Chiang. Catastrophic evaporation of rocky planets. *MNRAS*, 433: 2294–2309, Aug. 2013. doi: 10.1093/mnras/stt895.

M. Perryman, J. Hartman, G. Á. Bakos, and L. Lindegren. Astrometric Exoplanet Detection with Gaia. *ApJ*, 797:14, Dec. 2014. doi: 10.1088/0004-637X/797/1/14.

B. Placek, K. H. Knuth, and D. Angerhausen. EXONEST: Bayesian Model Selection Applied to the Detection and Characterization of Exoplanets via Photometric Variations. *ApJ*, 795: 112, Nov. 2014. doi: 10.1088/0004-637X/795/2/112.

PLATO Study Team. PLATO Assessment Study Report (Yellow Book). *ESA/SRE(2013)5*, pages 1–107, 2013.

J. Radigan, R. Jayawardhana, D. Lafrenière, É. Artigau, M. Marley, and D. Saumon. Large-amplitude Variations of an L/T Transition Brown Dwarf: Multi-wavelength Observations of Patchy, High-contrast Cloud Features. *ApJ*, 750:105, May 2012. doi: 10.1088/0004-637X/750/2/105.

D. Ragozzine and A. S. Wolf. Probing the Interiors of very Hot Jupiters Using Transit Light Curves. *ApJ*, 698:1778–1794, June 2009. doi: 10.1088/0004-637X/698/2/1778.

S. Rappaport, R. Sanchis-Ojeda, L. A. Rogers, A. Levine, and J. N. Winn. The Roche Limit for Close-orbiting Planets: Minimum Density, Composition Constraints, and Application to the 4.2 hr Planet KOI 1843.03. *ApJL*, 773:L15, Aug. 2013. doi: 10.1088/2041-8205/773/1/L15.

I. N. Reid and S. L. Hawley. *New light on dark stars : red dwarfs, low-mass stars, brown dwarfs*. 2005. doi: 10.1007/3-540-27610-6.

G. R. Ricker, J. N. Winn, R. Vanderspek, D. W. Latham, G. Á. Bakos, J. L. Bean, Z. K. Berta-Thompson, T. M. Brown, L. Buchhave, N. R. Butler, R. P. Butler, W. J. Chaplin, D. Charbonneau, J. Christensen-Dalsgaard, M. Clampin, D. Deming, J. Doty, N. De Lee, C. Dressing, E. W. Dunham, M. Endl, F. Fressin, J. Ge, T. Henning, M. J. Holman, A. W. Howard, S. Ida, J. Jenkins, G. Jernigan, J. A. Johnson, L. Kaltenegger, N. Kawai,

H. Kjeldsen, G. Laughlin, A. M. Levine, D. Lin, J. J. Lissauer, P. MacQueen, G. Marcy, P. R. McCullough, T. D. Morton, N. Narita, M. Paegert, E. Palle, F. Pepe, J. Pepper, A. Quirrenbach, S. A. Rinehart, D. Sasselov, B. Sato, S. Seager, A. Sozzetti, K. G. Stassun, P. Sullivan, A. Szentgyorgyi, G. Torres, S. Udry, and J. Villasenor. Transiting Exoplanet Survey Satellite (TESS). In *Society of Photo-Optical Instrumentation Engineers (SPIE) Conference Series*, volume 9143 of *Society of Photo-Optical Instrumentation Engineers (SPIE) Conference Series*, page 20, Aug. 2014. doi: 10.1117/12.2063489.

P. Robertson, S. Mahadevan, M. Endl, and A. Roy. Stellar activity masquerading as planets in the habitable zone of the M dwarf Gliese 581. *Science*, 345:440–444, July 2014. doi: 10.1126/science.1253253.

R. Sanchis-Ojeda, S. Rappaport, J. N. Winn, A. Levine, M. C. Kotson, D. W. Latham, and L. A. Buchhave. Transits and Occultations of an Earth-sized Planet in an 8.5 hr Orbit. *ApJ*, 774:54, Sept. 2013. doi: 10.1088/0004-637X/774/1/54.

R. Sanchis-Ojeda, S. Rappaport, J. N. Winn, M. C. Kotson, A. Levine, and I. El Mellah. A Study of the Shortest-period Planets Found with Kepler. *ApJ*, 787:47, May 2014. doi: 10.1088/0004-637X/787/1/47.

P. Saxena, P. Panka, and M. Summers. The observational effects and signatures of tidally distorted solid exoplanets. *MNRAS*, 446:4271–4277, Feb. 2015. doi: 10.1093/mnras/stu2111.

L. Schaefer and B. Fegley. A thermodynamic model of high temperature lava vaporization on Io. *Icarus*, 169:216–241, May 2004. doi: 10.1016/j.icarus.2003.08.023.

L. Schaefer and B. Fegley. Chemistry of Silicate Atmospheres of Evaporating Super-Earths. *ApJL*, 703:L113–L117, Oct. 2009. doi: 10.1088/0004-637X/703/2/L113.

L. Schaefer, K. Lodders, and B. Fegley. Vaporization of the Earth: Application to Exoplanet Atmospheres. *ApJ*, 755:41, Aug. 2012. doi: 10.1088/0004-637X/755/1/41.

C. A. Scharf. *Extrasolar Planets and Astrobiology.* University Science Books, 2009.

S. Seager and D. Deming. Exoplanet Atmospheres. *ARA&A*, 48:631–672, Sept. 2010. doi: 10.1146/annurev-astro-081309-130837.

S. Seager and L. Hui. Constraining the Rotation Rate of Transiting Extrasolar Planets by Oblateness Measurements. *ApJ*, 574:1004–1010, Aug. 2002. doi: 10.1086/340994.

S. Seager and J. J. Lissauer. *Introduction to Exoplanets*, pages 3–13. 2011.

S. Seager and G. Mallén-Ornelas. A Unique Solution of Planet and Star Parameters from an Extrasolar Planet Transit Light Curve. *ApJ*, 585:1038–1055, Mar. 2003.

A. P. Showman, R. D. Wordsworth, T. M. Merlis, and Y. Kaspi. *Atmospheric Circulation of Terrestrial Exoplanets*, pages 277–326. 2013. doi: $10.2458/\mathrm{azu}_u apress_9 780816530595 - ch12$.

A. P. Showman, N. K. Lewis, and J. J. Fortney. 3D Atmospheric Circulation of Warm and Hot Jupiters. *ApJ*, 801:95, Mar. 2015. doi: 10.1088/0004-637X/801/2/95.

D. K. Sing, A. Lecavelier des Etangs, J. J. Fortney, A. S. Burrows, F. Pont, H. R. Wakeford, G. E. Ballester, N. Nikolov, G. W. Henry, S. Aigrain, D. Deming, T. M. Evans, N. P. Gibson, C. M. Huitson, H. Knutson, A. P. Showman, A. Vidal-Madjar, P. A. Wilson, M. H. Williamson, and K. Zahnle. HST hot-Jupiter transmission spectral survey: evidence for aerosols and lack of TiO in the atmosphere of WASP-12b. *MNRAS*, 436:2956–2973, Dec. 2013. doi: 10.1093/mnras/stt1782.

I. A. G. Snellen, B. R. Brandl, R. J. de Kok, M. Brogi, J. Birkby, and H. Schwarz. Fast spin of the young extrasolar planet $\beta$ Pictoris b. *Nature*, 509:63–65, May 2014. doi: 10.1038/nature13253.

J. H. Steffen, D. C. Fabrycky, E. Agol, E. B. Ford, R. C. Morehead, W. D. Cochran, J. J. Lissauer, E. R. Adams, W. J. Borucki, S. Bryson, D. A. Caldwell, A. Dupree, J. M. Jenkins, P. Robertson, J. F. Rowe, S. Seader, S. Thompson, and J. D. Twicken. Transit timing observations from Kepler - VII. Confirmation of 27 planets in 13 multiplanet systems via transit timing variations and orbital stability. *MNRAS*, 428:1077–1087, Jan. 2013. doi: 10.1093/mnras/sts090.

K. B. Stevenson, J. L. Bean, A. Seifahrt, J.-M. Désert, N. Madhusudhan, M. Bergmann, L. Kreidberg, and D. Homeier. Transmission Spectroscopy of the Hot Jupiter WASP-12b from 0.7 to 5 $\mu$m. *AJ*, 147:161, June 2014a. doi: 10.1088/0004-6256/147/6/161.

K. B. Stevenson, J.-M. Désert, M. R. Line, J. L. Bean, J. J. Fortney, A. P. Showman, T. Kataria, L. Kreidberg, P. R. McCullough, G. W. Henry, D. Charbonneau, A. Burrows, S. Seager, N. Madhusudhan, M. H. Williamson, and D. Homeier. Thermal structure of an exoplanet atmosphere from phase-resolved emission spectroscopy. *Science*, 346:838–841, Nov. 2014b. doi: 10.1126/science.1256758.

T. Sumi, K. Kamiya, D. P. Bennett, I. A. Bond, F. Abe, C. S. Botzler, A. Fukui, K. Furusawa, J. B. Hearnshaw, Y. Itow, P. M. Kilmartin, A. Korpela, W. Lin, C. H. Ling, K. Masuda, Y. Matsubara, N. Miyake, M. Motomura, Y. Muraki, M. Nagaya, S. Nakamura, K. Ohnishi, T. Okumura, Y. C. Perrott, N. Rattenbury, T. Saito, T. Sako, D. J. Sullivan, W. L. Sweatman, P. J. Tristram, A. Udalski, M. K. Szymański, M. Kubiak, G. Pietrzyński, R. Poleski, I. Soszyński, Ł. Wyrzykowski, K. Ulaczyk, and Microlensing Observations in Astrophysics (MOA) Collaboration. Unbound or distant planetary mass population detected by gravitational microlensing. *Nature*, 473:349–352, May 2011. doi: 10.1038/nature10092.

M. R. Swain, M. R. Line, and P. Deroo. On the Detection of Molecules in the Atmosphere of HD 189733b Using HST NICMOS Transmission Spectroscopy. *ApJ*, 784:133, Apr. 2014. doi: 10.1088/0004-637X/784/2/133.

M. Tuomi and H. R. A. Jones. Probabilities of exoplanet signals from posterior samplings. *AAP*, 544:A116, Aug. 2012. doi: 10.1051/0004-6361/201118114.

D. Valencia, R. J. O'Connell, and D. Sasselov. Internal structure of massive terrestrial planets. *Icarus*, 181:545–554, Apr. 2006. doi: 10.1016/j.icarus.2005.11.021.

D. Valencia, R. J. O'Connell, and D. D. Sasselov. Inevitability of Plate Tectonics on Super-Earths. *ApJL*, 670:L45–L48, Nov. 2007a. doi: 10.1086/524012.

D. Valencia, D. D. Sasselov, and R. J. O'Connell. Detailed Models of Super-Earths: How Well Can We Infer Bulk Properties? *ApJ*, 665:1413–1420, Aug. 2007b. doi: 10.1086/519554.

D. Valencia, M. Ikoma, T. Guillot, and N. Nettelmann. Composition and fate of short-period super-Earths. The case of CoRoT-7b. *AAP*, 516:A20, June 2010. doi: 10.1051/0004-6361/200912839.

F. W. Wagner, N. Tosi, F. Sohl, H. Rauer, and T. Spohn. Rocky super-Earth interiors. Structure and internal dynamics of CoRoT-7b and Kepler-10b. *AAP*, 541:A103, May 2012. doi: 10.1051/0004-6361/201118441.

L. M. Weiss and G. W. Marcy. The Mass-Radius Relation for 65 Exoplanets Smaller than 4 Earth Radii. *ApJL*, 783:L6, Mar. 2014. doi: 10.1088/2041-8205/783/1/L6.

M. W. Werner, T. L. Roellig, F. J. Low, G. H. Rieke, M. Rieke, W. F. Hoffmann, E. Young, J. R. Houck, B. Brandl, G. G. Fazio, J. L. Hora, R. D. Gehrz, G. Helou, B. T. Soifer, J. Stauffer, J. Keene, P. Eisenhardt, D. Gallagher, T. N. Gautier, W. Irace, C. R. Lawrence, L. Simmons, J. E. Van Cleve, M. Jura, E. L. Wright, and D. P. Cruikshank. The Spitzer Space Telescope Mission. *ApJS*, 154:1–9, Sept. 2004. doi: 10.1086/422992.

J. N. Winn. Transits and Occultations. *ArXiv e-prints*, Jan. 2010.

J. N. Winn and D. C. Fabrycky. The Occurrence and Architecture of Exoplanetary Systems. *ArXiv e-prints*, Oct. 2014.

J. N. Winn, J. M. Matthews, R. I. Dawson, D. Fabrycky, M. J. Holman, T. Kallinger, R. Kuschnig, D. Sasselov, D. Dragomir, D. B. Guenther, A. F. J. Moffat, J. F. Rowe, S. Rucinski, and W. W. Weiss. A Super-Earth Transiting a Naked-eye Star. *ApJL*, 737: L18, Aug. 2011. doi: 10.1088/2041-8205/737/1/L18.

I. Wong, H. A. Knutson, N. B. Cowan, N. K. Lewis, E. Agol, A. Burrows, D. Deming, J. J. Fortney, B. J. Fulton, J. Langton, G. Laughlin, and A. P. Showman. Constraints on the

Atmospheric Circulation and Variability of the Eccentric Hot Jupiter XO-3b. *ApJ*, 794:134, Oct. 2014. doi: 10.1088/0004-637X/794/2/134.

R. Wordsworth. Atmospheric heat redistribution and collapse on tidally locked rocky planets. *ArXiv e-prints*, Dec. 2014.

J. T. Wright and B. S. Gaudi. *Exoplanet Detection Methods*, page 489. 2013. doi: 10.1007/978-94-007-5606-9$_1$0.

J. T. Wright and A. W. Howard. Efficient Fitting of Multiplanet Keplerian Models to Radial Velocity and Astrometry Data. *ApJS*, 182:205, May 2009. doi: 10.1088/0067-0049/182/1/205.

A. Wyttenbach, D. Ehrenreich, C. Lovis, S. Udry, and F. Pepe. Spectrally resolved detection of sodium in the atmosphere of HD189733b with the HARPS spectrograph. *ArXiv e-prints*, Mar. 2015.

M. Zechmeister and M. Kürster. The generalised Lomb-Scargle periodogram. A new formalism for the floating-mean and Keplerian periodograms. *AAP*, 496:577–584, Mar. 2009. doi: 10.1051/0004-6361:200811296.

W. Zhu, C. X. Huang, G. Zhou, and D. N. C. Lin. Constraining the Oblateness of Kepler Planets. *ApJ*, 796:67, Nov. 2014. doi: 10.1088/0004-637X/796/1/67.

# Curriculum Vitae

Prabal Saxena graduated from Hicksville High School, Hicksville, NY in 2003. He received his Bachelor of Science from Columbia University in 2007. He then worked for Saralux LLC Consulting in New York City until 2009. He began his graduate work at George Mason University in Fairfax, Virginia later that year.